Università di Pisa

Dipartimento di Fisica
Corso di laurea magistrale in Fisica

Tesi di laurea

Measurement of the CP violation parameter A_Γ in $D^0 \to K^+K^-$ and $D^0 \to \pi^+\pi^-$ decays with LHCb Run 2 data

CERN-THESIS-2017-439

Candidato:
Tommaso Pajero

Relatore:
Dott. Michael J. Morello

Relatore interno:
Prof. Giovanni Punzi

Anno accademico 2016–2017

Abstract

Time-dependent CP asymmetries in the decay rates of the D^0 and $\overline{D}^0$ mesons into the CP-symmetric, singly Cabibbo-suppressed final states K^+K^- and $\pi^+\pi^-$ are measured in pp collisions collected by the LHCb experiment in 2015 and in 2016 at the centre-of-mass energy of 13 TeV, corresponding to an integrated luminosity of 1.7 fb^{-1}. The strong-interaction decay $D^{*+} \to D^0\pi^+$ is used to infer the flavour of the D^0 meson at production. The asymmetry between the effective decay widths of the D^0 and $\overline{D}^0$ decays, sensitive to indirect CP violation, is measured to be

$$A_\Gamma(D^0 \to K^+K^-) = (-60.9 \pm 3.8 \pm 0.6) \cdot 10^{-4},$$
$$A_\Gamma(D^0 \to \pi^+\pi^-) = (-62.5 \pm 6.7 \pm 0.5) \cdot 10^{-4},$$

where the first uncertainty is statistical, the second one systematic and the central values are blinded pending the receipt of the approval of the analysis procedure by the LHCb collaboration. The obtained statistical precision is comparable to the previous, world-leading measurement of A_Γ by the LHCb collaboration, whereas the systematic uncertainty is reduced by about a factor of 2.

Contents

Introduction

The standard model of particle physics (SM) constitutes the reference model to describe all the interactions between known elementary particles, except for gravity. Over the course of the last decades, it has been tested thoroughly to a remarkable degree of precision by several generations of experiments, and no significant deviations from its predictions have been observed so far. However, there are many reasons to doubt that it constitutes the final word on particle physics. For example, the low value of the mass of the Higgs boson cannot be explained without an unnatural fine-tuning cancellation between its bare mass and its radiative corrections, the SM cannot account for the presence of dark matter that is observed in our universe, nor its baryonic asymmetry, *i.e.* the observation that the universe content is largely dominated by matter while antimatter is just a tiny fraction of it. Therefore, it is universally acknowledged that the SM is just the low-energy approximation of a more general theory, whose discovery is currently the main aim of the particle physics community.

High precision measurements of the non-invariance of the weak interaction under the combined action of the charge conjugation (C) and parity (P) operators, commonly referenced as CP violation (CPV), are one of the main topics investigated in order to evidence some of the possible properties of this new theory. In the SM, the only known source of CPV is the irreducible complex phase in the Cabibbo-Kobayashi-Maskawa (CKM) quark mixing matrix. However, the amount of CPV produced through the CKM mechanism is too small to explain the baryonic asymmetry of the universe. This fact suggests that the theory that extends the SM might exhibit some additional sources of CPV. Moreover, it is possible that these new sources manifest themselves also at energies that are much lower than the typical energy scale of the new interactions and particles, in the form of slight deviations from the SM predictions in the decay of well known particles, thanks to the contribution to their decay amplitudes from loop diagrams of order larger than the first non-null in the SM [1].

This fact motivates the interest for the high precision measurements of CPV in the decays of particles containing charm quarks, and in particular of the D^0 ($c\overline{u}$) neutral meson. In fact, in these decays the SM contribution to CPV is very low, $\leq \mathcal{O}(10^{-3})$ [1,2], since they involve, to good approximation, only quarks of the first two generations, whereas the complex term of the CKM matrix mainly affects transitions between the first and the third generation of quarks. As a consequence, the charm decays are particularly sensitive to CP-violating contributions from new physics phenomena. Moreover, the charm quark is the only up-type quark allowing to explore all aspects of mixing and CPV (top quarks decay before adronising, whereas the neutral particles composed of the u and $\overline{u}$ quarks, like the π^0 meson, coincide with their antiparticle). Therefore, the study of the charm sector might highlight new phenomena of CPV that cannot be evidenced by the study of kaons and B mesons, being exclusively or mainly related to up-type quarks.

The discovery of CPV in D^0 decays would thus constitute an important achievement for particle physics. It should not be forgotten that, since we are now nearly reaching the precision needed to measure the CPV contribution of the SM, the observation of CPV in D^0 decays would not directly imply the presence of new physics phenomena. However, the progressive improvement of theoretical studies, and in particular of lattice calculations, accompanied by the new measurements of charm decays that are foreseen in the next few years, will hopefully lead to more precise estimates of the SM contribution and, as a consequence, also a better sensitivity to unexpected phenomena.

The most sensitive probe for *CPV* in the charm sector is given by decays of D^0 mesons into *CP* eigenstates f, where $f = K^+K^-$ or $f = \pi^+\pi^-$. Since both the charm mixing parameters $x = \Delta m/\Gamma$ and $y = \Delta\Gamma/(2\Gamma)$ and the direct *CPV* in these decays are known to be smaller than 10^{-2} [3], the time-dependent *CP* asymmetry of each decay can be approximated as

$$A_{CP}(t) = \frac{\Gamma(D^0(t) \to f) - \Gamma(\overline{D}^0(t) \to f)}{\Gamma(D^0(t) \to f) + \Gamma(\overline{D}^0(t) \to f)} \approx a^f_{\mathrm{dir}} - A_\Gamma \frac{t}{\tau(D^0)}$$

where $\Gamma(D^0(t) \to f)$ indicates the time-dependent decay rate of a charmed meson produced as a D^0 into final state f after a time t, $\tau(D^0)$ is the lifetime of the D^0 meson, a^f_{dir} is related to *CPV* in the decay and A_Γ is a parameter sensitive to indirect *CPV*, both in the mixing and in the interference.[1] So far, the A_Γ parameter has provided the strongest limits on indirect *CPV* in the charm sector. In particular, the LHCb experiment has recently published, in 2017, the most precise measurement of A_Γ ever made [4], using the full data sample collected during the LHC Run 1 (2011–2012), corresponding to $3\,\mathrm{fb}^{-1}$ of integrated luminosity of *pp* collisions at 7–8 TeV, approximately 9 (3) million reconstructed $D^0 \to K^+K^-$ ($D^0 \to \pi^+\pi^-$) decays. The result,

$$A_\Gamma(D^0 \to K^+K^-) = (-3.0 \pm 3.2 \pm 1.0) \cdot 10^{-4},$$
$$A_\Gamma(D^0 \to \pi^+\pi^-) = (+4.6 \pm 5.8 \pm 1.2) \cdot 10^{-4},$$

is compatible with the hypothesis of no *CPV* and currently dominates the world average. Since the most recent SM predictions for A_Γ are approximately in the range of 10^{-3}–10^{-4} [1, 2], and LHCb has just entered such a precision regime, where the *CPV* predicted by the SM might become detectable, it would be very important to push the experimental sensitivity well below the level of 10^{-4} as soon as possible in order to highlight a possible first evidence of CPV in the charm sector.

The work described in this thesis has therefore a dual purpose. Firstly, it aims at improving the statistical precision on A_Γ extending its measurement to the total currently available LHCb data sample, including the new data collected during the LHC Run 2 (2015–2016). Secondly, it aims at a significant reduction of systematic uncertainties, paving the way to the measurements with still higher precision that are foreseen in the next few years, whose statistical uncertainty will quickly become comparable or even lesser than the current systematic one.[2]

Despite the integrated luminosity of the new data sample, collected during Run 2 in 2015–2016 ($1.7\,\mathrm{fb}^{-1}$), being lesser than that of Run 1 ($3\,\mathrm{fb}^{-1}$), its size is larger than that of Run 1 approximately by a factor of 2, resulting in about 22 million $D^0 \to K^+K^-$, 7 million $D^0 \to \pi^+\pi^-$ and 194 million $D^0 \to K^-\pi^+$ decays.[3] The increasing of the LHCb capability in collecting such decays can be ascribed to several factors. The centre-of-mass energy of the *pp* collisions has increased from 7–8 TeV to 13 TeV, thereby increasing the charm production cross section by a factor of 1.8 [5]. The trigger of the LHCb experiment has undergone a substantial revision [6, 7], moving towards the configuration that will be adopted at the more challenging data-taking

[1]The A_Γ parameter is defined as the asymmetry between the D^0 and $\overline{D}^0$ effective decay widths, $A_\Gamma = \frac{\hat{\Gamma}(D^0 \to f) - \hat{\Gamma}(\overline{D}^0 \to f)}{\hat{\Gamma}(D^0 \to f) + \hat{\Gamma}(\overline{D}^0 \to f)}$, where $\hat{\Gamma}(D^0 \to f)$ is the effective decay width that is measured parametrising the decay rate of a particle that is produced at $t = 0$ as D^0 flavour eigenstate with a simple exponential function.

[2]The LHCb experiment is foreseen to collect further $3\,\mathrm{fb}^{-1}$ of integrated luminosity of data during Run 2, by the end of 2018, and additional $40\,\mathrm{fb}^{-1}$ in Run 3 and Run 4, before 2030.

[3]As in the Run 1 measurement, the high statistics sample of Cabibbo-favoured $D^0 \to K^-\pi^+$ decays is used in order to validate the analysis procedure, as no *CPV* is expected to be detectable for it within the current sensitivity.

conditions of Run 3 (2021), where the instantaneous luminosity will grow by a factor of 5. Finally, the reduction of the event size and the parallel increase of the rate at which data are stored to disk produced an additional increase of the data-taking rate.

As the Run 2 data-taking conditions have changed considerably with respect to those of Run 1, a careful analysis of the impact of the new selection criteria, including new trigger lines, on the A_Γ measurement is performed in the thesis. As it was shown in the past, trigger requirements on momenta and decay time-related quantities introduce correlations between the D^0 decay time and other kinematic variables that affect the detection efficiency, generating biases to the measurement of A_Γ of order 10^{-3}, well above the statistical uncertainty. The main source of these detector-induced, time-dependent charge asymmetries has been studied and pinpointed at very high precision, along with the correction procedure, developed in Run 1, to account for them. This allowed a better understanding of what would be the optimal trigger configuration to be used to collect the remainder of Run 2 data (2017–2018), and that to be adopted in the future LHC runs at higher luminosity, in order to continue to keep the uncertainty on the correction procedure under control and well below the statistical one.

In the thesis, dominant systematic uncertainties have been studied and assessed with the new Run 2 data sample. This has been done in preparation for future measurements at much higher precision. Particular attention has been dedicated to reducing the size of the systematic uncertainty, resulting to be the dominant one in the Run 1 measurement, due to a few per cent residual contamination of D^0 mesons that originate from weak decays of b-hadrons (secondary decays), and not in the pp primary vertex (primary decays). Since the reconstructed decay times of these D^0 mesons are biased towards higher values,[4] and since they are characterised by different production and detection asymmetries with respect to primary decays, a fake value of A_Γ can be artificially generated. In Run 1, the contribution of secondary decays to the measurement of A_Γ was not subtracted and a systematic uncertainty of $1.0 \cdot 10^{-4}$ was assessed to fully cover its value. In this thesis, a novel approach was developed to subtract their contribution and to drastically reduce the size of the associated systematic uncertainty, in order to prepare the future LHCb measurements with a much higher number of decays.

In conclusion, this thesis presents the preliminary measurement of the *CP* violation parameter A_Γ in $D^0 \to K^+K^-$ and $D^0 \to \pi^+\pi^-$ decays with the data collected in pp collisions by LHCb in Run 2 during 2015 and 2016, at a centre-of-mass energy of 13 TeV, corresponding to an integrated luminosity of $1.7\,\mathrm{fb}^{-1}$. The analysis is currently under internal review of the collaboration and the value of A_Γ is blinded.

[4] In this analysis, the D^0 meson is supposed to be produced in the pp primary vertex in order to improve its decay time resolution, an assumption that is clearly not true for secondary decays.

Chapter 1

CP violation in the charm sector and definition of A_Γ

This chapter introduces the phenomenology of CP violation in the standard model of particle physics, with a particular focus on the phenomenon of the mixing of the neutral flavoured mesons and on the charm sector. Finally, the A_Γ observable is presented.

1.1 Introduction

The CP transformation is defined as the combination of the charge conjugation (C) and the parity (P) transformations, where C reverses the sign of all the internal quantum numbers of the particles and P reverses their spatial coordinates and, consequently, their handedness. Classically, both C and P were considered to be exact symmetries of nature. Therefore, also CP would have been conserved and, as a consequence, matter would have been completely indistinguishable from antimatter.

So far, no experimental evidence was found that the electromagnetic and the strong interactions violate C or P. On the contrary, the weak interaction was shown to violate P and C in the strongest possible way, the W boson being coupled only to left-handed particles and right-handed antiparticles. Initially, the CP symmetry was believed to be preserved by the weak interactions, a fact that is actually approximately true for most weak decays. However, CP violation (CPV) was observed in 1964 in the decay of kaons [8], allowing for the first time to distinguish unambiguously matter from antimatter. This discovery was the reason why the third generation of quarks was postulated, as CPV would not have been possible within the paradigm of the standard model of particle physics (SM) if only two generations of quarks existed, and was fundamental for the emergence of the current formulation of the SM.

Today, the only source of CPV within the SM, namely the irreducible complex phase that is needed in the parametrisation of the CKM quark mixing matrix,[1] that quantifies the couplings between the quarks, is known at a good level of accuracy. However, high precision measurements of CPV are still of great importance and are pursued in dedicated experiments like LHCb. In fact, CPV effects might be enhanced by contributions from the new interactions beyond the SM whose discovery is currently the main aim of the particle physics community, and might manifest themselves also at energies much lower than the typical energy scale of the new particles and interactions.

[1]The conservation of the CP symmetry by the strong interaction, actually, is not guaranteed by the SM. However, no evidence of CPV has been detected so far in Quantum Chromodynamics (QCD) and the coefficient of the CP-violating term of the Lagrangian of the QCD is measured to be $\theta_{\text{QCD}} < 10^{-10}$ [9]. This absence of CPV in the strong interaction is often referenced as the *strong CP problem*.

The flavoured neutral mesons constitute a privileged laboratory for the study of the *CPV*, as they represent the only case where *CPV* can be observed in the full variety of its aspects. In the following sections, the rich phenomenology of mixing in flavoured neutral mesons is described, and the standard classification of *CPV* is introduced. Finally, a detailed presentation of the parameter A_Γ, that quantifies the indirect *CPV* of the decays of the D^0 meson in two charged hadrons—$D^0 \to K^+K^-$ or $D^0 \to \pi^+\pi^-$—which are the subject of this thesis, is given.

1.2 Flavoured neutral mesons mixing

In the SM there are exactly four neutral mesons (plus their antiparticles) which are unable to decay into lighter particles *via* electromagnetic or strong interaction: the K^0 ($d\bar{s}$), D^0 ($c\bar{u}$), B^0 ($d\bar{b}$) and B_s^0 ($s\bar{b}$) mesons.[2] They are said to be *flavoured*, since they all possess non-null flavour quantum numbers. These particles are produced as flavour eigenstates either in combination with an opposite-flavoured hadron by the strong and electromagnetic interaction or as single mesons in the weak decay of heavier particles. However, owing to the violation of flavour quantum numbers by the weak interaction, the flavour eigenstates of the neutral mesons are not eigenstates of the free Hamiltonian governing their time evolution. As a consequence, flavoured neutral mesons have a non-null probability to oscillate into their antiparticles *via* a transition that changes their flavour quantum number by two units, the so called *mixing* phenomenon, before decaying.

In this section the mixing formalism for a generic flavoured neutral meson M^0 is introduced [3, 10]; then, the mixing phenomenology of the four different flavoured neutral mesons of the SM is briefly described.

1.2.1 Time evolution of flavour eigenstates

Let us consider an initial state which is a pure superposition of a neutral meson in its flavour eigenstate M^0 and of its antiparticle $\overline{M}^0$ (where M^0 can be equal to K^0, D^0, B^0, B_s^0):

$$|\psi(0)\rangle = a(0)\left|M^0\right\rangle + b(0)\left|\overline{M}^0\right\rangle .$$

As time passes, this state will evolve according to the Schrödinger equation,[3]

$$i\frac{\mathrm{d}}{\mathrm{d}t}\left|\psi(t)\right\rangle = H\left|\psi(t)\right\rangle ,$$

where H is the Hamiltonian governing its dynamics and $|\psi(t)\rangle$ is a linear superposition of $\left|M^0\right\rangle$, $\left|\overline{M}^0\right\rangle$ and all the final states $|f_k\rangle$ in which these two mesons can decay:

$$|\psi(t)\rangle = a(t)\left|M^0\right\rangle + b(t)\left|M^0\right\rangle + \sum_k c_k(t)\left|f_k\right\rangle .$$

If one is only interested in the values of $a(t)$ and $b(t)$ and not in the decays into final states different from $\left|M^0\right\rangle$ and $\left|\overline{M}^0\right\rangle$, and if the times t under consideration are much larger than the typical time scale of the strong interaction, the problem can be solved with a simplified formalism using the Wigner–Weisskopf approximation [10, 11]. This corresponds to considering the flavour-changing weak interaction as a perturbation to the strong one, and to evaluating the time evolution of the flavour eigenstates up to the second order in weak interactions. Then,

[2] The short lifetime of the t quark prevents it from hadronising into quark bound states; consequently, no hadrons containing the t quark exist.

[3] Natural units are adopted in this chapter, taking $c = \hbar = 1$.

Table 1.1: Constraints on the $\boldsymbol{\mathcal{H}}$ matrix elements in case of *CPT*, *CP* or *T* invariance of the interactions governing the time evolution of the M^0–$\overline{M}^0$ system.

Invariance	Constraints
CPT	$\mathrm{M}_{11} = \mathrm{M}_{22}, \quad \Gamma_{11} = \Gamma_{22}$
CP	$\mathrm{M}_{11} = \mathrm{M}_{22}, \quad \Gamma_{11} = \Gamma_{22}, \quad \mathcal{I}m(\Gamma_{12}/\mathrm{M}_{12}) = 0$
T	$\mathcal{I}m(\Gamma_{12}/\mathrm{M}_{12}) = 0$

the evolution of the state in the M^0–$\overline{M}^0$ subspace can be described with a 2×2 effective, non Hermitian Hamiltonian $\boldsymbol{\mathcal{H}}$:[4]

$$i\frac{\mathrm{d}}{\mathrm{d}t}\begin{pmatrix} a(t) \\ b(t) \end{pmatrix} = \begin{pmatrix} \mathcal{H}_{11} & \mathcal{H}_{12} \\ \mathcal{H}_{21} & \mathcal{H}_{22} \end{pmatrix}\begin{pmatrix} a(t) \\ b(t) \end{pmatrix}.$$

The complex effective Hamiltonian can in general be split into a Hermitian and an anti-Hermitian part

$$\boldsymbol{\mathcal{H}} := \mathbf{M} - \frac{i}{2}\boldsymbol{\Gamma},$$

where $\mathbf{M} = (\mathcal{H} + \mathcal{H}^\dagger)/2$ is usually referenced as the *mass matrix* and $\boldsymbol{\Gamma} = i(\mathcal{H} - \mathcal{H}^\dagger)$ as the *decay matrix*. $\mathbf{M}$ describes dispersive transitions through virtual (off-shell) intermediate states, and $\boldsymbol{\Gamma}$ absorptive transitions through real (on-shell) states.[5] $\boldsymbol{\Gamma}$ is responsible for the non-Hermiticity of $\boldsymbol{\mathcal{H}}$, and regulates the decay rate of the state from the M^0–$\overline{M}^0$ subspace: indicating the projection of $|\psi\rangle$ on this subspace with $|\psi^{(2)}\rangle$, it can be easily obtained that

$$\frac{\mathrm{d}}{\mathrm{d}t}\langle\psi^{(2)}|\psi^{(2)}\rangle = i\langle\psi^{(2)}|\left(\boldsymbol{\mathcal{H}}^\dagger - \boldsymbol{\mathcal{H}}\right)|\psi^{(2)}\rangle = -\langle\psi^{(2)}|\,\boldsymbol{\Gamma}\,|\psi^{(2)}\rangle\,.$$

As the right term must be negative, corresponding to the decay of the state $|\psi\rangle$ from the M^0–$\overline{M}^0$ subspace, $\boldsymbol{\Gamma}$ is positive definite.

The Hermiticity of $\mathbf{M}$ and $\boldsymbol{\Gamma}$ implies by definition that $\mathrm{M}_{ij} = \mathrm{M}^*_{ji}$ and $\Gamma_{ij} = \Gamma^*_{ji}$, so that $\boldsymbol{\mathcal{H}}$ is defined in general by eight free parameters. However, if the interactions described by $\boldsymbol{\mathcal{H}}$ are invariant under some combination of discrete transformations, further relations among the matrix elements of $\boldsymbol{\mathcal{H}}$ hold, as listed in Tab. 1.1, reducing the number of degrees of freedom. In the following, *CPT* invariance will be assumed, *i.e.* $\mathrm{M} := \mathrm{M}_{11} = \mathrm{M}_{22}$ and $\Gamma := \Gamma_{11} = \Gamma_{22}$.[6]

Let us define the $\boldsymbol{\mathcal{H}}$ eigenstates to be

$$\begin{aligned} |M_1\rangle &:= p\,|M^0\rangle + q\,|\overline{M}^0\rangle\,, \\ |M_2\rangle &:= p\,|M^0\rangle - q\,|\overline{M}^0\rangle\,, \end{aligned} \tag{1.1}$$

normalised imposing $|p|^2 + |q|^2 = 1$. As the matrix $\boldsymbol{\mathcal{H}}$ is not Hermitian, the two eigenstates are not necessarily orthogonal. The relative eigenvalues can be calculated to be

$$\lambda_{1,2} := m_{1,2} - \frac{i}{2}\Gamma_{1,2} = \mathrm{M} - \frac{i}{2}\Gamma \pm \frac{q}{p}\left(\mathrm{M}_{12} - \frac{i}{2}\Gamma_{12}\right) \tag{1.2}$$

so that

$$|M_{1,2}(t)\rangle = e^{-im_{1,2}t}e^{-\Gamma_{1,2}t/2}\,|M_{1,2}(0)\rangle\,, \tag{1.3}$$

[4] The non-Hermiticity of the $\boldsymbol{\mathcal{H}}$ matrix is a consequence of the fact that probability is not conserved in the M^0–$\overline{M}^0$ subspace.

[5] The explicit expressions for $\mathbf{M}$ and $\boldsymbol{\Gamma}$ can be found, for example, in Ref. [12].

[6] This choice, which simplifies the discussion of mixing, is justified by the central role of *CPT* invariance for the consistency of QFT and to the lack of experimental evidence for its violation.

with

$$\frac{q}{p} = \pm\sqrt{\frac{\mathrm{M}_{12}^* - \frac{i}{2}\Gamma_{12}^*}{\mathrm{M}_{12} - \frac{i}{2}\Gamma_{12}}}.$$

The sign of the square root in the last equation can be taken to be positive without loss of generality thanks to the arbitrariness of the sign of q in the definition (1.1). From Eq. (1.2), it can be seen that the following relations hold:

$$M = \frac{m_1 + m_2}{2}, \qquad \Gamma = \frac{\Gamma_1 + \Gamma_2}{2}.$$

The time evolution of a particle that was created in its flavour eigenstate at $t = 0$ can be easily obtained substituting Eq. (1.3) in the definition (1.1):

$$\begin{aligned} \left|M^0(t)\right\rangle &= g_+(t)\left|M^0\right\rangle + \frac{q}{p}\, g_-(t)\left|\overline{M}^0\right\rangle, \\ \left|\overline{M}^0(t)\right\rangle &= g_+(t)\left|\overline{M}^0\right\rangle + \frac{p}{q}\, g_-(t)\left|M^0\right\rangle, \end{aligned} \tag{1.4}$$

where $|\overset{(-)}{M}{}^0(t)\rangle$ indicates the time-evolution at time t of a state that corresponded to a flavour eigenstate $|\overset{(-)}{M}{}^0\rangle$ at $t = 0$ and

$$g_\pm(t) = \frac{e^{-i\lambda_1 t} \pm e^{-i\lambda_2 t}}{2}. \tag{1.5}$$

From Eq. 1.4, it follows that the probability of measuring at time t a state with the same flavour quantum numbers with which the state was produced at time $t = 0$ is

$$\begin{aligned} \mathrm{Prob}(M^0, t = 0 \to M^0, t) &= \left|\left\langle M^0(t)\middle|M^0\right\rangle\right|^2 = \left|g_+(t)\right|^2, \\ \mathrm{Prob}(\overline{M}^0, t = 0 \to \overline{M}^0, t) &= \left|\left\langle \overline{M}^0(t)\middle|\overline{M}^0\right\rangle\right|^2 = \left|g_+(t)\right|^2, \end{aligned}$$

whereas the probability of measuring the state with opposite flavour quantum numbers is

$$\begin{aligned} \mathrm{Prob}(M^0, t = 0 \to \overline{M}^0, t) &= \left|\left\langle M^0(t)\middle|\overline{M}^0\right\rangle\right|^2 = \left|\frac{q}{p}\right|^2 \cdot \left|g_-(t)\right|^2, \\ \mathrm{Prob}(\overline{M}^0, t = 0 \to M^0, t) &= \left|\left\langle \overline{M}^0(t)\middle|M^0\right\rangle\right|^2 = \left|\frac{p}{q}\right|^2 \cdot \left|g_-(t)\right|^2, \end{aligned} \tag{1.6}$$

with

$$\begin{aligned} \left|g_\pm(t)\right|^2 &= \frac{1}{2}e^{-\Gamma t}\left[\cosh\left(\frac{\Delta\Gamma t}{2}\right) \pm \cos\left(\Delta m t\right)\right], \\ \Delta m &:= m_2 - m_1 = -2\,\mathcal{R}e(\sqrt{\mathcal{H}_{12}\mathcal{H}_{21}}), \\ \Delta\Gamma &:= \Gamma_2 - \Gamma_1 = 4\,\mathcal{I}m(\sqrt{\mathcal{H}_{12}\mathcal{H}_{21}}). \end{aligned}$$

The last equation is often rewritten in terms of two dimensionless *mixing parameters* $x := \Delta m/\Gamma$ and $y := \Delta\Gamma/2\Gamma$:

$$\left|g_\pm(t)\right|^2 = \frac{1}{2}e^{-\Gamma t}\left[\cosh(y\Gamma t) \pm \cos(x\Gamma t)\right]$$

In particular, it is worth noting that the probability of the M^0 and $\overline{M}^0$ mesons to preserve their flavour quantum numbers over time is the same for both mesons, whereas the probability to oscillate in their antiparticle can be different, provided that $|q/p| \neq 1$.

Table 1.2: Approximate mixing parameters of the four flavoured neutral meson systems (values taken from [10] for kaons and from [3] for c and b mesons).

System	$x = \Delta m/\Gamma$	$y = \Delta\Gamma/2\Gamma$
K^0–$\overline{K}^0$	-0.95	0.997
D^0–$\overline{D}^0$	0.003	0.007
B^0–$\overline{B}^0$	0.77	-0.001
B^0_s–$\overline{B}^0_s$	26.7	0.06

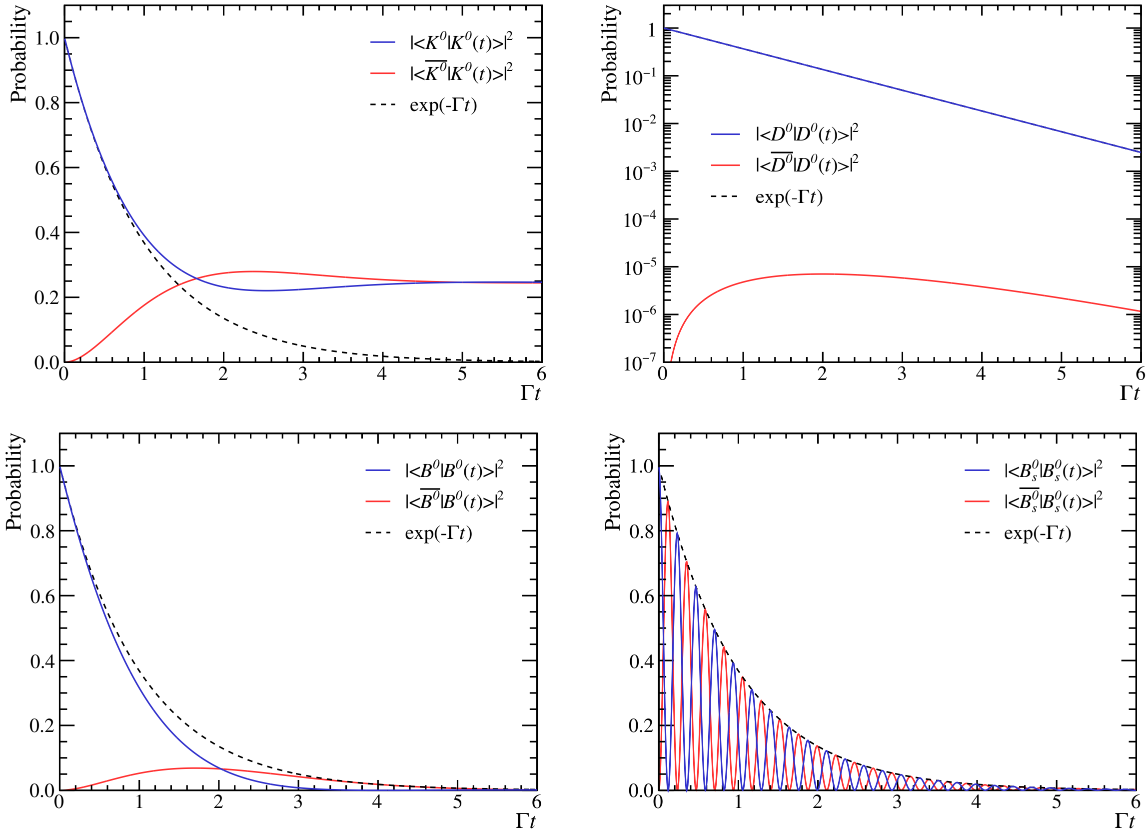

Figure 1.1: Probability for a neutral meson to oscillate in its relative antimeson (red) or to preserve its flavour quantum numbers (blue) as a function of its proper time, in the approximation that $|q/p| = 1$, for the four flavoured neutral meson systems where mixing is observed. From left to right and from top to bottom: K^0–$\overline{K}^0$, D^0–$\overline{D}^0$ (in logarithmic scale), B^0–$\overline{B}^0$ and B^0_s–$\overline{B}^0_s$ systems. The exponential function that would be measured in absence of mixing is also drawn (black-dashed line).

1.2.2 Mixing phenomenology

Although the formalism is the same for all K^0, D^0, B^0 and B^0_s mesons, the phenomenologies of their mixing are very different, owing to the different matrix elements of the effective Hamiltonian $\mathcal{H}$, resulting in different mixing parameters x and y, as shown in Tab. 1.2. The resulting probability, as a function of the decay time, for the mesons to preserve their flavour quantum numbers or to change them, oscillating into their antiparticles, is represented in Fig. 1.1. In particular, the mixing between the D^0 and $\overline{D}^0$ mesons is very slow, the probability over time of the D^0 meson to preserve its flavour quantum numbers being almost indistinguishable from an exponential function.

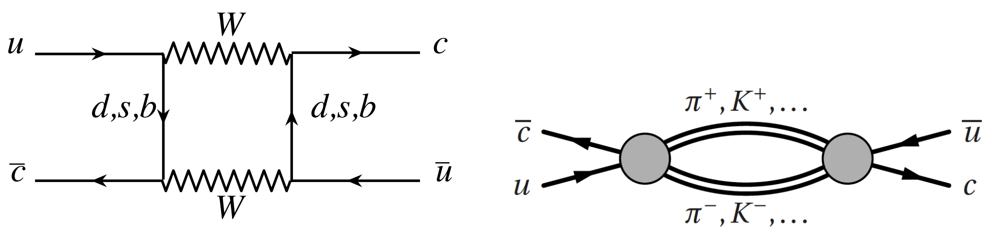

Figure 1.2: Graphical representation of short (left) and long (right) distance contributions to the D^0 mixing.

The dynamics behind the values of x and y is enclosed in the effective Hamiltonian governing the specific system. In general, there are two types of contributions to the mixing amplitudes: the *short distance* and the *long distance* contributions. The short distance contributions are fourth order interactions in the weak coupling, as represented by the Feynman diagram drawn in Fig. 1.2 (left). They are called short distance contribution since their typical scale length is much lower than that of the strong interaction. However, these contributions are strongly suppressed in the charm system, contrary to the B systems where the analogous box diagrams are dominant. In fact, the contribution of the b quark in the charm box diagram (Fig. 1.2 left), is CKM-suppressed by a factor of $|V_{ub}V^*_{cb}|^2/|V_{us}V^*_{cs}|^2 \approx 10^{-5}$. The contribution from down and strange quarks is also strongly suppressed in the limit of SU(3) flavour symmetry [2, 13], by the GIM suppression mechanism. Even taking into account the next-to-leading order diagrams, the short distance contributions to the mixing parameters x and y of the D^0 meson are predicted to be about $\mathcal{O}(10^{-6})$ [14]. These values are far below the current experimentally measured values of x and y [15–19], $\lesssim \mathcal{O}(10^{-2})$, thus the long distance contributions are dominant in the D^0–$\overline{D}^0$ mixing.

In fact, mixing can proceed through intermediate on-shell states common to the D^0 and the $\overline{D}^0$ mesons, as schematically represented in the right part of Fig. 1.2, the so-called long distance contributions. The size of the long distance contributions is determined by the amount of the phase space of the final states which is shared by the meson and the anti-meson. In the K^0–$\overline{K}^0$ system this contribution is almost maximal, since there is a small number of possible final states for the K^0 decays and almost all of them are accessible also to the $\overline{K}^0$. In the B systems the situation is the opposite, since there is a large number of possible final states for the B mesons, but just a small fraction of them are also accessible to the $\overline{B}$ ones. Unfortunately, precise calculations of long distance effects for the D^0 meson are difficult and are characterised by large uncertainties, since the value of the mass of the charm quark is placed somewhat halfway between the heavy and the light quark systems, where two different kinds of approximations are usually made. Inclusive approaches such as heavy quark effective field theory rely on power series expansions of the inverse of the quark mass, which are extensively used for the B mesons but are of limited validity in the charm case because of the intermediate value of its mass [20, 21]. Alternatively, exclusive approaches are used [22, 23], trying to account explicitly for all possible intermediate states, which may be modelled or fitted directly to the experimental data. However, the D^0 meson is not light enough to have few final states, and in the absence of sufficiently precise measurements of amplitudes and strong phases of many decays, several assumptions are made, limiting the precision of the predictions of this approach. As a consequence, theoretical predictions of the D^0–$\overline{D}^0$ mixing parameters (and *CPV* parameters) are very challenging, and several orders of magnitude are spanned in the literature [24]. Therefore, it is crucial to provide very precise measurements in the charm sector in order to improve them.

1.3 Origin of CP violation in particle decays

In general, a state $|f\rangle$ transforms, under the CP operator, as $CP\,|f\rangle = \omega_f\,|\overline{f}\rangle$, where ω_f is a complex phase ($|\omega_f| = 1$), whereas the analogous transformation for its antiparticle is $CP\,|\overline{f}\rangle = \omega_f^*\,|f\rangle$. In the particular case that f is a CP eigenstate (for example $f = K^+K^-$ or $f = \pi^+\pi^-$), one obtains

$$CP\,|f\rangle = \eta_{CP}(f)\,|f\rangle\,,$$

with $\eta_{CP}(f) = \pm 1$ for CP-even and CP-odd states, respectively. Let us consider a neutral meson M^0. Its decay amplitudes into final state f can be defined as

$$A_f := \langle f|\,\mathcal{H}\,|M^0\rangle\,, \quad \bar{A}_f := \langle f|\,\mathcal{H}\,|\overline{M}^0\rangle\,,$$

where $\mathcal{H}$ is the decay Hamiltonian of the M^0 meson. In general, two types of phases can enter in these amplitudes:

- *weak phases*, coming from any complex term in the Lagrangian governing the system, therefore appearing as complex conjugate in the CP-conjugate amplitude. As a consequence, weak phases have opposite signs for A_f and $\bar{A}_f$. They are referenced as weak because the only complex phase of the Lagrangian of the SM is that relative to the CKM matrix, governing the weak transitions between quarks;

- *strong phases*, coming from final state interactions and contributing to the amplitudes through intermediate on-shell states in the decay process. These phases arise also if the Lagrangian is real and are often called "scattering phases". They are typically generated by the strong interaction, whenever there are hadrons in the final state; therefore, they are referenced as "strong phases". Their fundamental characteristic is that they do not change sign under the action of the CP operator.

All the known observables depend on squared amplitudes, so that the phases are not observable. However, differences between phases can be observed through the interference of different amplitudes. Similarly, CPV in the decay appears only through the interference of different decay amplitudes, provided that at least two of them are characterised by different weak and strong phases.

As an example, let us consider a decay process which can proceed through several amplitudes a_i,

$$A_f = \sum_i |a_i|\,e^{i(\phi_i+\delta_i)}, \qquad \bar{A}_f = \sum_i |a_i|\,e^{i(-\phi_i+\delta_i)},$$

where ϕ_i are the weak phases, which change sign under CP, and δ_i are the strong ones, which do not change sign under CP. The difference between the two squared amplitudes is:

$$|A_f|^2 - |\bar{A}_f|^2 = -2\sum_{i,j} |a_i|\,|a_j|\sin(\phi_i - \phi_j)\sin(\delta_i - \delta_j).$$

By definition, one needs $|A_f| \neq |\bar{A}_f|$ to observe CPV, requiring at least two amplitudes with different weak and strong phases in order to have a non-vanishing interference term.

1.4 CP violation in flavoured neutral mesons

Experimentally, there are three possible manifestations of CPV in the decay of flavoured neutral mesons. They are separately described, one at a time, in the following subsections.

1.4.1 *CP* violation in the decay

CPV in the decay (also referenced as direct *CPV*) occurs if the magnitudes of the decay amplitudes of *CP*-conjugated processes are not equal. This type of *CPV* is usually quantified with the direct *CP* asymmetry, defined as

$$A_{CP}^{\mathrm{dir}} = \frac{|A_f|^2 - |\bar{A}_{\bar{f}}|^2}{|A_f|^2 + |\bar{A}_{\bar{f}}|^2} = \frac{1-R_f^2}{1+R_f^2}, \tag{1.7}$$

where

$$R_f := \left|\frac{\bar{A}_{\bar{f}}}{A_f}\right|$$

is the magnitude of the ratio between the decay amplitudes of the *CP*-conjugated decays $\overline{M}^0 \to \bar{f}$ and $M^0 \to f$.[7] The *CPV* in the decay occurs if and only if $R_f \neq 1$.

1.4.2 *CP* violation in the mixing

CPV in the mixing occurs if the probability of the M^0 meson to oscillate after a time t into its anti-meson $\overline{M}^0$ is different from that for the *CP*-conjugate process, where a $\overline{M}^0$ oscillates into a M^0. Eq. (1.6) implies that this happens if and only if the magnitude of the ratio between the coefficients of M^0 and $\overline{M}^0$ for the mass eigenstates of the flavoured neutral mesons is different from 1,

$$R_m := \left|\frac{q}{p}\right| \neq 1.$$

1.4.3 *CP* violation in the interference

If a final state f is shared by the M^0 and $\overline{M}^0$ mesons,[8] then the *CP* symmetry can be violated by the interference between the decay without mixing, $M^0 \to f$, and that with mixing, $M^0 \to \overline{M}^0 \to f$. This condition occurs when

$$\mathcal{I}m(\lambda_f) + \mathcal{I}m(\lambda_{\bar{f}}) \neq 0, \tag{1.8}$$

with

$$\lambda_f := \frac{q}{p}\frac{\bar{A}_f}{A_f}.$$

For final *CP* eigenstates, such as K^+K^- and $\pi^+\pi^-$, the condition of Eq. 1.8 simplifies to

$$\mathcal{I}m(\lambda_f) \neq 0.$$

In this case, λ_f is usually written as

$$\lambda_f := \frac{q}{p}\frac{\bar{A}_f}{A_f} = -\eta_{CP}(f) R_m R_f e^{i\phi_f}, \tag{1.9}$$

where $\eta_{CP}(f)$ is the *CP*-parity of the f final state and

$$\phi_f := \arg\left(-\eta_{CP}(f)\cdot\frac{q}{p}\frac{\bar{A}_f}{A_f}\right).$$

Then, the condition to have *CPV* in the interference is expressed by $\phi_f \neq \{0, \pi\}$.

[7] This is the only type of *CPV* that can be observed also in charged hadrons.
[8] In particular, this is verified by all *CP* eigenstates.

1.5 CP violation in the D^0 system

Since the main subject of this thesis are the singly Cabibbo-suppressed decays $D^0 \to K^+K^-$ and $D^0 \to \pi^+\pi^-$, the discussion is now specialised to the time-dependent decay rates of the D^0 and $\overline{D}^0$ mesons into these final states, which are referenced in general with the symbol f. The notation follows that of Ref. [3, 10].

1.5.1 Decay rates

The time-dependent rates of the D^0 and $\overline{D}^0$ decays into final state f are defined as

$$\Gamma(D^0(t) \to f) = \mathcal{N}_f \left| \langle f|H|D^0(t)\rangle \right|^2, \qquad \Gamma(\overline{D}^0(t) \to f) = \mathcal{N}_f \left| \langle f|H|\overline{D}^0(t)\rangle \right|^2,$$

where $\mathcal{N}_f$ is a common, time-independent normalisation factor that includes the result of the phase space integration and H is the effective Hamiltonian governing the decay of the D mesons. Substituting the results of Eq. (1.4), one obtains

$$\Gamma(D^0(t) \to f) = \mathcal{N}_f \left| g_+(t)A_f + \frac{q}{p} g_-(t)\bar{A}_f \right|^2, \qquad \Gamma(\overline{D}^0(t) \to f) = \mathcal{N}_f \left| \frac{p}{q} g_-(t)A_f + g_+(t)\bar{A}_f \right|^2.$$

Then, substituting the definitions of $g_\pm(t)$, Eq. (1.5, 1.2), and using the definition of λ_f, Eq. (1.9), these expressions can be rewritten as

$$\begin{aligned}
\Gamma(D^0(t) \to f) &= \frac{\mathcal{N}_f}{2} e^{-\Gamma t} |A_f|^2 \big[(1 + |\lambda_f|^2) \cosh(y\Gamma t) + (1 - |\lambda_f|^2) \cos(x\Gamma t) \\
&\qquad + 2\,\mathcal{R}e(\lambda_f) \sinh(y\Gamma t) - 2\,\mathcal{I}m(\lambda_f) \sin(x\Gamma t)\big], \\
\Gamma(\overline{D}^0(t) \to f) &= \frac{\mathcal{N}_f}{2} e^{-\Gamma t} |\bar{A}_f|^2 \big[(1 + |\lambda_f^{-1}|^2) \cosh(y\Gamma t) + (1 - \left|\lambda_f^{-1}\right|^2) \cos(x\Gamma t) \\
&\qquad + 2\,\mathcal{R}e(\lambda_f^{-1}) \sinh(y\Gamma t) - 2\,\mathcal{I}m(\lambda_f^{-1}) \sin(x\Gamma t)\big] \\
&= \frac{\mathcal{N}_f}{2} e^{-\Gamma t} |A_f|^2 \left|\frac{p}{q}\right|^2 \big[(1 + |\lambda_f|^2) \cosh(y\Gamma t) - (1 - |\lambda_f|^2) \cos(x\Gamma t) \\
&\qquad + 2\,\mathcal{R}e(\lambda_f) \sinh(y\Gamma t) + 2\,\mathcal{I}m(\lambda_f) \sin(x\Gamma t)\big].
\end{aligned} \tag{1.10}$$

1.5.2 Effective decay widths

Since both mixing parameters x and y are $< 10^{-2}$ [3], the Eq. (1.10) can be expanded to the first order in $x\Gamma t$ and $y\Gamma t$ in the time range $\Gamma t \sim \mathcal{O}(1 - 10)$, obtaining

$$\begin{aligned}
\Gamma(D^0(t) \to f) &= \mathcal{N}_f e^{-\Gamma t} |A_f|^2 \big[1 + \mathcal{R}e(\lambda_f) y\Gamma t - \mathcal{I}m(\lambda_f) x\Gamma t + \mathcal{O}\big((x\Gamma t)^2\big) + \mathcal{O}\big((y\Gamma t)^2\big)\big]. \\
\Gamma(\overline{D}^0(t) \to f) &= \mathcal{N}_f e^{-\Gamma t} |\bar{A}_f|^2 \big[1 + \mathcal{R}e(\lambda_f^{-1}) y\Gamma t - \mathcal{I}m(\lambda_f^{-1}) x\Gamma t + \mathcal{O}\big((x\Gamma t)^2\big) + \mathcal{O}\big((y\Gamma t)^2\big)\big].
\end{aligned}$$

Expanding λ_f according to Eq. (1.9), one obtains

$$\begin{aligned}
\Gamma(D^0(t) \to f) &\approx \mathcal{N}_f e^{-\Gamma t} |A_f|^2 \big[1 - \eta_f^{CP} R_m R_f (y \cos\phi_f - x \sin\phi_f)\Gamma t\big], \\
\Gamma(\overline{D}^0(t) \to f) &\approx \mathcal{N}_f e^{-\Gamma t} |\bar{A}_f|^2 \big[1 - \eta_f^{CP} R_m^{-1} R_f^{-1} (y \cos\phi_f + x \sin\phi_f)\Gamma t\big].
\end{aligned}$$

The above time dependencies can be approximated at first order with a pure exponential form, using the relation $e^{-\Gamma t}(1 - z\Gamma t + \mathcal{O}\big((z\Gamma t)^2\big)) \approx e^{-\hat{\Gamma} t}$, that holds at first order for $|z| \ll 1$, defining $\hat{\Gamma} := \Gamma(1 + z)$. The resulting effective decay widths,

$$\begin{aligned}
\hat{\Gamma}(D^0(t) \to f) &= \Gamma\big[1 + \eta_f^{CP} R_m R_f (y \cos\phi_f - x \sin\phi_f)\big], \\
\hat{\Gamma}(\overline{D}^0(t) \to f) &= \Gamma\big[1 + \eta_f^{CP} R_m^{-1} R_f^{-1} (y \cos\phi_f + x \sin\phi_f)\big],
\end{aligned} \tag{1.11}$$

are the decay widths that are measured when modelling the time distribution of the decays with a simple exponential function.

1.5.3 Time-dependent *CP* asymmetry

The time-dependent *CP* asymmetry is defined as the asymmetry between the decay rates of the D^0 and $\overline{D}^0$ mesons into final state f,

$$A_{CP}(t) := \frac{\Gamma(D^0(t)\to f) - \Gamma(\overline{D}^0(t)\to f)}{\Gamma(D^0(t)\to f) + \Gamma(\overline{D}^0(t)\to f)}. \tag{1.12}$$

Substituting the values of the time-dependent rates from Eq. (1.10), it follows that

$$\begin{aligned} A_{CP}(t) = \big[&(R_m^2-1)(1+|\lambda_f|^2)\cosh(y\Gamma t) + (R_m^2+1)(1-|\lambda_f|^2)\cos(x\Gamma t) \\ &+ 2(R_m^2-1)\mathcal{R}e(\lambda_f)\sinh(y\Gamma t) - 2(R_m^2+1)\mathcal{I}m(\lambda_f)\sin(x\Gamma t)\big]/ \\ \big[&(R_m^2+1)(1+|\lambda_f|^2)\cosh(y\Gamma t) + (R_m^2-1)(1-|\lambda_f|^2)\cos(x\Gamma t) \\ &+ 2(R_m^2+1)\mathcal{R}e(\lambda_f)\sinh(y\Gamma t) - 2(R_m^2-1)\mathcal{I}m(\lambda_f)\sin(x\Gamma t)\big] \end{aligned}$$

Using the same approximation utilised in the previous section, since the mixing parameters x and y are $< 10^{-2}$, this expression can be expanded to the first order in $x\Gamma t$ and $y\Gamma t$, obtaining

$$A_{CP}(t) = A_{CP}^{\text{dir}} + A_{CP}^{\text{ind}}\cdot\Gamma t + \mathcal{O}\big((x\Gamma t)^2\big) + \mathcal{O}\big((y\Gamma t)^2\big), \tag{1.13}$$

where the constant term A_{CP}^{dir}, defined in Eq. (1.7), is different from zero if and only if *CPV* in the decay is present ($R_f \neq 1$). On the contrary, the slope of $A_{CP}(t)$ is

$$A_{CP}^{\text{ind}} := -\frac{2\eta_f^{CP}R_f^2}{(1+R_f^2)^2}\left[(R_mR_f - R_m^{-1}R_f^{-1})y\cos\phi_f - (R_mR_f + R_m^{-1}R_f^{-1})x\sin\phi_f\right] \tag{1.14}$$

and is sensitive to all three types of *CPV*:[9] *CPV* in the decay ($|R_f| \neq 1$), in the mixing ($|R_m| \neq 1$) and the interference between the decay and the mixing ($\phi_f \notin \{0, \pi\}$).

1.5.4 Observables of the time-dependent *CPV* in the charm sector

The two observables that have produced the most precise measurements of the time-dependent *CPV* in the charm sector are defined as

$$\begin{aligned} A_\Gamma &:= \frac{\hat\Gamma(D^0\to f) - \hat\Gamma(\overline{D}^0\to f)}{\hat\Gamma(D^0\to f) + \hat\Gamma(\overline{D}^0\to f)}, \\ y_{CP} &:= \frac{\hat\Gamma(D^0\to f) + \hat\Gamma(\overline{D}^0\to f)}{2\Gamma} - 1, \end{aligned} \tag{1.15}$$

where $\hat\Gamma$ is the effective decay width that is measured by modelling the decay rate distribution of the meson decays into final state f with a simple exponential function. In particular, A_Γ can be rewritten as

$$A_\Gamma = \frac{\hat\Gamma(D^0\to f) - \hat\Gamma(\overline{D}^0\to f)}{2\Gamma(1+y_{CP})} \approx \frac{\hat\Gamma(D^0\to f) - \hat\Gamma(\overline{D}^0\to f)}{2\Gamma}$$

where $y_{CP} < 10^{-2}$ [3] is neglected. Finally, substituting in the previous expression the effective decay widths from Eq. (1.11), one finds

$$\begin{aligned} A_\Gamma &= \frac{\eta_{CP}(f)}{2}\left[(R_mR_f - R_m^{-1}R_f^{-1})y\cos\phi_f - (R_mR_f + R_m^{-1}R_f^{-1})x\sin\phi_f\right], \\ y_{CP} &= \frac{\eta_{CP}(f)}{2}\left[(R_mR_f + R_m^{-1}R_f^{-1})y\cos\phi_f - (R_mR_f - R_m^{-1}R_f^{-1})x\sin\phi_f\right]. \end{aligned}$$

[9] Note that Eq. (1.13) is the definition of A_{CP}^{ind}.

The A_Γ parameter is therefore related to the indirect *CPV* defined in Eq. (1.14) as follows,

$$A_\Gamma = -\frac{1}{4}\frac{\left(1+R_f^2\right)^2}{R_f^2}A_{CP}^{\rm ind} \approx -A_{CP}^{\rm ind}.$$

where the current experimental values for the direct *CPV* ($A_{CP}^{\rm dir}(D^0 \to K^+K^-) = (0.01 \pm 0.14)\cdot 10^{-2}$ and $A_{CP}^{\rm dir}(D^0 \to \pi^+\pi^-) = (-0.11 \pm 0.13)\cdot 10^{-2}$ [3, 10]) allow neglecting the *CPV* in the decay, assuming $R_f \approx 1$. In this approximation, $A_\Gamma \approx -A_{CP}^{\rm ind}$, and the *CP* asymmetry $A_{CP}(t)$ of Eq. (1.12) can be rewritten as

$$A_{CP}(t) = A_{CP}^{\rm dir} - A_\Gamma \frac{t}{\tau(D^0)}, \tag{1.16}$$

where $\tau(D^0) := \frac{1}{\Gamma}$ can be measured as the lifetime of the flavour-specific $D^0 \to K^-\pi^+$ decay mode. In the same approximation ($R_f \approx 1$), A_Γ and y_{CP} can be rewritten as

$$\begin{aligned} A_\Gamma &= \frac{\eta_{CP}(f)}{2}\left[\left(\left|\frac{q}{p}\right| - \left|\frac{p}{q}\right|\right) y\cos\phi_f - \left(\left|\frac{q}{p}\right| + \left|\frac{p}{q}\right|\right) x\sin\phi_f\right], \\ y_{CP} &= \frac{\eta_{CP}(f)}{2}\left[\left(\left|\frac{q}{p}\right| + \left|\frac{p}{q}\right|\right) y\cos\phi_f - \left(\left|\frac{q}{p}\right| - \left|\frac{p}{q}\right|\right) x\sin\phi_f\right]. \end{aligned} \tag{1.17}$$

From this expression, it is clear that A_Γ receives both a contribution from *CPV* in the mixing, proportional to $y\cos\phi_f$ and vanishing only in the case that $|q| = |p|$, and one from *CPV* in the interference, that is null if and only if $\phi_f = \{0, \pi\}$. Therefore, a non-null value of A_Γ unequivocally indicates the presence of indirect *CPV*. On the contrary, the y_{CP} parameter is non-null also in the case of the absence of *CPV* in the charm sector, in which case it is expected to be equal to the mixing parameter y. In the limit of no *CPV* in the decay, the A_Γ and the y_{CP} parameters are necessary and sufficient in order to quantify both the amount of *CPV* in the mixing and in the interference.

1.5.5 Universality

In the expression for A_Γ of Eq. (1.17), whereas x, y, p and q are independent of the final state of the decay, the angle

$$\phi_f = \arg\left(\frac{q}{p}\frac{\bar{A}_f}{A_f}\right)$$

can in general depend on the final state through the phase $\arg(\bar{A}_f/A_f)$. Therefore, A_Γ could depend on the final state, too. In general, the decay amplitudes into final state f can be factorised as

$$\begin{aligned} A_f &= A_f^T e^{+i\phi_f^T}\left[1 + r_f e^{i(\delta_f + \phi_f)}\right] \\ \eta_{CP}(f)\bar{A}_f &= A_f^T e^{-i\phi_f^T}\left[1 + r_f e^{i(\delta_f - \phi_f)}\right] \end{aligned}$$

where $A_f^T e^{+i\phi_f^T}$ is the SM tree level amplitude, its weak phase ϕ_f^T excluded, r_f is the ratio between the magnitude of the sum of all the non-tree diagrams of the SM to that of the tree diagram, and ϕ_f and δ_f the weak and strong phases of this sum, relative to the tree amplitude [1, 25]. Since electroweak loop (penguin) diagrams are suppressed by a factor larger than 10^6 with respect to the tree level one [26], r_f can be neglected, obtaining

$$\frac{\bar{A}_f}{A_f} \approx \eta_{CP}(f)e^{-2i\phi_f^T}.$$

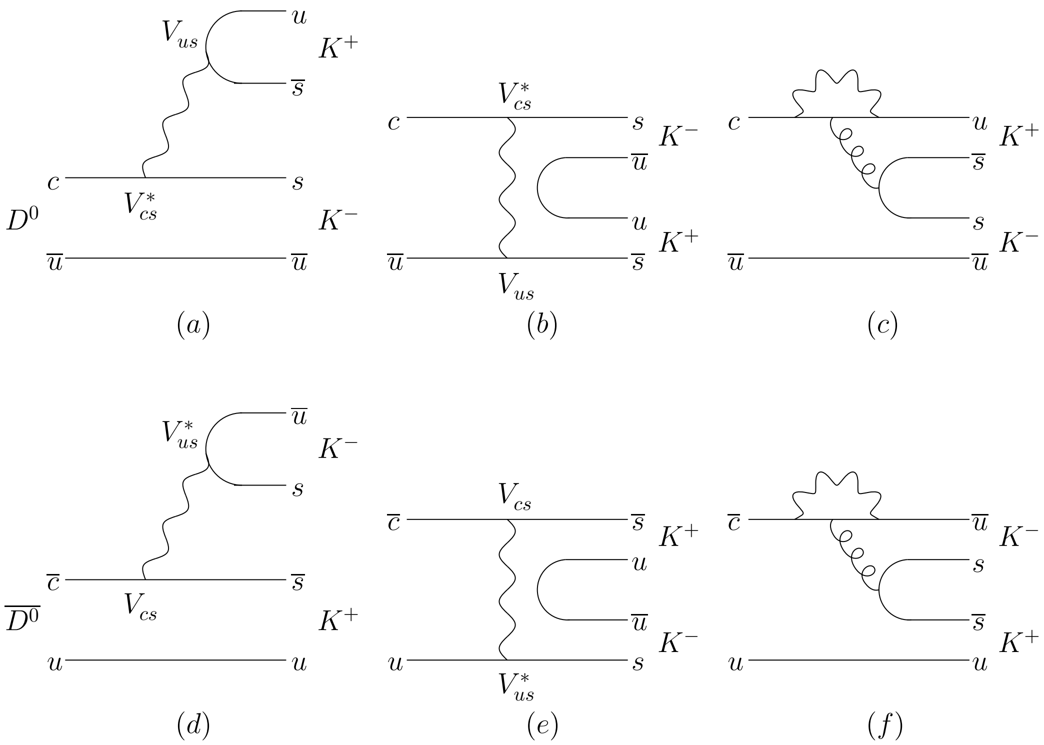

Figure 1.3: Tree diagrams (a,b) [(d,e)] and electroweak loop diagram (c) [(f)] for the $D^0 \to K^+K^-$ [$\overline{D}^0 \to K^+K^-$] decay (figure taken from Ref. [26]); the loop diagrams are suppressed with respect to the tree diagrams by a factor larger than 10^6. The two tree diagrams share the same CKM matrix elements (being only *CP*-conjugated for the $\overline{D}^0 \to K^+K^-$ decays). Therefore, $\frac{\bar{A}(K^+K^-)}{A(K^+K^-)} \approx \eta_{CP}(K^+K^-)\frac{V_{us}^*V_{cs}}{V_{us}V_{cs}^*} = \eta_{CP}(K^+K^-) = +1$, since all the CKM elements under consideration can be taken to be real.

Finally, since at tree level the decays of the D^0 meson involve only transitions between the first two generations of quarks, and the relative elements of the CKM matrix can be taken to be real, for example adopting the Wolfenstein parametrisation, the weak phase ϕ_f^T must be equal to 0 or to π—an example of this general fact is reported, for the $D^0 \to K^+K^-$ decay, in Fig. 1.3—. Therefore, $\bar{A}_f/A_f \approx \eta_{CP}(f)$ and

$$\lambda_f \approx -\eta_{CP}(f)R_m e^{i\phi_D} \tag{1.18}$$

where $\phi_D := \arg(-\eta_{CP}(f)\cdot q/p)$ is the relative weak phase between the mixing and the decay and is universal for all D^0 decays into *CP*-even (*CP*-odd) final states, with a relative phase of π between the *CP*-even and *CP*-odd final states. Since both the K^+K^- and the $\pi^+\pi^-$ final states are *CP*-even, A_Γ and y_{CP} are expected to be equal for these decays in the approximations described in this section, and can be written as

$$\begin{aligned} A_\Gamma &= \frac{\eta_{CP}(f)}{2}\left[\left(\left|\frac{q}{p}\right| - \left|\frac{p}{q}\right|\right) y\cos\phi_D - \left(\left|\frac{q}{p}\right| + \left|\frac{p}{q}\right|\right) x\sin\phi_D\right], \\ y_{CP} &= \frac{\eta_{CP}(f)}{2}\left[\left(\left|\frac{q}{p}\right| + \left|\frac{p}{q}\right|\right) y\cos\phi_D - \left(\left|\frac{q}{p}\right| - \left|\frac{p}{q}\right|\right) x\sin\phi_D\right], \end{aligned} \tag{1.19}$$

where the universality holds only in the SM.

The current experimental values of the mixing and *CPV* parameters for the charm sector, resulting from the average of all the measurements performed worldwide so far, are [3]

$$\begin{aligned} x &= (3.2 \pm 1.4) \cdot 10^{-3}, \\ y &= (6.9\,^{+0.6}_{-0.7}) \cdot 10^{-3}, \\ |q/p| &= 0.89\,^{+0.08}_{-0.07}, \\ \phi_D &= (-12.9\,^{+9.9}_{-8.7})^\circ, \\ A_\Gamma &= (-3.2 \pm 2.6) \cdot 10^{-4}, \\ y_{CP} &= (8.35 \pm 1.55) \cdot 10^{-3}. \end{aligned}$$

Furthermore, if direct *CPV* in the doubly Cabibbo-suppressed $D^0 \to K^+\pi^-$ decays is neglected, tighter constraints are obtained for $|q/p|$ and ϕ_D [10]:

$$\begin{aligned} 1 - |q/p| &= (-0.2 \pm 1.4) \cdot 10^{-2}, \\ \phi_D &= (-0.1 \pm 0.6)^\circ. \end{aligned}$$

Under this assumption, the measurement of A_Γ translates directly into the measurement of the phase ϕ_D:

$$A_\Gamma \approx -\eta_{CP}(f) \cdot x \sin\phi_D.$$

Chapter 2

Overview of the current experimental status

The experimental methodologies employed to measure the A_Γ parameter are briefly outlined in this chapter, along with its experimental status. The two techniques that are currently used to infer the D^0 flavour at production and the main experimental strategies to measure A_Γ are described, as well as the role of the Cabibbo-favoured $D^0 \to K^-\pi^+$ decay that is used to validate the measurement. A review of the past measurements of the A_Γ parameter is presented, with a particular focus on the last measurement performed by the LHCb experiment, which currently dominates the world average. As it represents the starting point of this thesis, its main challenges and its dominant systematic uncertainties are outlined.

2.1 Flavour tagging

A measurement of *CP* asymmetry requires the knowledge of the flavour at production ($t = 0$) of the decaying particles. Since the final state of both $D^0(t) \to f$ and $\overline{D}^0(t) \to f$ decays, where $f = K^+K^-$ or $f = \pi^+\pi^-$, is the same, the flavour of the D meson cannot be inferred from the observation of its decay products and must be distinguished analysing its production mechanism. This is usually achieved by analysing only the D^0 and $\overline{D}^0$ mesons that are produced in the two following decays:

1. $D^{*+} \to D^0\pi^+$ and $D^{*-} \to \overline{D}^0\pi^-$;
2. $\overline{B} \to D^0\mu^-\overline{\nu}_\mu X$ and $B \to \overline{D}^0\mu^+\nu_\mu X$, where $\overline{B}$ (B) stands for a generic hadron containing one b ($\overline{b}$) quark and X for all the additional particles that might be produced in the decay.

In the first case, the flavour-conserving strong interaction decay allows inferring the flavour of the D meson from the sign of the charge of the pion. In the second case, the flavour is inferred from the sign of the charge of the muon, which is the same of the charge of the W boson that mediates the tree-level transition between the $\overline{b}$ (b) and the c ($\overline{c}$) quark.

To date, most of the measurements of A_Γ have been performed using the first technique, as the production cross section of $c\overline{c}$ pairs is much larger than that of $b\overline{b}$ at the hadron colliders, whereas at the B-factories they are comparable, but the first decay chain is anyway favoured as its branching fraction is larger than that of the second decay chain by a factor of ten.[1]

[1] $\mathcal{B}(D^{*+} \to D^0\pi^+) = (67.7 \pm 0.5)\%$, whereas $\mathcal{B}(\overline{B} \to D^0\mu^-\overline{\nu}_\mu X) = (6.83 \pm 0.35)\%$. The last, inclusive branching fraction is averaged over the typical mixture of b-hadrons that is produced at the high energy hadron colliders [10].

2.2 Experimental strategies for the A_Γ measurement

Once the D^0 flavour has been determined according to one of the methods described in the previous section, there are two main approaches that have been historically used to extract the value of A_Γ from the information on the time-dependent asymmetry between the D^0 and $\overline{D}^0$ decay rates. They are described in the two following subsections, trying to highlight the main differences between them.

2.2.1 Approach based on the measurement of the effective lifetimes

The first method to measure the A_Γ parameter follows directly by its definition, Eq. (1.15):

$$A_\Gamma \equiv \frac{\hat{\Gamma}(D^0 \to f) - \hat{\Gamma}(\overline{D}^0 \to f)}{\hat{\Gamma}(D^0 \to f) + \hat{\Gamma}(\overline{D}^0 \to f)} = \frac{\hat{\tau}(\overline{D}^0 \to f) - \hat{\tau}(D^0 \to f)}{\hat{\tau}(\overline{D}^0 \to f) + \hat{\tau}(D^0 \to f)},$$

where $\hat{\tau} \equiv \frac{1}{\hat{\Gamma}}$ is the effective lifetime that is measured when modelling the decay time distribution with a simple exponential function. This approach, that requires a precise measurement of both the D^0 and the $\overline{D}^0$ effective lifetimes, was the first to be used at the B-factories, where they could be extracted with relative ease, since in this kind of experiments the D decays are characterised by very low background and can thus be selected without affecting significantly their decay time distribution. On the contrary, problems arise when trying to measure lifetimes in experiments that are installed at hadron colliders. In fact, these experiments have to request some requirements on decay time-related quantities—for example, on the flight distance of the D^0 meson before it decays—, in order to select a pure sample of $D^0 \to f$ decays from the overwhelming background of particles produced in the primary collision vertex between the two initial hadrons. Consequently, the measured distribution of the decay time is not exponential any longer, but is multiplied by a complex acceptance function which in general strongly depends on the decay time and is typically suppressed for low ones. This implies that measuring lifetimes at hadron colliders requires knowing the acceptance function with a high degree of precision.

Traditionally, this was achieved *via* precise Monte Carlo simulations; however, this approach does not appear to be feasible any longer in order to reach the level of precision which currently characterises the A_Γ measurement, $\sigma(A_\Gamma) \approx 3 \cdot 10^{-4}$, and data-driven methods must be developed. At the LHCb experiment, this was done through the so called *swimming* procedure, described in detail in Ref. [27, 28], which has been employed to perform a measurement of A_Γ with the data collected during 2011 [29]. However, the procedure is very CPU-consuming and it is possible that, as the data sample collected by the LHCb experiment increases, it will become unsustainable, given the predicted computing constraints, within the next few years. Therefore, it is fundamental to develop alternative approaches to perform the measurement of A_Γ in an easier, less CPU-consuming way.

2.2.2 Approach based on the measurement of the decay rate asymmetry $A_{CP}(t)$

The second approach to measure A_Γ is based on the relation that holds between this parameter and the CP asymmetry of decay rates in the limit of small CP violation (CPV) in the decay, Eq. (1.16):

$$A_{CP}(t) = \frac{\Gamma(D^0(t) \to f) - \Gamma(\overline{D}^0(t) \to f)}{\Gamma(D^0(t) \to f) + \Gamma(\overline{D}^0(t) \to f)} \approx A_{CP}^{\mathrm{dir}} - A_\Gamma \cdot \frac{t}{\tau_{D^0}}$$

where $\Gamma(D^0(t) \to f)$ is the decay rate into final state f and at time t of a particle that was created at $t = 0$ in its flavour eigenstate D^0. If $A_{CP}(t)$ is measured, A_Γ can be easily extracted with a linear fit to it, as the opposite of the slope.

However, at real experiments we do not measure directly the asymmetry between decay rates, but rather a raw asymmetry between the number of reconstructed D^0 and $\overline{D}^0$ mesons

$$A_{\text{raw}}(t) \approx \frac{\mathrm{d}N(t, D^0_{\text{rec}}) - \mathrm{d}N(t, \overline{D}^0_{\text{rec}})}{\mathrm{d}N(t, D^0_{\text{rec}}) + \mathrm{d}N(t, \overline{D}^0_{\text{rec}})},$$

where $\mathrm{d}N(t, D^0_{\text{rec}})$ is the number of $D^0(t) \to f$ decays reconstructed in the interval of proper decay time $[t, t+\mathrm{d}t]$. This quantity is insensitive to charge-independent acceptance and efficiency effects, as they cancel in the ratio. However, even if the final state $f = K^+K^-$, $\pi^+\pi^-$ is charge symmetric and is not expected to be affected by acceptance or detection asymmetries between D^0 and $\overline{D}^0$ decays, both flavour identification techniques described in Sect. 2.1 require the detection of an additional charged particle whose sign is opposite for D^0 and $\overline{D}^0$ events, and can easily introduce both acceptance and efficiency asymmetries.[2] Furthermore, the number of D^0 and $\overline{D}^0$ that are produced at the pp colliders is not the same, since the initial state of the collision is not *CP*-symmetric. As a result, the measured asymmetry between the number or reconstructed decays of D^0 and $\overline{D}^0$ mesons can be shown to contain two additional terms with respect to $A_{CP}(t)$:[3]

$$A_{\text{raw}}(t) \approx A_{CP}^{\text{dir}} - A_\Gamma \cdot \frac{t}{\tau_{D^0}} + A_{\text{D}}^{\text{flav.id}}(t) + A_{\text{P}}(t) \tag{2.1}$$

where $A_{\text{D}}^{\text{flav.id}}(t)$ denotes the detection asymmetry due to the flavour identification technique, enclosing both the acceptance and the efficiency asymmetries, $A_{\text{P}}(t)$ denotes the production asymmetry, and third order terms in $A_{CP}(t)$, $A_{\text{D}}^{\text{flav.id}}(t)$ and $A_{\text{P}}(t)$ are neglected. Both the detection and the production asymmetries depend only on the trajectories and on the momenta of the particles; therefore, they should not display any direct dependence on the D^0 decay time. If that were the case, they would not affect the measurement of A_Γ either, as this is related only to time-dependent variations of the asymmetry. However, slight time dependences of $A_{\text{D}}^{\text{flav.id}}(t)$ and $A_{\text{P}}(t)$ have been shown to arise owing to the correlations between the D^0 decay time and the momentum of the charged particle used to infer the D^0 flavour that are typically introduced by the selection requirements of the experiment. At the unprecedented statistical precision that has been achieved in the last measurement of A_Γ performed by the LHCb experiment [4], they can bias the value of A_Γ by a value whose size can be as large as five times the statistical uncertainty. As a consequence, they cannot be neglected and a dedicated procedure, described in Chap. 5, must be adopted to eliminate these artificial detector-induced, time-dependent charge asymmetries.

In conclusion, with respect to the determination of A_Γ performed through the measurement of the effective lifetimes, the method based on the measurement of the time-dependent decay asymmetry $A_{CP}(t)$ has the advantage that it does not require any knowledge of the acceptance of the experiment, but only to control the detection asymmetries between D^0 and $\overline{D}^0$ decays, as a function of the decay time. Therefore, it is the most suitable for the experiments installed at hadron colliders.

2.3 Control channel: $D^0 \to K^-\pi^+$ decays

At the level of precision that was achieved in the last measurements of A_Γ, $\mathcal{O}(10^{-4})$, it is essential to validate the analysis procedure on a parallel, well understood and more abundant control sample, in order to ensure its robustness and reliability and to assess the entity of any systematic

[2] For example, particles of opposite charge are deflected in opposite directions by magnetic fields, and if the detector is not perfectly symmetric and aligned with the magnetic field, acceptance asymmetries occur. Additionally, particles of opposite charge typically interact differently with matter, resulting into different detection efficiencies.

[3] See Appendix B of Ref. [30] for an explicit derivation of this result.

uncertainties related to the approximations that are intrinsic to the analysis and to the correction procedure that is used to mitigate the time-dependent production and detection contributions to the asymmetry of Eq. (2.1). The two-body decays of the D^0 into final states made up of two charged kaons or pions are an excellent experimental system from this point of view. In fact, four different decay channels of this type exist, with nearly the same kinematic characteristics, but completely different dynamical properties:

- the Cabibbo-favoured decay $D^0 \to K^-\pi^+$, with branching fraction $(38.9 \pm 0.4) \cdot 10^{-3}$, which is an excellent control channel where no *CPV* is expected to be detectable within the current experimental sensitivity;
- the singly Cabibbo-suppressed decay $D^0 \to K^+K^-$, with branching fraction $(3.97 \pm 0.07) \cdot 10^{-3}$, which is used to measure A_Γ;
- the singly Cabibbo-suppressed decay $D^0 \to \pi^+\pi^-$, with branching fraction $(1.41 \pm 0.03) \cdot 10^{-3}$, which is used to measure A_Γ, even if with lower precision;
- the doubly Cabibbo-suppressed decay $D^0 \to K^+\pi^-$, with branching fraction $(0.139 \pm 0.003) \cdot 10^{-3}$, which is of little or no use for the measurement of A_Γ owing to its highly suppressed branching fraction, but is fundamental in the measurement of the D^0 mixing [15–18].[4]

As in the case of the singly Cabibbo-suppressed decays, the time-dependent asymmetry of the $D^0 \to K^-\pi^+$ decays can be written as

$$A_{CP}^{K\pi}(t) = A_{CP}^{K\pi,\,\mathrm{dir}} + A_{CP}^{K\pi,\,\mathrm{ind}} \cdot \frac{t}{\tau(D^0)}.$$

However, both $A_{CP}^{K\pi,\,\mathrm{dir}}$ and $A_{CP}^{K\pi,\,\mathrm{ind}}$ are expected to be negligible within the current experimental sensitivity (in particular, $A_{CP}^{K\pi,\,\mathrm{ind}}$ can be estimated to be $\leq \mathcal{O}(10^{-5})$, see Appendix A of Ref. [30]). The smallness of the direct *CPV* is ascribable to the fact that the tree level decay $D^0 \to K^-\pi^+$, as opposed to $D^0 \to K^+K^-$ and $D^0 \to \pi^+\pi^-$, is not Cabibbo-suppressed; therefore, loop diagrams responsible for *CPV* are expected to contribute lesser in the first than in the last two decays. On the other side, indirect *CPV* is suppressed because the interference between the $D^0 \to K^-\pi^+$ and the $D^0 \to \overline{D}{}^0 \to K^-\pi^+$ decays, where in the last case the D^0 oscillates in a $\overline{D}{}^0$ owing to mixing before decaying, is largely suppressed by the fact that $D^0 \to K^-\pi^+$ is a Cabibbo-favoured decay, whereas $\overline{D}{}^0 \to K^-\pi^+$ is a far less frequent doubly Cabibbo-suppressed one.[5]

As a consequence, the asymmetry between $D^0 \to K^-\pi^+$ and $\overline{D}{}^0 \to K^+\pi^-$ decays can be written as

$$A_{\mathrm{raw}}^{K\pi}(t) \approx A_{\mathrm{D}}^{\mathrm{flav.id}}(t) + A_{\mathrm{D}}^{K\pi}(t) + A_{\mathrm{P}}(t)$$

where no dynamical *CP* asymmetries are present, but an additional detection asymmetry term $A_{\mathrm{D}}^{K\pi}(t)$ appears with respect to Eq. (2.1), since the final state of $D^0 \to K^-\pi^+$ decay is no *CP*-symmetric any longer, and kaons of opposite charge possess different interaction cross sections with matter. However, this quantity is expected to be much lower than $A_{\mathrm{D}}^{\mathrm{flav.id}}(t)$, since the kaons are characterised by detection asymmetries that are much lower than those of the muons and pions that are used to infer the D^0 flavour. Moreover, it is partially corrected by the correction procedure described in Chap. 5, and can therefore be safely neglected. From the last equation, it is then clear that the $D^0 \to K^-\pi^+$ decay represents an excellent channel to check if the analysis procedure is accurate. In fact, if the raw asymmetry in $D^0 \to K^-\pi^+$ decays is modelled as

$$A_{\mathrm{raw}}^{K\pi} = A_0^{K\pi} - A_\Gamma^{K\pi} \cdot \frac{t}{\tau(D^0)},$$

[4] All branching fractions are taken from Ref. [10].

[5] On the contrary, $D^0 \to f$ and $\overline{D}{}^0 \to f$ decays are equally suppressed.

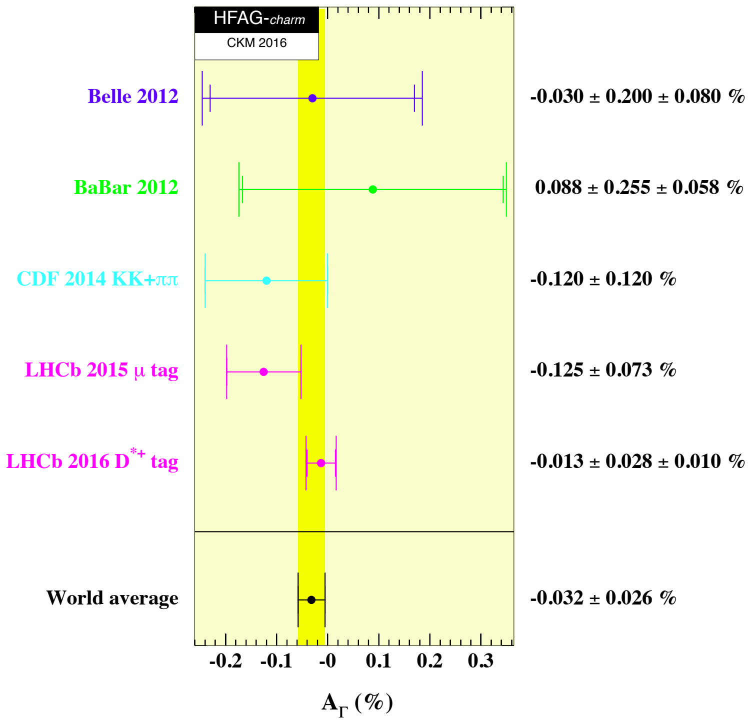

Figure 2.1: Current experimental status of the A_Γ parameter (figure taken from Ref. [3]); universality is assumed. Measurements references and relative integrated luminosity, from top to bottom: Belle 2012 ($976\,\mathrm{fb}^{-1}$) [31], BaBar 2012 ($468\,\mathrm{fb}^{-1}$) [32], CDF 2014 ($9.7\,\mathrm{fb}^{-1}$) [33], LHCb 2015 μ tag ($3\,\mathrm{fb}^{-1}$) [34], LHCb 2016 D^{*+} tag ($3\,\mathrm{fb}^{-1}$) [4].

with a formula that is equivalent to that used to measure the real A_Γ, the measurement of a value of $A_\Gamma^{K\pi}$ different from zero would unequivocally indicate that the time dependence of $A_{\mathrm{D}}^{\mathrm{flav.id}}(t)$ or $A_{\mathrm{P}}(t)$ is not appropriately corrected by the measurement procedure. Finally, the abundance of such decays and their kinematic similarity to $D^0 \to K^+K^-$ and $D^0 \to \pi^+\pi^-$ decay modes can be employed in order to assess some systematic uncertainties on the measurement of A_Γ with a higher level of precision than would be possible using only the $D^0 \to K^+K^-$ and $D^0 \to \pi^+\pi^-$ samples.

2.4 Current experimental status

The most precise measurements of A_Γ to date and their references are summarised in Fig. 2.1, where universality is assumed (see Sect. 1.5.5); their average is compatible with the hypothesis of no *CPV* ($A_\Gamma = 0$) within $3 \cdot 10^{-4}$. The first two measurements were performed at e^+e^- colliders by the Belle and BaBar collaborations. They both identify the D^0 flavour with the $D^{*+} \to D^0\pi^+$ decay and they extract the D^0 and $\overline{D}^0$ effective lifetimes through a maximum likelihood fit of their decay time distributions, simultaneously for $D^0 \to K^+K^-$ and $D^0 \to \pi^+\pi^-$ decays. Then, A_Γ is extracted as the asymmetry between the D^0 and $\overline{D}^0$ effective lifetimes, see Sect. 2.2.1. In the last years, these measurements were surpassed by those performed at hadronic colliders, that benefit from a much larger $c\bar{c}$ production cross section.

All the measurements performed by the CDF and LHCb experiments that are reported in Fig. 2.1 were performed extracting A_Γ from a linear fit of the asymmetry $A_{CP}(t)$ between D^0 and $\overline{D}^0$ decay rates (see Sect. 2.2.2), calculated in bins of decay time, separately for $D^0 \to K^+K^-$ and $D^0 \to \pi^+\pi^-$ decays. The better precision achieved by the LHCb experiment with respect to CDF, although the second experiment recorded a factor of three higher integrated luminosity, stems from the higher $c\bar{c}$ cross section at the LHC with respect to the Tevatron collider and by the fact that the LHCb trigger was specifically designed to collect a pure sample of c and b-hadron decays, and can afford a much higher data writing rate than that of CDF.

Both the measurements of the LHCb experiment were performed with the full data sample of Run 1 ($1\,\text{fb}^{-1}$ of integrated luminosity at a centre-of-mass energy of $7\,\text{TeV}$ and $2\,\text{fb}^{-1}$ at $8\,\text{TeV}$), but with two independent samples; in the first one the flavour of the D^0 is identified with B semileptonic decays, in the second one with D^{*+} strong decays. The second result is more precise by a factor of nearly 2 owing to the larger $c\bar{c}$ production cross section with respect to the $b\bar{b}$ one for the pp collisions at the LHC, and currently dominates the world average of A_Γ:

$$\begin{aligned} A_\Gamma(D^0 \to K^+K^-) &= (-3.0 \pm 3.2 \pm 1.0) \cdot 10^{-4}, \\ A_\Gamma(D^0 \to \pi^+\pi^-) &= (+4.6 \pm 0.58 \pm 1.2) \cdot 10^{-4}. \end{aligned}$$

At this unprecedented degree of precision, the detector-induced time-dependent terms of Eq. (2.1) cannot be neglected any longer, and a new experimental technique was introduced to correct them, as explained in Chap. 5 and in Ref. [30].

2.5 Systematic uncertainties

As the last measurement of LHCb [4] dominates the world average of A_Γ and it constitutes the starting point for this thesis, the discussion of the systematic uncertainties is narrowed to that measurement (in any case, most of them are common to the measurements of the other experiments).

At the experiments installed at hadron colliders, whenever the D^0 flavour is identified using the $D^{*+} \to D^0\pi^+$ decay, the decay time of the D^0 is usually measured supposing that the D^{*+} (and hence the D^0) was produced in the primary vertex of collision between the two particle beams. In fact, most D^{*+} are actually produced there (primary decays), and the resolution of the measurement of the primary vertex is typically much better than that of the $D^0\pi^+$ reconstructed vertex, allowing a sizeable improvement of the decay time resolution. However, a smaller fraction of D^{*+} originates from the decay of b-hadrons, that we can generically indicate with B (secondary decays).[6] For these events, the measurement of the decay time is biased towards higher times, as the flight distance of B is not negligible with respect to that of the D^0 ($c\tau(D^0) = 123\,\mu\text{m}$, whereas $c\tau(B) \approx 500\,\mu\text{m}$). The bias coming from the presence of a residual fraction of secondary decays that are not removed from the data sample affects the measurement of A_Γ and currently constitutes its dominant systematic uncertainty, amounting to $0.8 \cdot 10^{-4}$ and $1.2 \cdot 10^{-4}$ for $D^0 \to K^+K^-$ and $D^0 \to \pi^+\pi^-$ decays, respectively. In this thesis, the problem of secondary decays is addressed in Chap. 6.[7]

The second largest systematic uncertainty is due to the background from partially reconstructed and misidentified D^0 decays, such as $D^0 \to K^-\pi^+\pi^0$, $D^+ \to K^-\pi^+\pi^+$ and $D_s^+ \to K^+K^-\pi^+$. If one of the particles produced in the decay of the meson is not detected, but another one is wrongly assigned a kaon instead of a pion identity, the loss in D^0 invariant mass can be compensated by its larger mass. The relative contamination to the signal, corresponding to about 0.5% for the $D^0 \to K^+K^-$ decay mode, is accounted for with a systematic uncertainty of $0.5 \cdot 10^{-4}$. On the contrary, it is completely negligible in the $D^0 \to \pi^+\pi^-$ decays, as in this case the loss in invariant mass cannot be compensated.

[6] The typical inclusive branching fraction of b-hadrons into a final state involving a D^{*+} at hadron colliders is $\mathcal{B}(\overline{B} \to D^{*+}X) \approx 17\%$ [10].

[7] On the contrary, in the measurements that adopt the semileptonic decays of the B to identify the D^0 flavour, the decay time of the D^0 is measured from the decay vertex of the B hadron. Therefore, it is independent of the decay time of the B hadron, and no bias is introduced.

Other minor systematic uncertainties, coming from the approximated nature of the procedure that is employed to remove the detector-induced time-dependent charge asymmetries, or due to the residual presence of other backgrounds, were all estimated to be negligible within $0.2 \cdot 10^{-4}$, and have a marginal impact on the total current value of the systematic uncertainty.

2.6 Purpose of the thesis and future perspectives

As shown in Sect. 2.4, in the last few years the LHCb experiment has provided the most precise measurements of A_Γ to date using the full data sample collected during the LHC Run 1 (2011-2012, $3\,\text{fb}^{-1}$ of integrated luminosity at the centre-of-mass energy of 7–8 TeV), with a statistical uncertainty of $2.8 \cdot 10^{-4}$ and a systematic one of $1.0 \cdot 10^{-4}$. During the LHC Run 2 (2015–2018), the LHCb experiment is expected to collect additional $5\,\text{fb}^{-1}$ of integrated luminosity at the increased centre-of-mass energy of 13 TeV. The number of collected events will increase more than linearly with the integrated luminosity for several reasons: the increment of the centre-of-mass energy has caused the charm production cross section to grow by a factor of 1.8 [5], the LHCb trigger system has undergone a substantial upgrade [6, 7] moving towards the configuration that will be adopted in the future high luminosity runs, the reduction of the event size and the parallel increase of the rate at which data are written to disk caused the data-taking rate to increase by a further factor of 2. On a slightly longer timescale, the LHCb experiment is going to record other $40\,\text{fb}^{-1}$ of integrated luminosity by the end of the LHC Run 3 and Run 4 (2021–2030), the so called Phase-I LHC-Upgrade, where the instantaneous luminosity will move from the current $4 \cdot 10^{32}\,\text{cm}^{-2}\,\text{s}^{-1}$ to $2 \cdot 10^{33}\,\text{cm}^{-2}\,\text{s}^{-1}$.[8] Finally, an expression of interest has been recently submitted to the LHC Experiments Committee (LHCC) to build a Phase-II Upgrade of LHCb able to take advantage of the high luminosity that will be delivered by the HL-LHC from 2031, operating at an instantaneous luminosity of $2 \cdot 10^{34}\,\text{cm}^{-2}\,\text{s}^{-1}$ and recording more than $300\,\text{fb}^{-1}$ of data [35]. In this context, the statistical uncertainty on the measurement of A_Γ parameter is expected to decrease very quickly, likely dropping below the level of $1 \cdot 10^{-4}$ already by the end of Run 2, and approaching the unprecedented precision of 10^{-5} during Run 3 and Run 4.

The work described in this thesis has therefore a dual purpose. Firstly, it aims at improving the statistical uncertainty on A_Γ extending its measurement to the total currently available LHCb data sample, including the new data collected during the LHC Run 2 (2015–2016, $1.7\,\text{fb}^{-1}$). Secondly, it aims at a significant reduction of systematic uncertainties, paving the way to the measurements with still higher precision that are foreseen in the next few years, whose statistical uncertainty will quickly become comparable or even lesser than the current systematic one. Both purposes are particularly relevant at present since the currently achieved range of precision ($3 \cdot 10^{-4}$) is very close to the lower bound of the interval enclosing most of the SM predictions that have been made for the A_Γ value so far, that are within the range 10^{-4}–10^{-3} (see for example [1, 2]). Therefore, any improvement of the experimental sensitivity in a short time scale may provide a valuable contribution to our knowledge of charm sector dynamics, either in the presence of first hints of *CPV* or in the case of results fully compatible with conservation of the *CP* symmetry.

As the Run 2 data-taking conditions have considerably changed with respect to those of Run 1, a careful analysis of the impact of the new selection criteria on the A_Γ measurement is performed. As anticipated in Sect. 2.2.2, selection requirements on momenta and lifetime-related quantities introduce correlations between the D^0 decay time and other kinematic variables that affect the detection efficiency, generating biases to the measurement of A_Γ of order 10^{-3}, well above the statistical uncertainty. These effects must accurately accounted for in order to achieve

[8] Meanwhile, the Belle II experiment will come into operation by the middle of 2018 and is expected to collect $50\,\text{ab}^{-1}$ of integrated luminosity by the end of 2025, to be compared with the value of its previous measurement, $976\,\text{fb}^{-1}$ [31].

the desired precision on the measurement. With this aim, in the Run 1 measurement a fully data-driven correction [4] was developed, allowing to keep under control systematic uncertainties below the level of 10^{-4}. However, it is not automatically guaranteed that such a procedure will prove to be successful at the new, improved level of precision and with the new sample of data collected in very different conditions, as described in Chap. 4. Additional and more detailed studies are therefore required in order evaluate the various systematic factors that might limit the precision of the future measurements at LHCb. Chapter 5 is then devoted to pinpoint the origin of the detector-induced, time-dependent charge asymmetries, highlighting both the origin of the correlations between the D^0 decay time and the momentum of the pion coming from the decay of the D^{*+}, and to accurately assessing the impact on the A_Γ measurement of the requirements of the various new trigger lines that were introduced in Run 2.

In preparation for future measurements at much higher precision, particular attention has been devoted to the effort of reducing the size of the dominant systematic uncertainty of the previous execution of this measurement with Run 1 data sample. The residual contamination of few per cents of secondary decays was not subtracted in the past, and a systematic uncertainty of $1.0 \cdot 10^{-4}$ was assessed to fully cover the size of the relative bias of the measurement. Chapter 6 describes a novel approach specifically developed to subtract the contribution of secondary decays from the final data sample, and to drastically reduce, by about a factor of 5, the size of the associated systematic uncertainty, thus reaching an unprecedented level of about $0.2 \cdot 10^{-4}$.

The preliminary, blinded measurement of A_Γ in $D^0 \to K^+K^-$ and $D^0 \to \pi^+\pi^-$ decays with pp collision data collected by LHCb in Run 2 during 2015 and 2016, at a centre-of-mass energy of 13 TeV, corresponding to an integrated luminosity of $1.7\,\mathrm{fb}^{-1}$, is presented in Chap. 7.

Chapter 3

The LHCb experiment at the LHC

This chapter briefly describes the Large Hadron Collider and the LHCb experiment, with a particular focus on the aspects that are more relevant to the measurement of the A_Γ parameter, namely the tracking and the trigger system. Further information on the LHC and the LHCb experiment can be found in the references cited throughout the chapter.

3.1 LHC

The Large Hadron Collider (LHC) is a superconducting circular hadron accelerator operating at the laboratories of CERN (*Conseil Européen pour la Recherche Nucléaire*) [36]; it is hosted in the 27 km tunnel that previously housed the Large Electron Positron collider (LEP), sited about 100 m underground across the French-Swiss border near Geneva.

Two proton beams, circulating in opposite directions along the ring, are bent by superconducting NbTi dipole magnets and collide in four interaction regions, corresponding to the four main experiments sited at the LHC: ALICE, ATLAS, CMS and LHCb. ATLAS and CMS are general purpose experiments, whereas ALICE and LHCb are specifically designed to study heavy-ion[1] and heavy-flavour physics, respectively. The beams are not continuous; on the contrary, the protons are organised in *bunches* of about 10^{11} protons each. The time distance between two consecutive bunches is a multiple of 25 ns, corresponding to a nominal bunch-crossing rate of 40 MHz. However, bigger gaps are present between some bunches, in order to allow the injection and the dumping of the beams; therefore, the effective crossing rate is about 30 MHz.

The event rate of any process generated in the LHC pp collisions is given by:[2]

$$\frac{\mathrm{d}N}{\mathrm{d}t} = \mathcal{L} \cdot \sigma(\sqrt{s}),$$

where $\mathcal{L}$ is the instantaneous luminosity of the collider and $\sigma(\sqrt{s})$ is the cross section of the process at the centre-of-mass energy $\sqrt{s}$. The design specifications of the LHC targeted operations at the instantaneous luminosity of $10^{34}\,\mathrm{cm}^{-2}\,\mathrm{s}^{-1}$. However, the LHCb experiment is not limited by the number of $c\bar{c}$ and $b\bar{b}$ produced in the pp interactions but by the trigger and reconstruction efficiencies and by the amount of data that can be saved to be analysed. Therefore, it decided to limit the luminosity to the level of $2\text{–}4{\cdot}10^{32}\,\mathrm{cm}^{-2}\,\mathrm{s}^{-1}$ by shifting the colliding beams in the plane transverse to their direction, thus reducing their overlap at the collision region. Thanks to this choice, the number of pp interactions per bunch crossing is kept below 2, limiting the detector occupancy and facilitating the trigger selection and reconstruction.

The centre-of-mass energy of the pp collisions raised from 7 TeV (2010 and 2011) to 8 TeV (2012) and finally to 13 TeV (2015–2017). The LHCb operations are accordingly divided in Run 1

[1] The LHC can be used, in dedicated runs, also to collide ions of lead and/or other elements.

[2] An event is defined as the set of interactions and decays that follow a collision between two proton bunches.

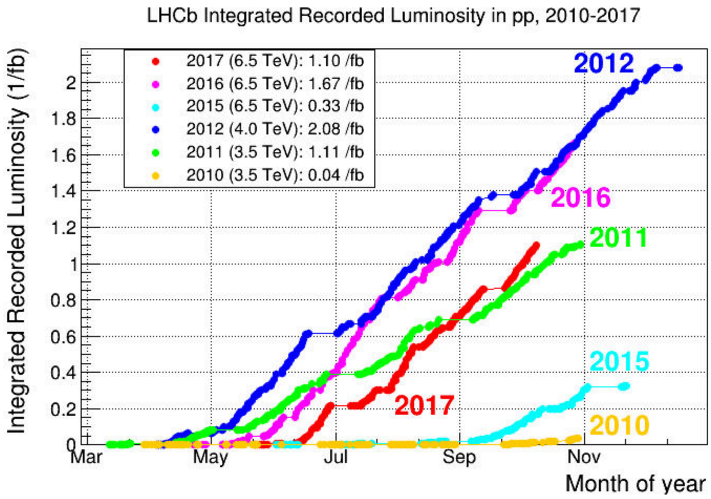

Figure 3.1: LHCb recorded integrated luminosity in pp interactions by year. The beam energy, corresponding to half of the centre-of-mass energy $\sqrt{s}$, is also reported.

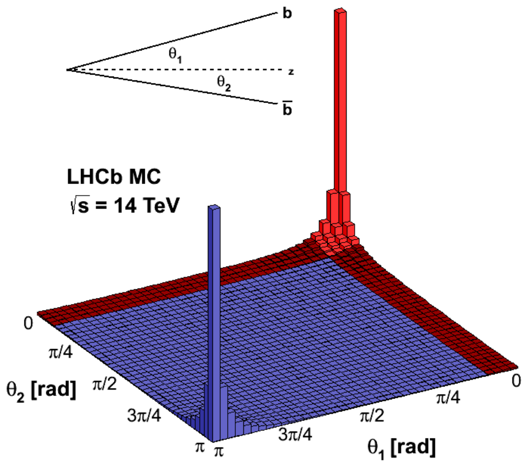

Figure 3.2: $b\bar{b}$ production cross section as a function of their polar angle with respect to the beam axis, in pp collisions simulated with Pythia [37]. The LHCb acceptance is displayed in red.

(2010–2012) and Run 2 (2015–2018). The integrated luminosity recorded over time by the LHCb experiment, together with the beam energy, are displayed in Fig. 3.1.

3.2 LHCb detector

The LHCb experiment is designed to measure the properties of b- and c-hadrons with unprecedented precision, possibly unveiling indirect evidence of phenomena of new physics beyond the standard model of particle physics in *CP* violation and rare decays of these particles.

In a high-energy pp collider, b quarks are mainly produced in $b\bar{b}$ pairs *via* the strong interaction of the partons of two colliding protons, their production cross section being peaked in a forward and a backward cones along the beam axis, as shown in Fig. 3.2. Therefore, the LHCb detector was designed as a single-arm spectrometer with a forward angular coverage from approximately 10 mrad to 300 (250) mrad in the horizontal (vertical) plane [38]. This choice enables the detector

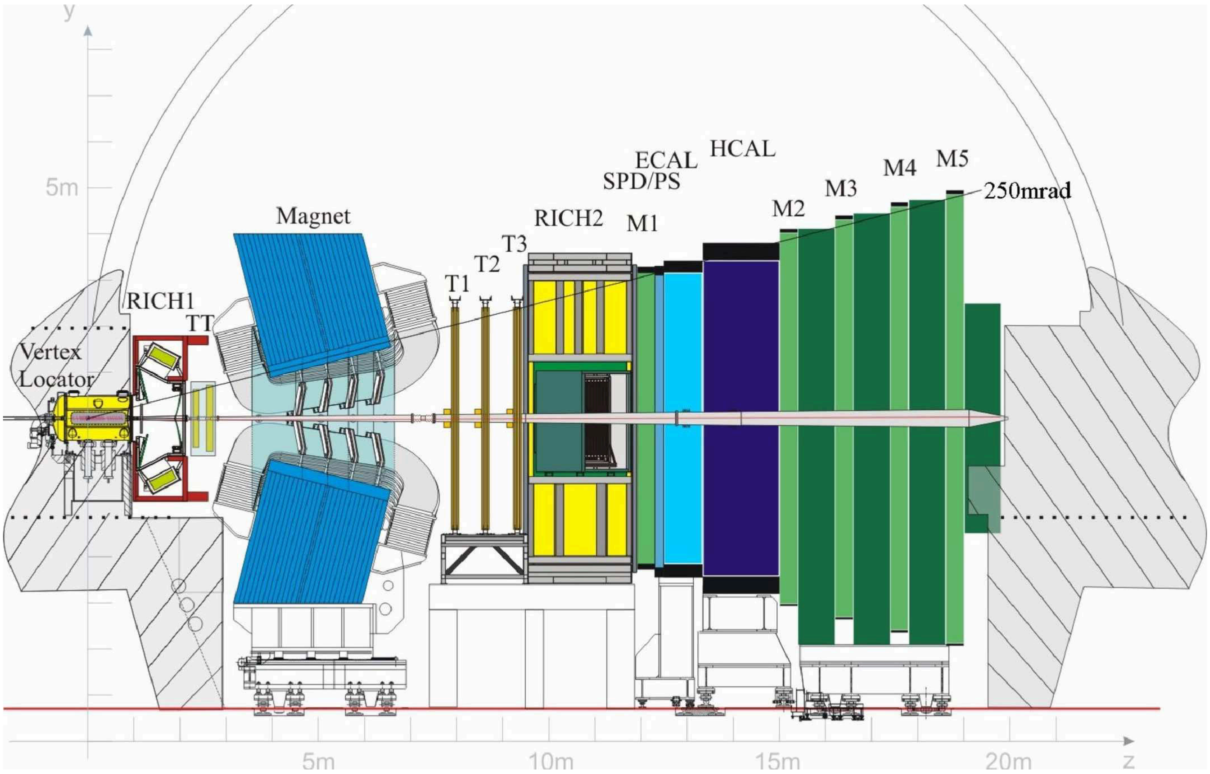

Figure 3.3: Side view of the LHCb spectrometer.

to collect about 27% of b quarks produced in the pp collisions, covering a relatively little angle, with benefits both in terms of costs and of ease of construction and access to the subdetectors, that are placed sequentially along the beam axis. In fact, most detector subsystem are assembled in two halves, which are mounted on rails and can be moved out separately in the horizontal x direction for assembly and maintenance, as well to provide access to the beam-pipe, whenever necessary. The pseudorapidity acceptance of LHCb, $1.8 < \eta < 4.9$, is furthermore complementary to that of the general purpose detectors like CMS and ATLAS ($|\eta| < 2.4$).[3]

The layout of the LHCb spectrometer is shown in Fig. 3.3; the right-handed coordinate system adopted is centred in the nominal pp interaction point, with the x axis pointing towards the centre of the LHC ring, the y axis pointing upwards and the z axis pointing along the beam. The main components of the spectrometer are, from left to right:

- **VELO** the vertex locator, a silicon-strip vertex detector surrounding the pp interaction region, aimed at measuring the position of the vertices of the pp interactions and the decay vertices of heavy flavoured hadrons with high precision;
- **RICH1** a ring imaging Čerenkov detector providing particle identification information (PID) for charged particles with momentum in range 1–60 GeV/c;
- **TT** the Tracker Turicensis, a large-area silicon-strip tracking detector placed just before the magnet;
- **magnet** a warm magnet producing a vertical field with bending power 4T m, allowing the measurement of the momentum of charged particles;

[3] The pseudorapidity is defined as $\eta = -\log[\tan(\theta/2)]$, where θ is the polar angle with respect to the beam axis.

- **T1, T2, T3** three tracking stations, made up of silicon strips in the central region and of straw drift tubes in the outer region, that are placed downstream of the magnet, used to measure the momentum of charged particles;
- **RICH2** a second ring imaging Čerenkov detector providing PID information for charged particles with momenta from 15 GeV/c up to and beyond 100 GeV/c;
- **ECAL** the electromagnetic calorimeter, essential to identify the electrons and the photons, to measure the energy of the last ones and to allow the hardware trigger to select electrons and photons candidates;
- **SPD/PS** the scintillating pad detector and the preshower detector, separated by a thin plate of lead, used to distinguish electrons from photons and electrons from hadrons, respectively;
- **HCAL** the hadronic calorimeter, used to identify and trigger the hadrons;
- **M1–5** the muon stations, composed by alternating layers of iron and multiwire proportional chambers, used to identify and trigger the muons.

Since the mass (and hence momentum) resolution of the spectrometer is essential to trigger on the decay of heavy flavoured hadrons, particular attention was paid to minimise the material budget up to the end of the tracking system, in order to minimise multiple scattering and other particle-matter interactions. On average, just before entering RICH2, a particle has crossed about 60% of a radiation length and 20% of an absorption length.

3.2.1 Tracking system

Magnet

A warm dipole magnet is placed between the TT and the T-stations, allowing for a measurement of the momentum of charged particles. The magnet is formed by two saddle-shaped coils that are slightly inclined in order to match the required detector angular acceptance (see left part of Fig. 3.4). The produced magnetic field is approximatively vertical, along the y axis, reaching a maximum intensity of about 1.1 T, for a total bending power of about 4 T m. The profile of the magnetic field is displayed in the right part of Fig. 3.4; most detectors lie outside the magnetic field, even if some residual field is present in the TT and, more importantly, in the T-stations. A precise map of the magnetic field is measured with Hall probes before the data-taking periods, to ensure a good momentum resolution for charged particles.

The presence of the vertical magnetic field makes the charged particles hit preferentially the right or the left side of the detectors, depending on the sign of their charge. This fact is especially evident for particles with low momenta: for example, a pion with $p_z = 5\,\mathrm{GeV}/c$ changes its direction, passing through the magnetic field, of about 250 mrad, a quantity comparable to the entire LHCb acceptance of 300 mrad. This fact introduces large detection asymmetries for particles with opposite charge. The asymmetries are partially corrected by reversing the polarity of the magnet (*MagUp* or *MagDown*) about every two weeks: if the data samples collected with opposite polarities have approximately equal size and if the detector operating conditions are stable enough, the detection charge asymmetries are expected to cancel.

Vertex locator

The vertex locator (VELO) is a silicon-strip vertex detector surrounding the pp interaction region. Its main purpose it to precisely measure tracks direction,[4] in order to reconstruct both

[4]Tracks are defined as the trajectories of charged particles.

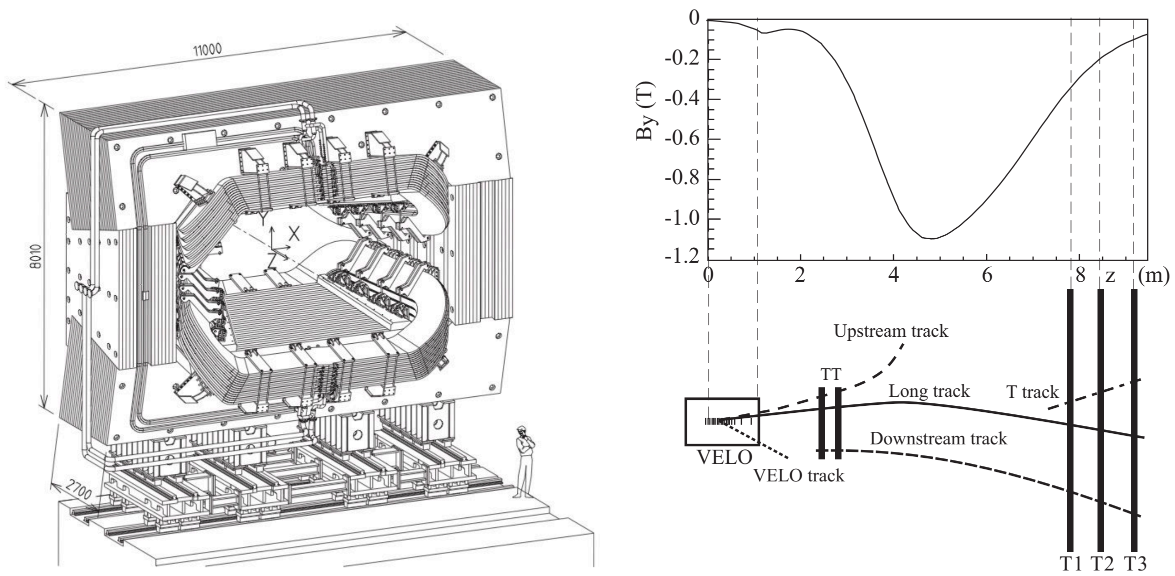

Figure 3.4: Left: perspective view of the LHCb dipole magnet (lengths in mm); the interaction point lies behind the magnet. Right: vertical magnetic field measured on the z axis, as a function of the z coordinate; the z location of the tracking detectors are shown, as well as the names given to the measured tracks, depending on the detectors from which they are detected; in this thesis we are only interested in *long tracks*, i.e. tracks that have been detected by all the three tracking subsystems. Figures taken from Ref. [38].

the primary vertices (PV) of the pp collisions and the displaced secondary vertices that are a distinctive feature of the decay of b- and c-hadrons, whose mean flight distance before decaying is $\mathcal{O}(\text{ cm})$.

The VELO consists of a series of 42 punched semicircular silicon modules arranged perpendicularly on the left and on the right of the beam direction, as shown in Fig. 3.5. The disposition of the modules is chosen such that every track within the LHCb acceptance intersects at least four of them. Each module is composed of two overlapping sensors, specialised to measure the r and ϕ coordinates (Fig. 3.6). In both cases, the sensitive area is 300 μm thick, starts at 8.2 mm radial distance from the beam and ends at 41.9 mm from it. The R-sensors measure the radial distance from the beam with semicircular-shaped strips, subdivided into four 45° regions to reduce the detector occupancy. The pitch at the innermost radius is 38 μm, increasing linearly with the radial distance up to 102 μm at the outer radius, ensuring that measurements along the track contribute to the precision on its impact parameter from the PV with roughly equal weights. The ϕ-sensor is subdivided in two regions, inner and outer, whose border is located at 17.25 mm from the centre. In the inner region, the strip pitch increases linearly from 38 to 78 μm, whereas in the outer region the pitch increases from 39 to 97 μm. At the innermost radius, the inner strips have an angle of approximately 20° to the radial direction, whereas the outer strips have an angle of approximately 10°. The modules are installed so that adjacent ϕ-sensors have the opposite skew with respect to each other; the resulting stereo view allows for a better discrimination of ghost hits from true ones, with respect to a configuration where all ϕ sensors are placed along the radial direction.

The minimum distance of the sensitive area of the VELO modules from the beam, 8.2 mm, is smaller than the aperture required by the LHC during the beams injection. Therefore, the VELO sensors are mounted on a remote-controllable positioning system that allows to retract them by 3 cm along the x direction whenever the beam is not stable, in order to avoid damaging the sensors (*VELO open* configuration, in contrast to the *VELO closed* standard configuration).

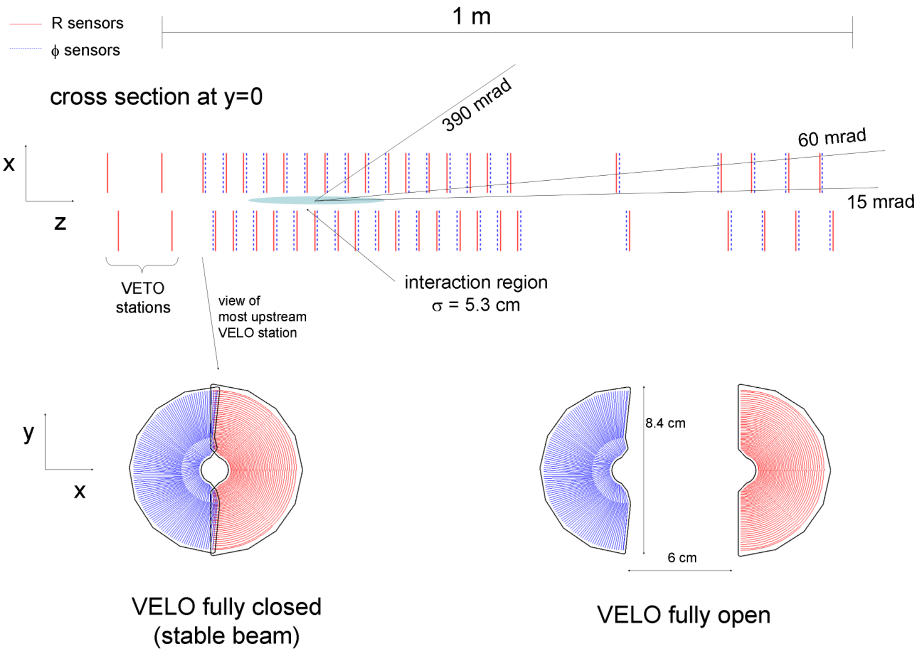

Figure 3.5: Cross section in the (x, z) plane of the VELO silicon sensors, at $y = 0$, with the detector in the closed position. The front face of the first modules is also illustrated in both the closed and open positions. Figure taken from Ref. [39].

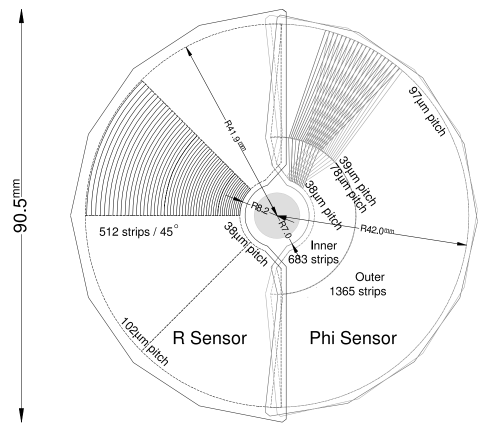

Figure 3.6: Geometrical scheme of the r and ϕ VELO sensors. For clarity, only a portion of the strips are illustrated; in the ϕ-sensor, the strips on two adjacent modules are indicated, to highlights the stereo angle. Figure taken from Ref. [39].

Each half of the VELO system is mounted inside a thin aluminium box, with the double function of maintaining the vacuum inside the detector and to shield the VELO from electromagnetic effects induced by the high frequency beam structure, hence the name of radiofrequency (RF) box.[5] The innermost surfaces of the two boxes are referenced as RF-foils and are made from 300 µm thick AlMg3 (an aluminium alloy with 3% magnesium). They present a highly corrugated shape to allow the two detector halves to overlap in the *VELO closed* configuration (see Fig. 3.7).

[5] Aluminium was chosen because of its relatively small radiation length, in order to minimise the interaction of charged particles with matter before crossing the detector.

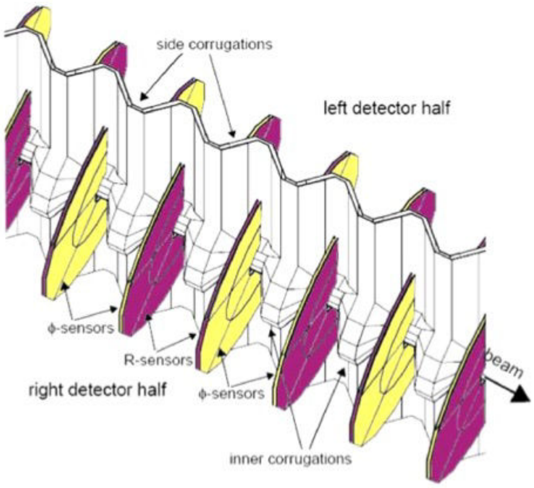

Figure 3.7: Inner view of the RF-boxes, with the detector halves in the fully closed position; the edges of the boxes are cut away to show the overlap between the sensors of the two halves. R- and ϕ-sensors are coloured in yellow and purple, respectively. Figure taken from Ref. [39].

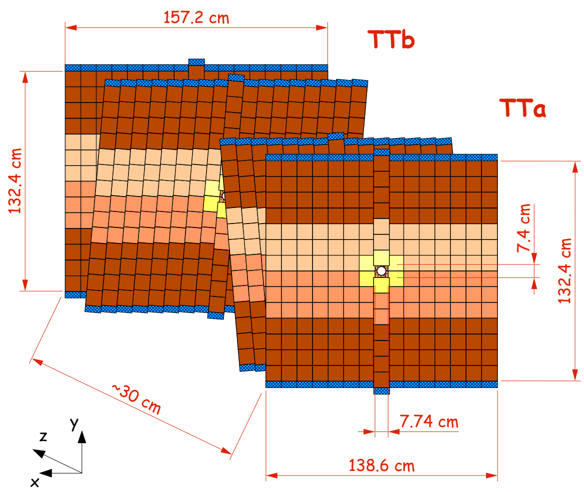

Figure 3.8: Scheme of the TT detector; different readout sectors are indicated by different shadings. Figure taken from Ref. [40].

Tracker turicensis

The tracker turicensis (TT) is a silicon microstrip detector placed immediately upstream of the dipole magnet, with the double purpose of reconstructing the trajectory of low-momentum particles that are deflected out of the LHCb acceptance by the magnet, and to reconstruct the trajectory upstream of the magnet of long-lived particles that are likely to decay outside the VELO region, such as the K^0_S and the Λ.

It covers a rectangular area about 150 cm wide and 130 cm high, corresponding to the full LHCb angular acceptance, and consists of four planar layers organised in two pairs separated by about 30 cm along the LHC beam axis, as displayed in Fig. 3.8. The first and last layers

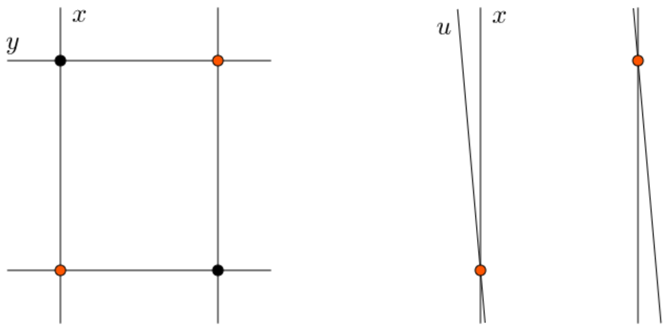

Figure 3.9: Strips activated by the passage of the same two particles in a $(x-y)$ and $(x-u)$ stations, respectively on the left and on the right. The particle hits are displayed in red; as it can be seen, the smaller angle between the x and u strips reduces the number of intersections between vertical and rotated strips, thus avoiding the reconstruction of the two black ghost hits that do not correspond to the passage of any particle in the $(x-y)$ detector.

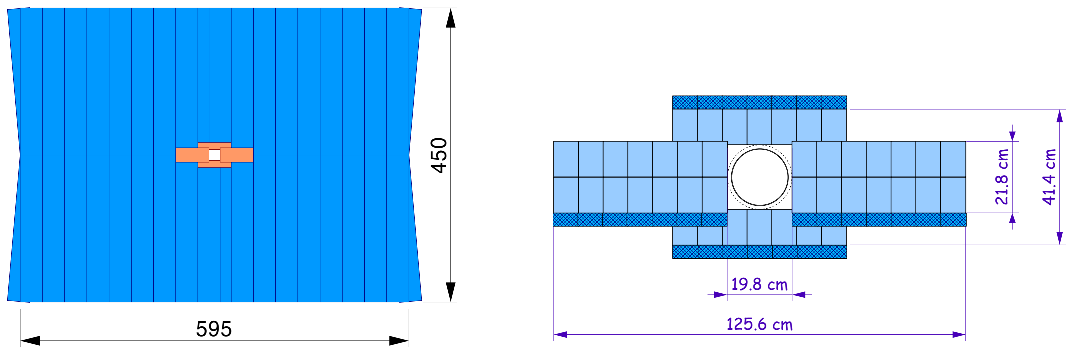

Figure 3.10: Left: front view of one of the T-stations (lengths in cm); the inner tracker is drawn in orange, the outer tracker in blue. Right: front view of a x plane of the inner tracker. Figure taken from Ref. [40].

are organised in vertical strips, measuring the x coordinate of the particles, whereas the second and third layer strips are rotated by $\pm 5°$ with respect to the vertical (u and v layers). The (x-u-v-x) arrangement allows to reduce the ambiguities and ghost hits that would arise by using a orthogonal arrangement, as displayed in Fig. 3.9. Each sensor module is a 500 µm thick, 9.64 cm wide and 9.44 cm long silicon sensor, carrying 512 readout strips with a strip pitch of 183 µm.

T-stations

The T-stations, T_1, T_2 and T_3, are three tracking stations placed immediately downstream of the dipole magnet, to measure the charged particles momentum. Each of them covers a area of approximatively $(6 \times 5)\,\mathrm{m}^2$, and is made up of four detection planes in a (x-u-v-x) arrangement, where the x planes are covered by vertical strips, whereas the u and v plane strips are tilted by $\pm 5°$, like for the TT. In order to hold costs down, only the area closer to the beam pipe is covered with silicon micro-strip detectors (*Inner Tracker*), whereas the larger part, corresponding to higher polar angles, is covered by straw-tube detectors (*Outer Tracker*), as shown in Fig. 3.10. The border between the inner and the outer tracker was determined by the requirement that the detector occupancies be lower than 10%, while keeping the single hit detection efficiency for every layer larger than 99%.

Inner tracker The Inner Tracker is a micro-strip silicon detector, whose modules use the same

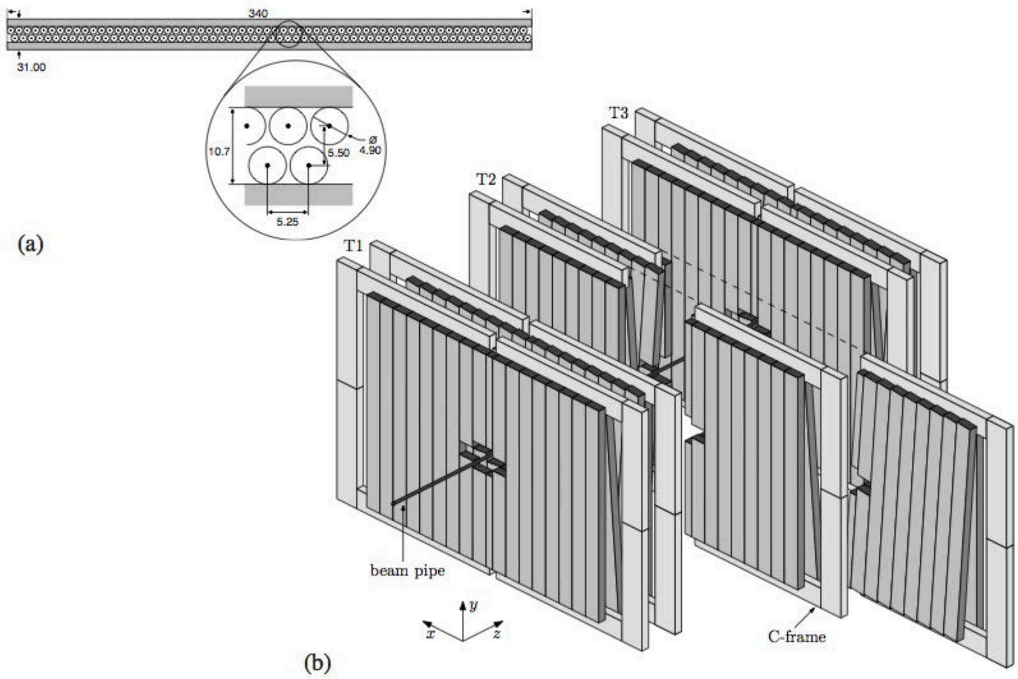

Figure 3.11: (a) Section of an OT detection plane. (b) Arrangement of OT straw-tubes modules in planes and stations; the second station is partially opened. Figure taken from Ref. [41].

technology and the same pitch of 198 µm employed by the TT, but with different width and length, (7.6×11) cm. All the four planes of each T-station are characterised by a cross shape, as displayed in the right part of Fig. 3.10, and are about 125 cm wide and 40 cm high.

Outer tracker The Outer Tracker (OT) is a gaseous ionisation detector consisting of straw-tubes operating as proportional counters. Each of the four planes that form a T-station is made up of two rows of staggered drift tubes, as displayed in Fig. 3.11 (a), in order to avoid dead regions between adjacent straws. The straw tubes are 2.4 m long with 4.9 mm inner diameter, and are filled with a gas mixture of $Ar/CO_2/O_2$ (70%/28.5%/1.5%), which guarantees a drift time below 50 ns. The anode wire has a diameter of 25 µm, is made of golden plated tungsten and is operated at 1550 V with respect to the tube of Kapton-XC coated with aluminium. The straws wall are only 80 µm thick, ensuring that the total thickness of every T-station is just 3.2% of a radiation length. This is particularly important since, as the measurement of the drift time allows a spatial resolution for the hits of about 200 µm in each detection plane, the measurement of the momenta of charged particles is completely dominated by multiple scattering.

3.2.2 Particle identification and calorimetric system

Čerenkov detectors

Two ring imaging Čerenkov detectors (RICH) are used to discriminate among pions, kaons and protons. It is a well known effect that a charged particle passing through a dielectric medium of refractive index n with a velocity greater than the phase velocity of light in the medium, $\beta > 1/n$, emits Čerenkov photons forming an angle θ_c with respect to the flight direction of the particle, where $\cos\theta_c = 1/(\beta n)$. Knowing the particle momentum and the Čerenkov angle, the mass of

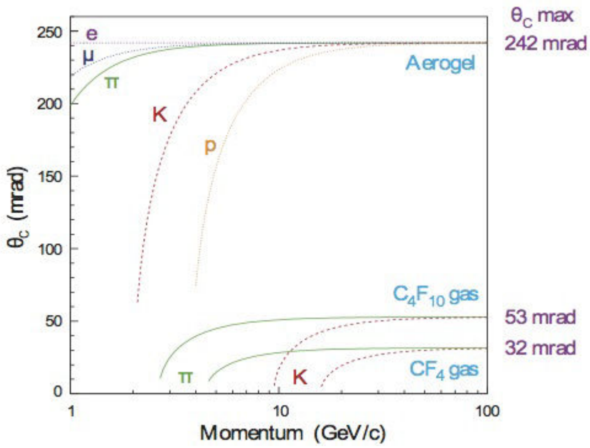

Figure 3.12: Čerenkov angle versus particle momentum for the RICH radiators and for different particle masses. Figure taken from Ref. [38].

the particle can be deduced from the relation

$$\cos\theta_c = \frac{1}{n}\sqrt{1+\left(\frac{mc}{p}\right)^2}.$$

A Čerenkov detector based on a single gas radiator can cover only a finite range velocities, since velocities below $1/n$ do not emit Čerenkov light and hence n cannot be too small whereas, on the other hand, the sensitivity to different values of β increases as n approaches to unity for β approaching unity, requiring n to be as close to unity as possible to distinguish high-momentum particles. As a consequence, in order to cover the full momentum spectrum of the particles produced within its acceptance, LHCb uses two different RICH detectors with different radiators to identify the particle masses in two different ranges of momentum. RICH1, placed right after the VELO and before the TT, uses aerogel ($n = 1.03$) and C_4F_{10} ($n = 1.0014$) gas radiators, covering the momentum range 1–60 GeV/c, whereas RICH2, placed after the T-stations, covers the momentum range from approximately 15 to $\geq 100\,\text{GeV}/c$ using as gas radiator CF_4 ($n = 1.0005$). The characteristic curves of the three radiators in the Čerenkov angle–momentum plane, for the most common particles detected within the LHCb acceptance, are shown in Fig. 3.12.

For both detectors, the Čerenkov photons are read by a lattice of hybrid photon detectors (HPDs) that are able to detect photons in the 200–600 nm spectrum.[6] The HPDs must be placed outside the detector acceptance both to reduce the material budget of the RICHs and to allow their shielding against magnetic fields. Therefore, a complex system of spherical and flat mirrors was designed in order to redirect the Čerenkov photons outside of the LHCb acceptance, towards the HPDs.

Calorimetric system

The calorimetric system of LHCb is designed to measure the energy and provide information for the particle identification of electrons, photons and hadrons. This information is essential for the implementation of the hardware trigger of the experiment, as it will be explained in Sect. 3.3.1. The calorimetric system comprises four different subdetectors:

- two scintillating planes separated by a 2.5 radiation lengths-thick lead plate, the Scintillator Pad Detector (SPD), used to distinguish charged from neutral particles, and the PreShower

[6] The HPD implements a technology similar to that of photomultipliers, but uses a silicon avalanche diode instead of multiple dynodes as electron multiplier.

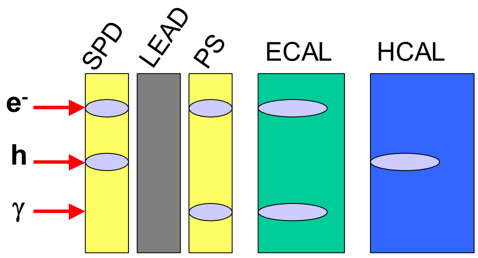

Figure 3.13: Energy deposited in the different subdetectors of the calorimetric system by electrons, hadrons and photons. Figure taken from Ref. [43].

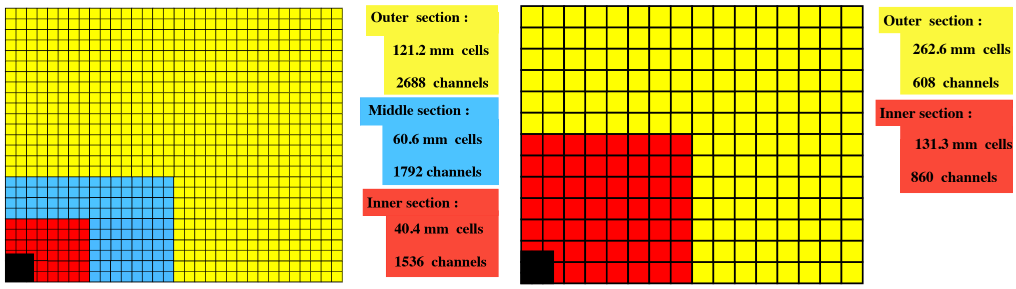

Figure 3.14: Segmentation of one quadrant of the SPD, PS and ECAL (left) and of the HCAL (right). The black sector, corresponding to the beam pipe, is outside of the LHCb acceptance. Figure taken from Ref. [38].

detector (PS), to distinguish electromagnetic showers from hadrons; each of the two subdetectors corresponds to 2 radiation lengths (X_0) and 0.1 nuclear interaction lengths (λ_{int}) thickness;

- the electromagnetic calorimeter (ECAL), consisting of alternating layers of lead and scintillator tiles, for a total thickness of $25\,X_0$ and $1.2\,\lambda_{\text{int}}$, capable of containing all the electromagnetic showers and to measure their energy with resolution $\sigma(E)/E = 1\% \oplus 10\%/\sqrt{E/\,\text{GeV}}$ [42];

- the hadronic calorimeter (HCAL), made up of alternating layers of iron and scintillator tiles, whose thickness (only $5.6\,\lambda_{\text{int}}$) is limited by the space available in the LHCb cavern; as a consequence, the HCAL is used only to estimate the hadron energy for the hardware trigger, but is not used in the offline analysis, because it is not able to contain the full hadronic showers and has therefore a quite poor resolution $\sigma(E)/E = 9\% \oplus 69\%/\sqrt{E/\,\text{GeV}}$ [42].

The energy deposits by different types of particles in the various subdetectors is shown in Fig. 3.13.

Three dimensions are used for the scintillator tiles in the SPD, PS and ECAL (about 4×4 cm, 6×6 cm or 12×12 cm), depending on their distance from the beam pipe, where the occupancy is higher, as shown in Fig. 3.14. The tiles of the HCAL, instead, are divided only in two types: 13×13 cm or 26×26 cm. The geometry of the tiles of the first three detectors is projective with respect to the interaction point, i.e. corresponding tiles in different sections of the detectors cover the same solid angle with respect to it, in order to speed up the transverse energy estimate of the electromagnetic particles by the hardware trigger. An analogous design holds also for the HCAL. All the detectors are read through photomultipliers placed above and below the LHCb acceptance, the scintillating light being transmitted there by wave shifting fibres.

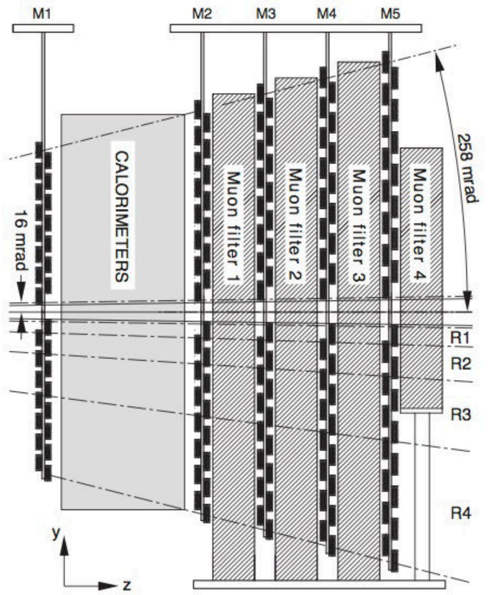

Figure 3.15: Side view of the muon system. Figure taken from Ref. [38].

Muon detectors

The five rectangular-shaped muon stations of the LHCb detector are designed to provide a quick measurement of the muon transverse momentum to the hardware trigger and particle identification information to the software trigger and offline analysis. Stations M2–5 are placed downstream of the HCAL and are interleaved with iron absorbers 80 cm thick to select penetrating muons (Fig. 3.15); only muons with momentum greater than 6 GeV/c pass through all the stations. Station M1, instead, is placed in front of the calorimeters, where effects of multiple scattering are less important, and is used to improve the p_{T} measurement in the trigger.

All stations are instrumented with multiwire proportional chambers, except for the innermost region of the M1 station, which employs triple-GEM detectors to face the higher particle rate that is present near the beam pipe. In both cases, the detection efficiency is over 95%, and the signal is collected in less than 20 ns, allowing the system to be included in the hardware stage of the trigger.

3.3 LHCb trigger and reconstruction system

The LHCb trigger is designed to select the relatively low fraction of collisions containing decays of b- or c-hadrons from the far more frequent background collisions containing only light quark particles.[7] In order to achieve its purpose, it takes advantage of the long flight distance of b- and c-hadrons before decaying, $\mathcal{O}(\,\mathrm{cm})$, and of their relatively high momentum in the plane transverse to the beams.

The trigger scheme (see Fig. 3.16) is divided in three successive phases, that are described in detail in the next sections. The first stage, known as Level-0 trigger (L0), is a hardware trigger fully implemented on custom electronics, and performs a fast, coarse selection of the collisions in order to reduce the input event rate to 1 MHz. The events passing this selection are then processed by a second and third level software triggers, the High Level Trigger 1 (HLT1) and

[7]For example, during 2012 data taking at 8 TeV and $4 \cdot 10^{32}\,\mathrm{cm}^{-2}s^{-1}$ nominal luminosity, about 30 k and 600 k pairs of hadrons containing respectively b and c quarks passed through the LHCb detector each second, whereas the total rate of collisions whose particles passed through the detector was greater than 10 MHz.

High Level Trigger 2 (HLT2), which are run on a dedicated computer farm and perform a full reconstruction of the event in order to select the interesting decays and reduce the event rate to about 5 kHz (12 kHz in Run 2), at which they are recorded on permanent memory to be analysed.

3.3.1 Run 1 trigger

This section describes the core structure of the trigger that was designed for the LHC Run 1. Many of its characteristics have not changed in Run 2.

Level-0 trigger (L0)

The aim of the L0 trigger is to reduce the input collision rate of about 30 MHz to 1 MHz, which is the maximum rate at which the detector channels can be read out by design. This selection must be performed very fast, with a fixed latency of 4 μs. Therefore, it employs only basic information that need not complicated elaboration to perform a rough estimate of the greatest transverse momentum (or energy) of the muons, electrons, photons and hadrons of the event, as great transverse momenta are a distinctive feature of b- and c-hadron decays. Both the reconstruction of the momentum and the choice to select or reject an event basing on this information are performed on custom electronics relying on FPGA technology, and are performed in parallel for the four different trigger lines (L0 hadron, photon, electron and muon).

Calorimeter L0 As mentioned in Sect. 3.2.2, the calorimetric system of LHCb is designed in a projective way, so that corresponding cells in different layers of a calorimeter (and of different calorimetric subsystems) cover the same solid angle with respect to the LHCb nominal interaction point. This fact is employed to provide a quick estimate of the transverse energy of the hadrons, photons and electrons passing through the calorimetric system. The whole calorimeter is divided into clusters of 2×2 cells, large enough to contain most of the energy released by a particle, and small enough to avoid overlaps of different particles. The transverse energy associated to a cluster is estimated as

$$E_{\mathrm{T}} = \sum_{i=0}^{4} E_i \sin\theta_i,$$

where E_i is the energy deposited in the i^{th} cell and θ_i is the angle between the beam axis and a straight line connecting the nominal interaction point of LHCb to the centre of the cell. Then, the energies are summed for correspondent 2×2 clusters along the different layers of the detector, giving the total estimated transverse energy of the particle. The energy of electrons and photons is estimated using only the information coming from the ECAL, and they are distinguished using the charge information provided by the SPD and PS detectors. The energy of the hadrons is estimated using only the data coming from the HCAL but, if the most energetic HCAL cluster corresponds to the ECAL most energetic one, also the energy of the ECAL is summed to that of the HCAL. Only the information about the most energetic particle of its type is considered; if it exceeds a fixed value, which is typically 3.5, 2.4 and 2.8 GeV respectively for hadrons, electrons and photons, the event is retained.

Muon L0 For every hit detected in the M3 chamber, a straight line extrapolation from the interaction point is made. For each muon station M1–5, an area denominated *field of interest* is considered around the extrapolated hit, covering all the possible positions where the muon might have passed, provided that its momentum in the x direction be larger than 0.6 GeV/c. If at least one hit is found in every *field of interest*, then the two hits in the first two stations M1 and M2 are employed to estimate the transverse momentum of the muon, with a precision of about 20%, using look-up tables. The event is retained only if highest transverse momentum of a muon is larger than a threshold, typically 1.5 GeV/c, or if the square root of the product of the two biggest transverse momenta of muons in the event, $\sqrt{p_{\mathrm{T}}(\mu_1) \cdot p_{\mathrm{T}}(\mu_2)}$, is larger than a given threshold, typically 1.3 GeV/c.

High level trigger (HLT)

The complete detector information of the events that passed the L0 trigger is transferred to the disk space of a dedicated computer cluster, the Event Filter Farm (EFF). Here the HLT, a C++ executable, performs a fast full reconstruction of the event and decides whether to memorise permanently it for further analysis or to discard it. The HLT is divided into two successive steps, the HLT1 and the HLT2.

HLT1 At the HLT1 level, a complete 3D reconstruction of the tracks in the VELO is performed in order to find all the primary vertices (PV) produced in the collision. Furthermore, tracks having large impact parameter (IP) with respect to all the PVs are fully reconstructed using also the information from the TT and the T-stations. The event is transferred to the HLT2 only if it contains at least one track with good-quality reconstruction and that has both a large IP with respect to all PVs and a large p_{T}. In this way, the event rate processed by the HLT2 is reduced to about 100 kHz.

HLT2 At the HLT2 level, a full reconstruction of the event is performed, using both the tracking and the particle identification information coming from all the detectors. However, a simplified version of the algorithms employed for the offline analysis is used, due to time constraints, as the L0 output rate and the processing power of the EFF limit the time available to process a single event to about 30 ms (the offline reconstruction takes about 2 s). Events of interest are selected based on the topology of the decays, as well on particle identification data; different types of decays are selected according to different algorithms, and are assigned to different *trigger lines*. The output event rate, about 5 kHz, is limited by the disk storage space available.

3.3.2 Turbo stream in LHCb Run 2

During the first long shutdown between Run 1 and Run 2 (2013–2014), the EFF underwent an upgrade that improved both its processing power and its disk storage resources, taking the second to a total buffer space of 5.2 PB. This allowed a complete revision of the HLT structure [6, 7]. In the new Run 2 data-taking (2015–2018), the total buffer space of the EFF is enough to store the information of all the events recorded in about ten days of continuous data-taking. Accounting for the LHC duty cycle ($\approx$ 30%), this leaves $\approx$ 50 ms to execute the HLT1 and $\approx$ 800 ms to execute the HLT2 on each event, even at the increased HLT2 input rate of 150 kHz (in the Run 1 the time available for the HLT2 was $\approx$ 30 ms and its input rate 100 kHz). As a consequence of the increased time available for the HLT2, the trigger reconstruction has been brought into line with the quality achieved offline. Moreover, the big buffer space available allows the events to be temporarily stored there after the HLT1 processing and before the HLT2 one, while automated calibrations of the detectors are performed using some dedicated HLT1 lines. The scheme of this new trigger flow is displayed on the right part of Fig. 3.16, its direct consequence being the fact that the quality of the data exiting the LHCb trigger in Run 2 is of the same quality as offline data.

This fact opens the way to a completely new paradigm of data collection. If the quality of the data exiting the trigger is comparable to that of reprocessed data, it is possible to perform physics analysis directly with these data, without the need of further offline reconstruction. This is the concept of the *Turbo stream*, which implements this paradigm with at least two evident

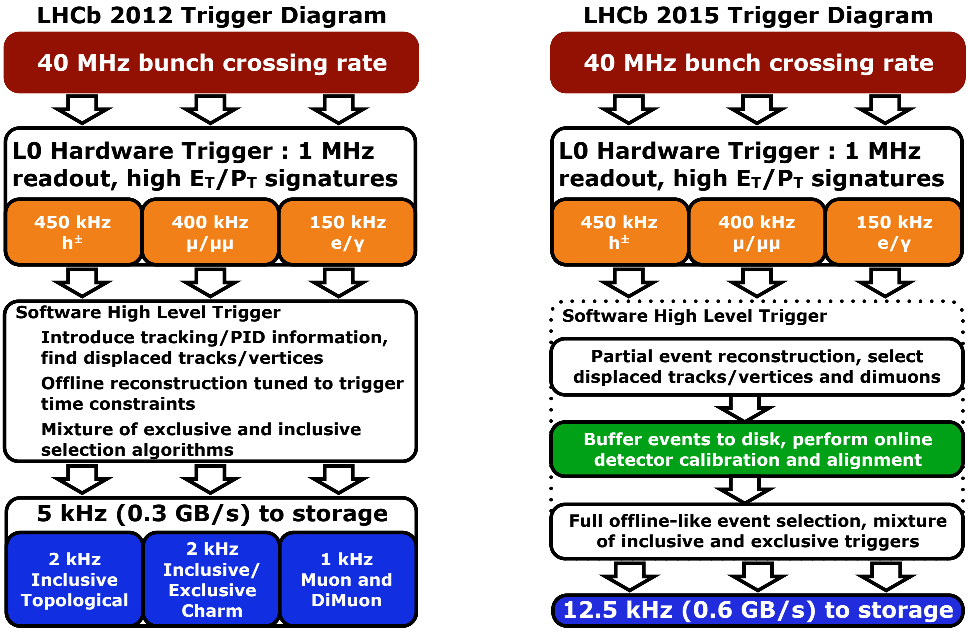

Figure 3.16: LHCb Run 1 trigger scheme (left), compared to the Run 2 scheme (right).

advantages over traditional data recording. First of all, if the specific analysis employs the information about only few particles, only the information regarding these particles (together with that relative to global variables of the event, such as the position of the PVs, the total occupancy of the subdetectors, etc.) is recorded, discarding the data relative to the other particles. As a consequence, the dimension of the average Turbo event is just 5 kB, with respect to the 70 kB of traditional full-information events, allowing a growth of the number of events recorded per unit of time, for equal space-writing rate. Secondly, the time that was required to reprocess the event is saved and can be spent in other tasks, and furthermore the recorded data are available for analysis nearly as soon as they are taken, with clear advantages whenever a trigger line has to be tuned or modified depending on the results obtained in the analysis.

During Run 2, about 5 kHz out of the 12 kHz of events written to tape belong to the Turbo stream. In particular, most of the decays of c-hadrons, including the ones that are analysed in this thesis, are recorded with the Turbo stream, in order to make their high rates affordable for the LHCb trigger. The measurement presented in this thesis is the first high-precision measurement of the LHCb experiment to be performed with the data of the Turbo stream. If this strategy will prove to be successful, the Turbo stream will become the standard data-taking model for the next runs of the LHCb experiment.

3.3.3 LHCb detector performance

A detailed description of the performance of the LHCb detector can be found in Ref. [39]; here we only review the performance of the variables that are more relevant for the A_Γ measurement.

Tracking performance

The relative uncertainty on the momentum of the charged particles passing through all the three tracking subdetectors (referenced as *long tracks*) is about $\delta p/p = 0.5\%$ for particles below $20\,\mathrm{GeV}/c$, rising linearly to 0.8% for particles at $100\,\mathrm{GeV}/c$ (Fig. 3.17(a)), translating in a mass resolution σ_m/m of about 5 per mille up to the Υ masses. The PV resolution depends strongly on the number of track originating in the vertex. For the average number of 25 tracks, the resolution is 13 μm in both the x and y coordinates (Fig. 3.17(b)) and 71 μm in the z coordinate. The resolution of the impact parameter of a long track with respect to a primary vertex is $15 + 29/p_{\mathrm{T}}$ μm, where p_{T} is measured in GeV/c (Fig. 3.17(c)).

Particle identification

Particle identification (PID) in LHCb is performed combining the information gathered by all subdetectors:

- the calorimetric system is used to identify electrons, photons and π^0 (the last two particles can be distinguished analysing the shape of their clusters), and neutral particles are distinguished from charged ones observing the presence of tracks in front of the energy deposits;
- the measurement of the Čerenkov angle in the RICH detectors is employed (Fig. 3.17(d)), together with the momentum measured by the tracking system, to estimate the mass of the particle, with a great discriminating power for pions and kaons;
- muons are recognised looking for hits in the muon stations along the extrapolated trajectory of their tracks, and looking at the overall energy deposited along their trajectory.

The PID information gathered in every subdetector is used to calculate the likelihood for a particle hypothesis X; then, the likelihoods of each subdetector are added linearly to obtain a combined likelihood, $\mathcal{L}(X)$. Usually, the values of this likelihood are compared to that relative to the pion hypothesis, $\mathcal{L}(\pi)$, since pions are the most frequently detected species at LHCb, defining the variable $\mathrm{DLL}_{X\pi} \equiv \log \mathcal{L}(X) - \log \mathcal{L}(\pi)$. $\mathrm{DLL}_{X\pi}$ is a measure of the probability for the particle to be of species X rather than a pion: the larger $\mathrm{DLL}_{X\pi}$, the more likely it is for the particle to belong to the X species. The performance of the $\mathrm{DLL}_{K\pi}$ variable in separating the kaons from the pions is shown in Fig. 3.17(e).

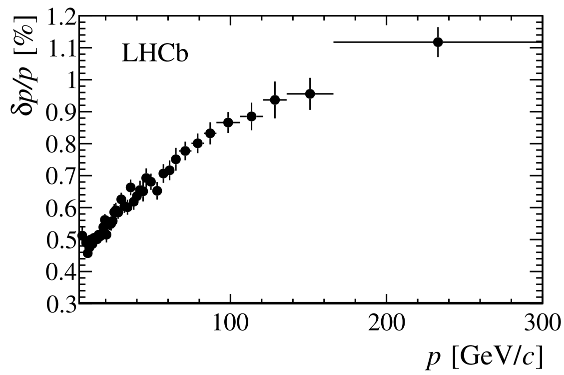

(a) Relative momentum resolution as a function of the momentum for long tracks from the decay of J/ψ particles.

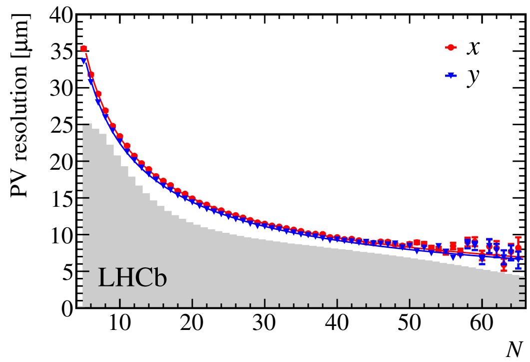

(b) Primary vertex (PV) resolution in the x and y directions, for events with one reconstructed PV, as a function of tracks multiplicity, whose distribution is reported in grey in arbitrary units.

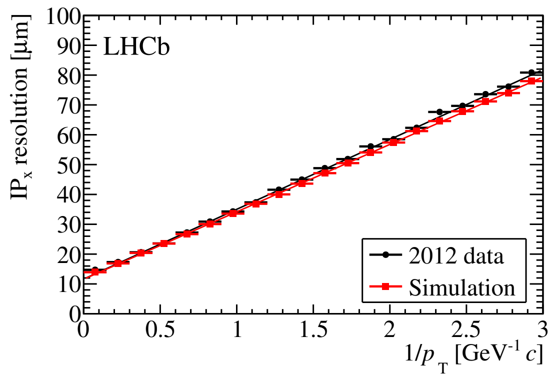

(c) Resolution of the x projection of the impact parameter of long tracks with respect to the primary vertex, as a function of $1/p_{\mathrm{T}}$.

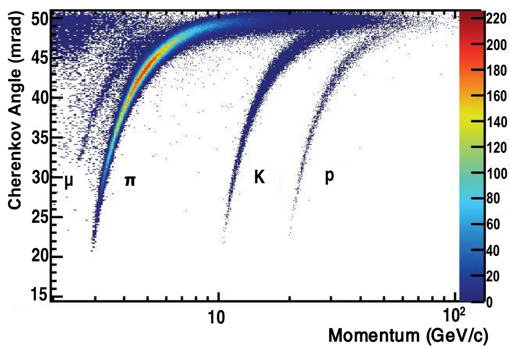

(d) Reconstructed Čerenkov angle for isolated tracks, as a function of track momentum in the C_4F_{10} radiator.

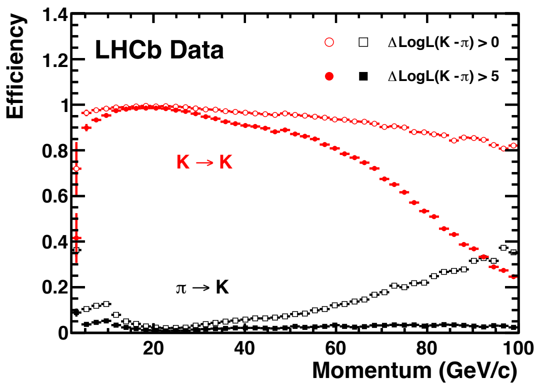

(e) Kaon identification efficiency (red) and pion misidentification rate (black) as a function of track momentum for two different requirements on $\mathrm{DLL}_{K\pi}$.

Figure 3.17: Performance of the LHCb detector. Figures taken from Ref. [39].

Chapter 4

Candidates selection and reconstruction

This chapter describes in detail the trigger and offline requirements to select a pure sample of $D^{*+} \to D^0(\to h^+h^-)\pi^+$ decays, where $h^+h^- = K^-\pi^+$, K^+K^- or $\pi^+\pi^-$,[1] from the overwhelming background of events that are uninteresting for the A_Γ measurement. The main differences with respect to the Run 1 analysis are highlighted. Finally, the total number of collected decays is presented.

4.1 Data sample and event topology

The analysis described in this thesis is performed using the full data sample recorded by the LHCb experiment in *pp* collisions during the LHC Run 2, in 2015 and 2016. The 2015 sample corresponds to $0.28\,\mathrm{fb}^{-1}$ of integrated luminosity, and the 2016 one to $1.46\,\mathrm{fb}^{-1}$; in both cases the centre-of-mass energy of the collisions was 13 TeV. For each sample, about half of the data were collected with the magnetic field pointing upwards (*MagUp*), and the remaining half with the opposite polarity (*MagDown*). The measurement of A_Γ is performed separately in four subsamples, divided according to the year and the magnet polarity. In fact, the data-taking conditions improved from 2015 to 2016, and the opposite magnet polarities are shown to induce different charge asymmetries in the *MagUp* and *MagDown* samples. Therefore, the compatibility among the results in the four subsamples is used to test the reliability and robustness of the analysis procedure.

The $D^{*+} \to D^0\pi^+$ decay chain is reconstructed, where the D^0 decays into final state $h^+h^- = K^-\pi^+$, K^+K^-, $\pi^+\pi^-$. Most D^{*+} are produced in *pp* collisions (primary decays); only a minor fraction comes from the decay of long-lived *b*-hadrons (secondary decays), and is considered as a background of the A_Γ measurement. Since $D^{*+} \to D^0\pi^+$ is a strong decay, the point where the D^0 is produced is completely indistinguishable from the production point of the D^{*+}. The Q-value of the $D^{*+} \to D^0\pi^+$ decay, $\approx 6\,\mathrm{MeV}/c^2$, is much lower than the pion mass. As a consequence, the π^+ that is used to infer the D^0 flavour is produced nearly at rest in the D^{*+} reference frame (as well as the D^0). Therefore, since the mass of the π^+ is much lower than that of the D^0, the momentum of the first is typically much lower than that of the kaons and pions coming from the decay of the D^0, is characterised by a high curvature in the magnetic field and is often referenced as "slow pion" (π_s^+). A further consequence of the low Q-value of the $D^{*+} \to D^0\pi^+$ decay is the fact that the D^0 and the π_s^+ are produced with nearly collinear momenta, resulting in a very poor vertex resolution in the momentum direction, that might be even larger than the flight distance of the D^0. The D^0 lifetime is about 0.41 ps, and its

[1] The inclusion of charge-conjugate processes is implied throughout, wherever not explicitly stated.

average momentum at LHCb is $\approx 60\,\text{GeV}/c$; however, owing to correlations induced by trigger requirements, its mean flight distance is slightly larger than it would be expected, around 1 cm. This allows an excellent discrimination of the D^0 decay vertex from the primary vertex, resulting in a very high purity of D^0 decays in the sample.

4.2 Nomenclature and LHCb trigger variables

Before starting the discussion of the selection of the $D^{*+} \to D^0(\to h^+h^-)\pi^+$ decays, it is useful to introduce some nomenclature and some specific variables that are used throughout the analysis. All the following quantities are calculated in the laboratory frame.

- **Track**: the trajectory corresponding to a set of signals (energy or charge deposits) that are recorded by the detector and that might be due to the passage of a single, charged particle.
- **Long track**: a track is said to be long if it has charge deposits in all the VELO and TT subdetectors, upstream of the magnet, and the T-stations, downstream of the magnet (see Fig. 3.4).
- **Track χ^2/ndf**: χ^2 of the fit of the track, divided by the relative number of degrees of freedom.
- **Track ghost probability**: output of a multivariate classifier quantifying the probability that the track does not correspond to the passage of any real particle. The main causes of misreconstruction are the wrong association of hits belonging to two or more different tracks, principally in the regions of highest occupancy of the detectors, or that are due to detector noise. An additional, lesser cause of error in the tracking is the persistence of real tracks in more than one event, the so called *spillover*, for detectors whose time response is comparable or longer than the time space between two bunches (25 ns). If this is the case, some hits and, possibly, whole tracks might occasionally be taken into consideration in more than one event. Lastly, a source of error is the association of two different track segments in the VELO and in the T-stations.
- **Primary vertex (PV)**: the point of interaction between two protons belonging to the two opposite beams.
- **Impact parameter (IP)**: minimum three-dimensional distance of a particle trajectory from the PV. This variable can be used both to select the decays of long-lived particles, as their decay products are expected to have an IP different from zero on average (whereas the IP of particles produced in the PV is identically null, within experimental sensitivity), and to distinguish primary from secondary decays, by looking at the IP of the D^0 (primary D^0 are produced in the PV, whereas the secondary ones result from the decay of b-hadrons and do not necessarily point back to the PV).
- $\boldsymbol{\chi^2_{\mathrm{IP}}}$: the difference between the χ^2 of the fit of the PV with and without including the track under consideration in the fit; particles that do not come from the PV have larger χ^2_{IP} on average. This variable is nearly equivalent to the IP, but performs slightly better, as it exploits not only the information on the IP, but also on its uncertainty.
- **PV of a particle**: when the collision between two bunches produces more than one PV, every particle is assigned to the PV for which its χ^2_{IP} is minimum.
- **Decay vertex (DV)**: the reconstructed point where a particle decayed.
- **Displacement vector ($\vec{d}$)**: the spatial vector linking the PV to the DV.

- **Proper decay time (t)**: it is calculated assuming that the D^0 meson was produced in the PV,[2] from the relation $\vec{d} = \vec{\beta}\gamma ct = (\vec{p}/m)t$, where $\vec{\beta}$ is the velocity of the D^0 in natural units, γ its relativistic factor, m its invariant mass and $\vec{p}$ its momentum. Owing to the finite experimental precision of LHCb detector in measuring kinematic variables, the momentum of a particle coming from the PV is not always measured to be along its displacement vector. Therefore, before calculating t, a fit of all the kinematic quantities of the particle is performed (spatial trajectory and momentum), with the constraint that it was produced in the PV.

- **Direction angle ($\theta_{\mathbf{DIRA}}$)**: the angle between the momentum of a particle and its displacement vector. It is expected to be null for particles coming from the PV like the primary D^0. It can be used to discriminate them from the secondary decays, for which the momentum of the D^0 is not necessarily aligned to that of its parent b-hadron, and from partially reconstructed decays of the D mesons, where the D momentum is wrongly calculated from only a part of its decay products.[3]

- **Distance of closest approach (DOCA)**: three-dimensional distance between two tracks; if the relative particles were produced in the decay of a same particle, it is expected to be null within experimental sensitivity.

- **χ^2-distance**: a measurement in χ^2 units of the probability of two vertices to coincide. Given two vertices $\vec{x}_1$ and $\vec{x}_2$ with covariance matrices $\mathbf{cov}_1$ and $\mathbf{cov}_2$, it is approximately calculated as $(\vec{x}_1 - \vec{x}_2)^T(\mathbf{cov}_1 + \mathbf{cov}_2)^{-1}(\vec{x}_1 - \vec{x}_2)$.

- **Flight distance χ^2 ($\chi^2_{\mathbf{FD}}$)**: χ^2-distance between the DV of a particle and its PV (*i.e.* a measure of the significance of the displacement vector to be different from zero). It is one of the most discriminating variables used to distinguish the DV of long-lived particles.

- $\mathrm{DLL}_{K\pi}$: the logarithm of the ratio of the likelihood for a particle to be a kaon to that to be a pion (for further details, see Sect. 3.3.3). The higher the $\mathrm{DLL}_{K\pi}$, the higher the probability that the particle is a kaon and not a pion.

- Δm: the difference between the reconstructed invariant mass of the D^{*+} and of the D^0 meson ($\Delta m = m(D^0\pi^+) - m(D^0)$). It has a higher discriminating power in identifying the D^{*+} mesons with respect to the D^{*+} invariant mass, as the experimental error in reconstructing the D^0 mass partially cancels in the difference. It has a natural lower cut-off at the mass of the π^+.

4.3 Trigger selection

The trigger of the LHCb experiment includes some Turbo lines specifically designed to select a pure sample of $D^{*+} \to D^0(\to h^+h^-)\pi^+$ decays. The present analysis is performed on the candidates selected by these lines, that are described in detail in the following sections.

[2]This is true to an excellent approximation for primary decays, since $D^{*+} \to D^0\pi^+$ is a strong decay. This choice allows to greatly improve the decay time resolution (≈ 45 fs), since the resolution on the PV is far better than that on the D^{*+} DV, as the Q-value of the $D^{*+} \to D^0\pi^+$ decay is very low and the D^0 and the π_s^+ are produced with nearly parallel momenta.

[3]One typical case is the three-body decay $D^+ \to K^-\pi^+\pi^+$ where one of the two pions is not detected, but the other one is wrongly assigned the mass hypothesis of a kaon, so that the reconstructed invariant mass of the D^+ remains very similar to that of the D^0.

Table 4.1: L0 thresholds for the main physics lines. For every configuration of the trigger thresholds (represented as a column), the selected fraction of signal events with respect to the sample of the whole year is displayed as well. Additional requirement on the number of SPD hits to avoid events with high number of tracks and high ghost rate: $n_{SPD} < 900$ for `L0DiMuon`, $n_{SPD} < 450$ for the other lines.

	2015						
`L0Hadron` E_{T} (MeV)	3600	3096	4008				
`L0Photon` E_{T} (MeV)	2688	2280	2688				
`L0Electron` E_{T} (MeV)	2688	2280	2688				
`L0Muon` p_{T} (MeV/c)	2800	2400	2800				
`L0DiMuon` $\sqrt{p_{\mathrm{T}1} p_{\mathrm{T}2}}$ (MeV/c)	1300	1300	1300				
Fraction of events (%)	50.4	27.2	22.4				
	2016						
`L0Hadron` E_{T} (MeV)	2928	3216	3552	3696	3696	3696	3744
`L0Photon` E_{T} (MeV)	2112	2304	2784	2976	2832	2976	2784
`L0Electron` E_{T} (MeV)	1872	2112	2256	2592	2352	2592	2400
`L0Muon` p_{T} (MeV/c)	700	1100	1300	1500	1300	1500	1800
`L0DiMuon` $\sqrt{p_{\mathrm{T}1} p_{\mathrm{T}2}}$ (MeV/c)	900	1000	1200	1300	1300	1300	1500
Fraction of events (%)	0.6	3.1	1.9	5.3	44.5	3.6	33.2
	2016						
`L0Hadron` E_{T} (MeV)	3888	3888	3744				
`L0Photon` E_{T} (MeV)	2976	2976	3192				
`L0Electron` E_{T} (MeV)	2616	2616	2376				
`L0Muon` p_{T} (MeV/c)	1500	1600	1350				
`L0DiMuon` $\sqrt{p_{\mathrm{T}1} p_{\mathrm{T}2}}$ (MeV/c)	1400	1500	1550				
Fraction of events (%)	2.9	5.1	0.0				

4.3.1 L0

The five main lines of the L0 trigger are described in Sect. 3.3.1; the values of the thresholds of their requirements during 2015 and 2016 are summarised in Tab. 4.1. Ideally, it would be desirable to require the h^+h^- mesons coming from the decay of the D^0 to fire the hadronic trigger at L0. However, the threshold of the hadronic trigger, $E_{\mathrm{T}}(D^0) \lesssim 3.7\,\mathrm{GeV}$, is considerably higher than those of the other trigger lines, that were designed to select rarer events, its value being limited by the finite rate at which the detector channels can be read out and by the higher rate of hadronic charm decays with respect to other rarer decays involving leptons or photons. Moreover, its reconstruction precision is very limited owing to the approximated procedure that was implemented in the hardware trigger to evaluate the hadrons transverse energy, taking advantage of the projective geometry of the calorimeters, resulting in a low efficiency for the hadronic trigger. As a consequence, very often D^0 with transverse energy even higher than the threshold are not selected by the L0 hadronic trigger. Therefore, more than 60% of the $D^0 \to h^+h^-$ decays that were reconstructed by the HLT did not fire the L0 trigger, that was randomly fired by other particles that are present in the event, instead (this happens as the production cross section of primary D^{*+} is very high, and the probability to find a D^{*+} in a random collision is not negligible). In order not to loose a significant fraction of the decays yield, no requirements on the signal candidates are asked at the L0 level, taking in input the logical OR of all the L0 lines. Even if this choice introduces different momentum thresholds in the data sample, they are not expected to produce significant biases on the final measurement of A_Γ, as it has been verified during the analysis of Run 1 data [4, 30].

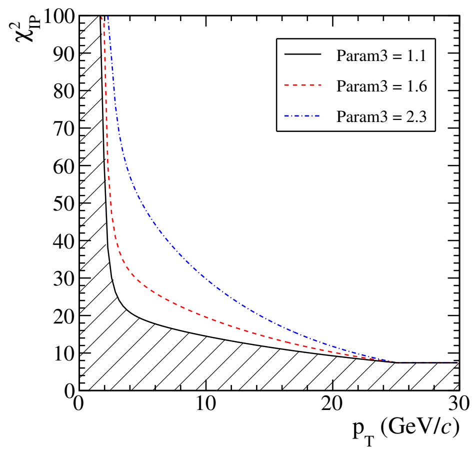

Figure 4.1: Boundary of the region in the track $p_{\rm T} - \chi^2_{\rm IP}$ plane selected by the `Hlt1TrackMVA` line, for the various values of Param3; the shaded area is excluded when Param3 = 1.1.

4.3.2 HLT1

At the HLT1 level, at least one of the particles coming from the decay of the D^0 is required to fire the `Hlt1TrackMVA` line looking for a single track with high $p_{\rm T}$ and significant IP with respect to the PV or, alternatively, the combination of the two particles is required to fire the `Hlt1TwoTrackMVA` line, looking for two high-$p_{\rm T}$ tracks forming a vertex which is displaced from the PV. The trigger thresholds changed slightly four times during the course of the data-taking period, dividing naturally the sample into four subsamples that will be indicated with the letters

(a) corresponding to the whole 2015 data sample and first 18.7% of the 2016 data sample;
(b) corresponding to the 8.0% of the 2016 data sample;
(c) corresponding to the 29.7% of the 2016 data sample;
(d) corresponding to the remaining 43.6% of the 2016 data sample.

The different thresholds for the four subsamples will be explicitly indicated in the following, labelling them with these letters, whenever needed.

The `Hlt1TrackMVA` line is designed to select single, long tracks characterised by good reconstruction quality, high transverse momentum and high IP from all the PVs. The last condition is required in order to select only the tracks coming from the decay of long-lived particles like the D^0 meson, rejecting the much more numerous tracks originating owing to strong interactions in the PV. The conditions on the momentum and on the displacement from the PV, in particular, are enforced requesting that the track satisfies the following relation,

$$\begin{aligned}&\left\{(p_{\rm T} > 25.0) \wedge (\chi^2_{\rm IP} > 7.4)\right\} \vee \\ &\qquad\left\{[1.0 < p_{\rm T} < 25.0] \wedge \left[\ln \chi^2_{\rm IP} > \ln(7.4) + \frac{1.0}{(p_{\rm T} - 1.0)^2} + \text{Param3}\left(1 - \frac{p_{\rm T}}{25}\right)\right]\right\},\end{aligned} \tag{4.1}$$

where the momenta are measured in GeV/c and Param3 is a constant equal to 1.1, 1.6 and 2.3 for (a,d), (b) and (c) subsamples, respectively. The region of the $p_{\rm T} - \chi^2_{\rm IP}$ plane that is selected by the inequality of Eq. (4.1) is represented in Fig. 4.1. The reconstruction quality, instead, is checked requesting both the χ^2 of the fit of the track and the ghost probability to be low.

The `Hlt1TwoTrackMVA` line, which was introduced with the LHC Run 2 and was not present in the Run 1 trigger, looks for couples of long tracks which are both characterised, like for the `Hlt1TrackMVA` line, by good reconstruction quality and high momentum. Looser requirements are requested for the transverse momentum and the $\chi^2_{\rm IP}$ of the single tracks with respect to the

Table 4.2: Selection requirements at HLT1 level; all the tracks are assigned a pion identity hypothesis and the following kinematic variables are calculated consistently. Whenever the threshold values have changed during the data-taking period, the different values are labelled with the subsamples' superscripts.

Line	Candidate	Quantity	Requirement	Unit
`Hlt1TrackMVA`	trk	track χ^2/ndf	< 2.5	–
		ghost probability	$-^{(a)}$, $< 0.2^{(b,c,d)}$	–
		p	$> 3^{(a,b)}$, $> 5^{(c,d)}$	GeV/c
		$p_{\mathrm{T}} - \chi^2_{\mathrm{IP}}$	see Eq. (4.1)	–
`Hlt1TwoTrackMVA`	trk_1, trk_2	track χ^2/ndf($\mathrm{trk}_{1,2}$)	< 2.5	–
		ghost probability($\mathrm{trk}_{1,2}$)	$-^{(a)}$, $< 0.2^{(b,c,d)}$	–
		$p_{\mathrm{T}}(\mathrm{trk}_{1,2})$	$> 500^{(a,b)}$, $> 600^{(c,d)}$	MeV/c
		$p(\mathrm{trk}_{1,2})$	$> 3^{(a,b)}$, $> 5^{(c,d)}$	GeV/c
		$\chi^2_{\mathrm{IP}}(\mathrm{trk}_{1,2})$	> 4	–
	(trk_1+trk_2)	$p_{\mathrm{T}}(\mathrm{trk}_1+\mathrm{trk}_2)$	> 2	GeV/c
		DOCA(trk_1,trk_2) in χ^2 units	< 10	–
		χ^2 of the vertex(trk_1,trk_2) fit	< 10	–
		$\eta\,\{\text{vertex}(\mathrm{trk}_1,\mathrm{trk}_2), \text{PV}\}$	$\in [2, 5]$	–
		$m_{\mathrm{corr}}(\mathrm{trk}_1 + \mathrm{trk}_2)$	> 1	GeV/c^2
		$\theta_{\mathrm{DIRA}}(\mathrm{trk}_1 + \mathrm{trk}_2)$	> 0	–
		output of the classifier	$> 0.95^{(a,b,d)}$, $> 0.97^{(c)}$	–

`Hlt1TrackMVA` line but, in addition, the two tracks are required to be consistent with coming from the same DV of a particle with high transverse momentum and significantly displaced from the PV. This last condition is enforced considering the output of a boosted-decision-tree-based (BDT), proprietary classifier by Yandex that takes in input the following variables:

1) χ^2-distance between the PV and the two tracks' vertex (abbreviated as flight distance χ^2, or χ^2_{FD});
2) sum of the p_{T} of the two tracks, $p_{\mathrm{T}}\,(h^+) + p_{\mathrm{T}}\,(h^-)$;
3) number of tracks with $\chi^2_{\mathrm{IP}} > 16$;
4) χ^2 of the two tracks' vertex fit.

The complete list of HLT1 requirements, for both `Hlt1TrackMVA` and `Hlt1TwoTrackMVA` lines, is displayed in Table 4.2. Some of the variables that are used in the selection of the `Hlt1TwoTrackMVA` line might need further explanation:

- DOCA(trk_1,trk_2) in χ^2 units is a measure of the significance for two tracks to have passed through a same point, *i.e.* the D^0 decay vertex;
- $\eta = -\log(\tan\theta/2)$ is the parametrisation *via* pseudorapidity of the polar angle (*i.e.* the angle with respect to the z axis) of the displacement vector between the PV and the vertex of the two tracks;
- the corrected mass is defined as $m_{\mathrm{corr}} \equiv \sqrt{m^2 + \vec{p_{\mathrm{T}}}^2} + \vec{p_{\mathrm{T}}}$, where $\vec{p_{\mathrm{T}}}$ is the component of the momentum of the combination of the two tracks transverse to their displacement vector, $|\vec{p_{\mathrm{T}}}| = p\sin\theta_{\mathrm{DIRA}}$ with p and θ_{DIRA} referred to the combination of the two tracks. This variable was developed to (partially) correct the value of the mass of the long-lived particles that are not entirely reconstructed, for example because they decayed leptonically, with the emission of a neutrino. In this case, the particle measured mass is lower than its real mass, and its measured θ_{DIRA} is in general different from zero, even if the particle was produced in the PV. The corrected mass is the minimum mass of the reconstructed

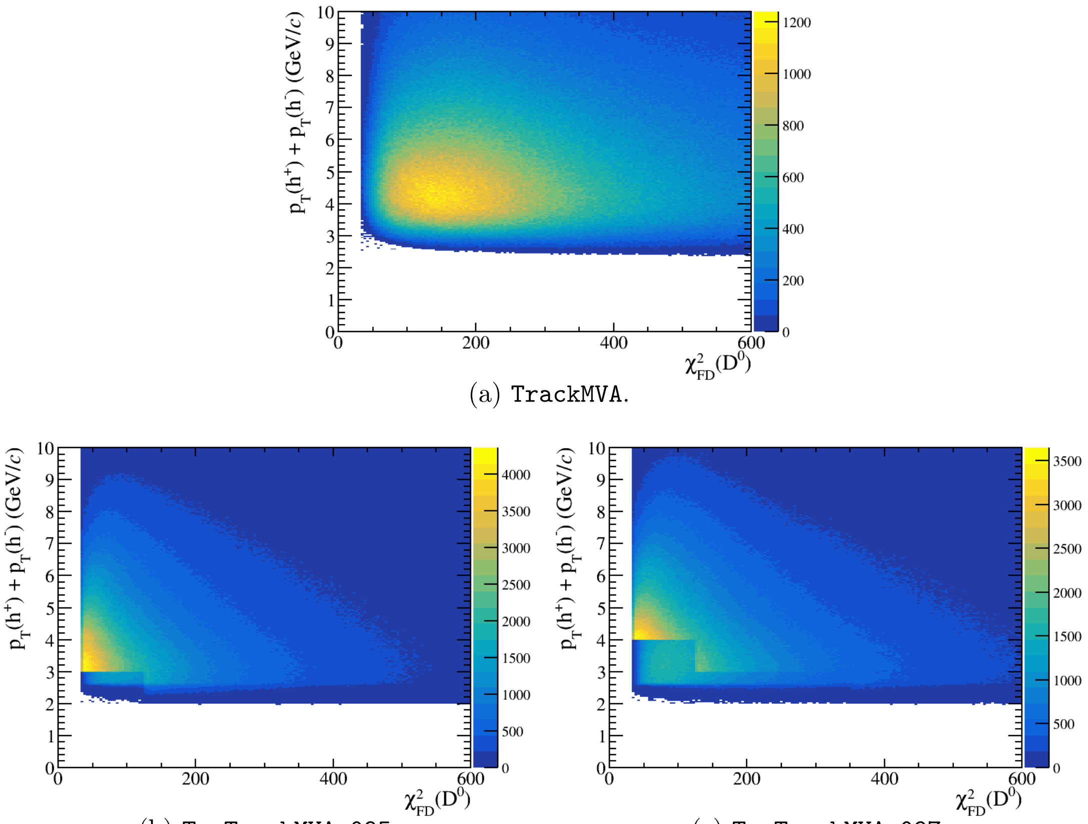

(a) `TrackMVA`.

(b) `TwoTrackMVA_095`.

(c) `TwoTrackMVA_097`.

Figure 4.2: Distribution of the signal events in the $[p_\mathrm{T}(h^+) + p_\mathrm{T}(h^-)] - \chi^2_\mathrm{FD}$ plane, separately for every HLT 1 line and classifier threshold. The multiple rectangular cuts introduced by the classifier are well visible in the plots relative to the two-track line.

particle, obtained by adding to its measured momentum some transverse momentum from massless undetected particles, needed to put θ_DIRA equal to zero. In the case of $D^0 \to h^+h^-$ decays, no further particles are missing and the corrected mass is equal to the reconstructed invariant mass, within experimental sensitivity;

- $\mathrm{DIRA}(\mathrm{trk}_1 + \mathrm{trk}_2) > 0$ requires that the reconstructed vertex of the two tracks does not lie behind the PV.

During the analysis, it was found that the classifier cuts on the $[p_\mathrm{T}(h^+) + p_\mathrm{T}(h^-)] - \chi^2_\mathrm{FD}$ plane (see Fig 4.2) have a significant impact on the measurement of A_Γ. Therefore, in the next chapter the whole sample is often subdivided in three subsamples according to the HLT1 trigger line and, for the two-tracks line, to the threshold of the classifier: `TrackMVA`, `TwoTrackMVA_095` and `TwoTrackMVA_097`. The non null overlap among the three subsamples is shown, divided by year and magnet polarity, in Fig. 4.3.

4.3.3 HLT2

At the HLT2 level, the $D^{*+} \to D^0(\to h^+h^-)\pi^+$ decays are selected by the `Hlt2CharmHadDstp2D0Pip_D02xxTurbo` lines, where `xx` stands for `KmKp`, `PimPip` or `KmPip`, that are specifically designed to identify the $D^0 \to K^+K^-$, $D^0 \to \pi^+\pi^-$ and $D^0 \to K^-\pi^+$ primary decays, respectively. All the lines share the same requirements, except that on the particle identification of the $h^\pm$ hadrons coming from the decay of the D^0, which is used to discriminate the $K^\pm$ from the $\pi^\pm$, thus distinguishing the three decay modes.

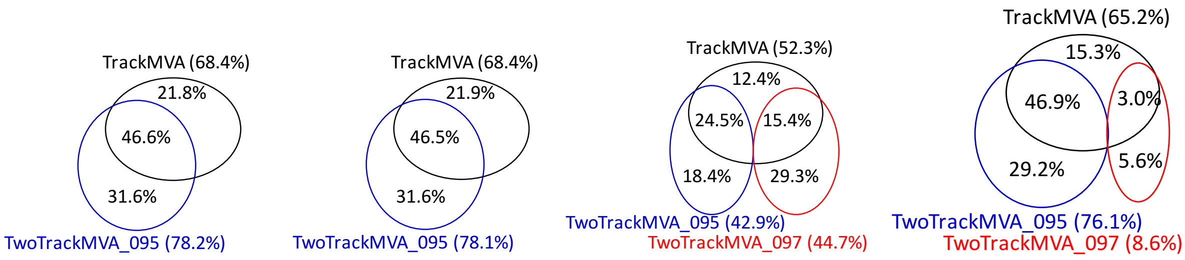

(a) 2015 *MagUp*. (b) 2015 *MagDown*. (c) 2016 *MagUp*. (d) 2015 *MagDown*.

Figure 4.3: Fraction of signal events selected by the different HLT1 lines, where the two-tracks line has been divided according to the classifier threshold.

Table 4.3: Selection requirements of the HLT2.

Candidate	Quantity	Requirement	Unit
$h^{\pm}$	track $\chi^2/\mathrm{ndf}(h^{\pm})$	< 3	–
	$p_{\mathrm{T}}(h^{\pm})$	> 800	MeV/c
	$p(h^{\pm})$	> 5	GeV/c
	$\chi^2_{\mathrm{IP}}(h^{\pm})$	> 4	–
	$\mathrm{DLL}_{K\pi}(K^{\pm})$	> 5	–
	$\mathrm{DLL}_{K\pi}(\pi^{\pm})$	< 5	–
D^0	p_{T} of at least one associated $h^{\pm}$	> 1	GeV/c
	$\mathrm{DOCA}(h^+, h^-)$	< 0.1	mm
	$p_{\mathrm{T}}(D^0)$	> 2	GeV/c
	$m(D^0)$	$\in [1715, 2015]$	MeV/c^2
	fit of D^0 vertex χ^2/ndf	< 10	–
	$\chi^2_{\mathrm{FD}}(D^0)$	> 25	–
	$\theta_{\mathrm{DIRA}}(D^0)$	< 17.3	mrad
π_s^+	track $\chi^2/\mathrm{ndf}(\pi_s^+)$	< 3	–
	$p_{\mathrm{T}}(\pi_s^+)$	> 100	MeV/c
	$p(\pi_s^+)$	> 1	GeV/c
D^{*+}	fit of D^{*+} vertex χ^2/ndf	< 25	–
	$\Delta m = m(D^{*+}) - m(D^0)$	$\in [130, 160]$	MeV/c^2

The full list of requirements of the HLT2 is reported in Table 4.3. Only tracks of good quality ($\chi^2/\mathrm{ndf} < 3$) and displaced from the PV ($\chi^2_{\mathrm{IP}} > 4$) are considered as candidates to be a decay product of a D^0; a requirement on the momentum and on the transverse momentum of these tracks is applied, as well ($p > 5\,\mathrm{GeV}/c$ and $p_{\mathrm{T}} > 800\,\mathrm{MeV}/c$). Then, the candidate tracks are classified as pions or kaons according to the particle identification information, looking if $\mathrm{DLL}_{K\pi}$ is lesser or greater than 5, respectively. They are assigned the relative mass hypothesis, and all the possible combinations of two of these particles are made. A combination of two particles is selected as D^0 candidate only if they have opposite charge, and their tracks form a good vertex. The vertex is required to be significantly displaced from the PV ($\chi^2_{\mathrm{FD}}(D^0) > 25$); moreover, the D^0 is requested to point to the PV ($\theta_{\mathrm{DIRA}}(D^0) < 17.3\,\mathrm{mrad}$) and to have a high transverse momentum. A loose cut on the D^0 mass is performed, too.

At this point, all the possible combinations between the D^0 and the other charged tracks that are present in the event (with pion mass hypothesis) is performed, looking for a good

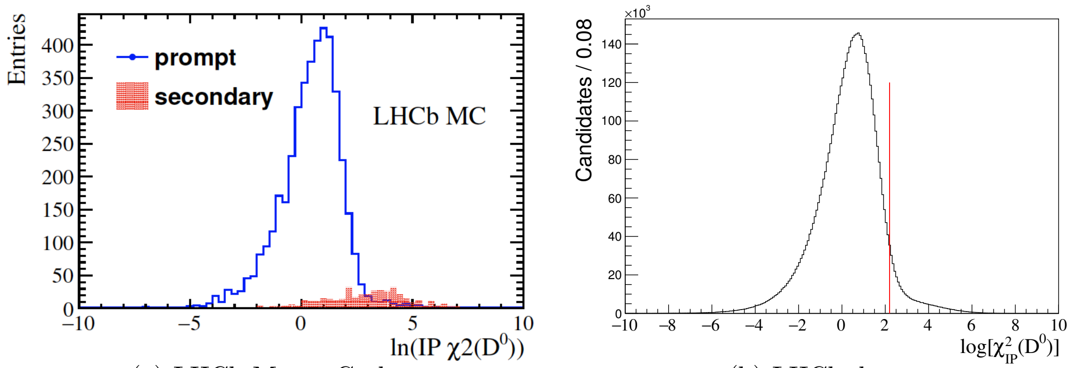

(a) LHCb Monte Carlo. (b) LHCb data.

Figure 4.4: Distribution of $\log[\chi^2_{\text{IP}}(D^0)]$ for the Monte Carlo, distinguishing between the primary and the secondary decays, and for the data recorded in LHCb Run 2. In the right plot, the cut $\chi^2_{\text{IP}}(D^0) < 9$ is shown. Left figure taken from Ref. [30].

$D^{*+} \to D^0\pi^+$ candidate. Minimal requirements are made on the track quality and on the momentum of the slow pion, but not on its particle identification information, as it is known to be strongly charge-dependent, in order not to introduce undesired charge asymmetries in the data sample between $D^{*+} \to D^0\pi^+$ and $D^{*-} \to \overline{D}{}^0\pi^-$ decays. Finally, the fit quality of the $D^{*+} \to D^0\pi^+$ vertex is requested to be good and a loose requirement on Δm is made.

4.4 Offline selection

On top of the trigger selection, some additional requirements are imposed to further improve the purity of the data sample. First of all, the particle identification requirements for the pions coming from the decay of the D^0 are tightened, requiring $\text{DLL}_{K\pi}(\pi^\pm) < -5$, reducing the contamination from misidentified decays. Then, the contamination from secondary decays is reduced requesting the D^0 to have an χ^2_{IP} lesser than 9 (Fig. 4.4). An additional requirement is used to reject D^0 that were not produced by the PV collision, but in the interaction of hadrons produced in the collision with the RF-foils that protect the VELO. In fact, their reconstructed proper decay time, calculated supposing that they were produced in the PV, is meaningless and must be discarded. This is achieved looking at the z coordinate of the DV and at the distance between the PV and the DV in the plane transverse to the beam,

$$R_{xy} = \sqrt{[x(\text{DV}) - x(\text{PV})]^2 + [y(\text{DV}) - y(\text{PV})]^2}. \tag{4.2}$$

As it is shown in Fig. 4.5, the cut $\{R_{xy} < 4\,\text{mm}\} \wedge \{|z(\text{DV})| < 200\,\text{mm}\}$ rejects all the D^0 originated on the RF-foil and decayed soon thereafter, as well as those unexplained that originated in the two ovoid regions on the right and on the left of the bunches nominal collision region.[4] Finally, a tighter cut on the D^0 mass is done, requiring the candidates mass to lie within two sigma from its nominal central value, $1864.5\,\text{MeV}/c^2$. As the D^0 decay is a weak decay, the width of the distribution of the reconstructed D^0 mass is completely dominated by the experimental resolution, that is slightly different for the three channels of decay owing to the cuts on the $\text{DLL}_{K\pi}$, being $8.8\,\text{MeV}/c^2$, $7.1\,\text{MeV}/c^2$ and $9.4\,\text{MeV}/c^2$ for the $D^0 \to K^-\pi^+$, $D^0 \to K^+K^-$ and $D^0 \to \pi^+\pi^-$ decay channels, respectively (Fig. 4.6).

The offline selection requirements are summarised in Table 4.4. The last offline requirement on the Δm, in order to select a pure sample of $D^{*+} \to D^0\pi^+$ decays, is slightly more complex, and is therefore described in the next section.

[4] During Run 1, these regions were not observed.

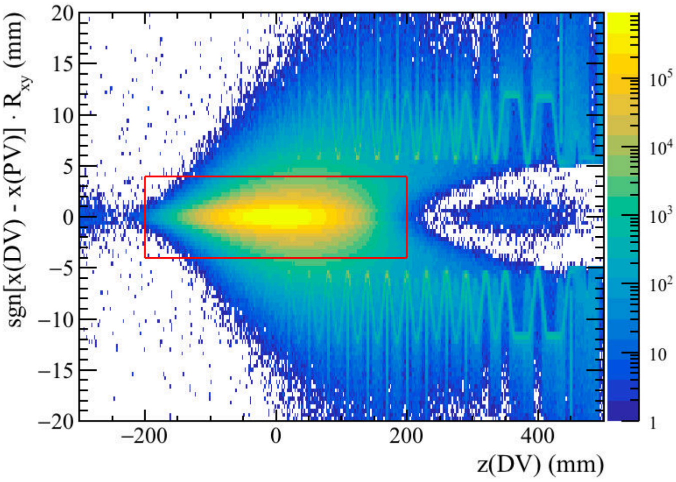

Figure 4.5: z coordinate of the D^0 DV versus its signed radial distance with respect to the PV (definition in Eq. 4.2). The vertical lines of the sensors of the VELO and the wavy shape of the shielding RF-foil are well visible in the regions $R_{xy} \geq 5\,\mathrm{mm}$; only the candidates within the red rectangle are selected by the offline requirements ($R_{xy} < 4\,\mathrm{mm} \wedge |z(\mathrm{DV})| < 200\,\mathrm{mm}$).

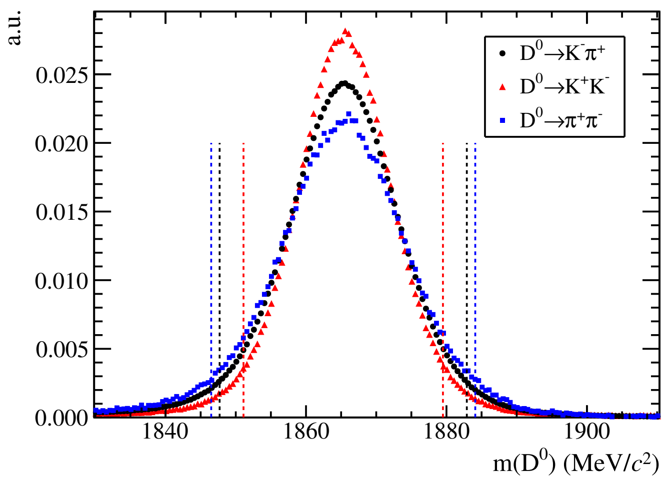

Figure 4.6: Normalised distributions of the D^0 invariant mass for the $D^0 \to K^-\pi^+$, $D^0 \to K^+K^-$ and $D^0 \to \pi^+\pi^-$ decays (2015, *MagUp*). The dashed lines define the signal window.

Table 4.4: Selection requirements imposed on top of the LHCb trigger. The experimental resolution on the D^0 mass, σ_{exp}, is equal to $8.8\,\mathrm{MeV}/c^2$, $7.1\,\mathrm{MeV}/c^2$ and $9.4\,\mathrm{MeV}/c^2$ for the $D^0 \to K^-\pi^+$, $D^0 \to K^+K^-$ and $D^0 \to \pi^+\pi^-$ decay channels, respectively.

Quantity	Requirement	Unit
$\mathrm{DLL}_{K\pi}(\pi^\pm)$	< -5	–
$\chi^2_{\mathrm{IP}}(D^0)$	< 9	–
R_{xy}	< 4	mm
$\lvert z(\mathrm{DV})\rvert$	< 200	mm
$m(D^0)$	$\in [1864.5 - 2\sigma_{\mathrm{exp}}, 1864.5 + 2\sigma_{\mathrm{exp}}]$	MeV/c^2

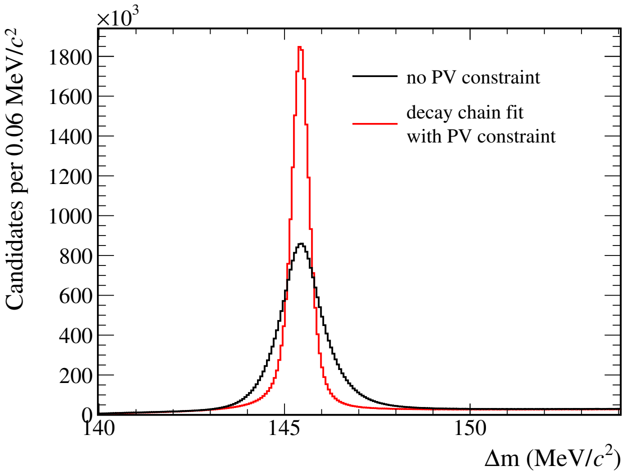

Figure 4.7: Distribution of Δm before and after applying the global kinematic fit of the $D^{*+} \to D^0(\to h^+h^-)\pi^+$ decay chain, constraining the D^{*+} to be produced in the PV.

4.5 Multiple candidates and Δm sideband subtraction

After the selection described in the last sections, the sample comprises a very pure sample of D^0 decays. However, in a significant fraction of events, more than one pion is combined with the same D^0 to form a D^{*+} candidate. In order to avoid double counting of the same candidate, whenever more than one slow pion is associated to the same D^0, only one pion is randomly selected to form a D^{*+} candidate. In particular, this happens in about 6% of $D^0 \to K^-\pi^+$, 11% of $D^0 \to K^+K^-$ and 13% of $D^0 \to \pi^+\pi^-$ decays. As the nature of this association is purely combinatorial, approximately the same percentage of events with multiple candidates would be expected for all three channels. Moreover, the probability of random associations of a D^0 with positive and negative pions is expected to be the same.[5] However, in the analysed sample the percentage of multiple events for $D^0 \to K^+K^-$ and $D^0 \to \pi^+\pi^-$ decays is about the double of that of $D^0 \to K^-\pi^+$ decays, since whenever a $D^0 \to K^-\pi^+$ decay is associated with a negative slow pion, it is not classified as a Cabibbo-favoured $D^0 \to K^-\pi^+$ decay any longer, but as a doubly Cabibbo-suppressed $\overline{D}^0 \to K^-\pi^+$ decay, going to a different Turbo line than those employed in this analysis.

Obviously, about half the time the choice made on the pion to associate to the D^0 (and, therefore, also the D^0 flavour identification) is wrong, and a residual background due to wrong associations survives. Its Δm distribution grows smoothly, with a square-root-like shape, after a threshold corresponding to the charged pion mass, $\approx 139.6\,\text{MeV}/c^2$, as can be seen in Fig. 4.7 (black colour). In order to improve the Δm resolution, thereby improving also the signal to noise ratio in the Δm peak region, a global kinematic fit of the $D^{*+} \to D^0(\to h^+h^-)\pi^+$ decay chain is performed, constraining the D^{*+} to be produced in the PV, following the procedure described in Ref. [44]. This approach allows to improve the measurement of the small angle between the momenta of the D^0 and of the π_s^+, that is the main cause of uncertainty in the value of the Δm. The gain in resolution, which amounts to a factor of 2, is displayed in Fig. 4.7.

In order to remove the residual background under the Δm peak, that is completely undistinguishable from the signal, a sideband subtraction is performed defining a signal range corresponding to a central interval containing 95% of signal candidates ($\approx 2\sigma$), $[144.45, 146.45]\,\text{MeV}/c^2$, and a sideband region containing only combinatorial background, $[149.00, 154.00]\,\text{MeV}/c^2$, that is assumed to behave in the same way of the residual background in the signal region.[6] From here

[5] Asymmetries between the number of π^+ and π^- produced in the event are neglected.

[6] An interval is said to be central if the right and left tails of the distribution around it are equally populated.

on out, all distributions of kinematic variables are filled with a weight that is:

- equal to unity, if their Δm is inside the signal region;
- equal to the opposite of the ratio of the number of background candidates inside the signal region to the number of background candidates in the sideband region, if their Δm is inside the sideband region.

The number of background events in the two regions is extracted through a maximum likelihood fit of the Δm distribution, separately for the four different data-taking periods $\{2015,\ 2016\} \times \{\textit{MagUp},\ \textit{MagDown}\}$, but integrated on the decay times and other kinematic variables. Of course, the procedure is expected to be effective only if the kinematic distributions of the background in both regions are similar, an assumption that is expected to hold as the background is of combinatorial nature. Deviations from this behaviour are assessed in the systematic uncertainties (see Chap. 7).

In the fit, the signal candidates are modelled through the sum of a Johnson distribution [45], $\mathcal{J}$, and three Gaussians, $\mathcal{G}$, as

$$\begin{aligned}\mathcal{P}_{\rm sgn}(\Delta m;\boldsymbol{\theta}_{\rm sig}) = \;& f_J \cdot \mathcal{J}(\Delta m;\mu_J,\sigma_J,\delta_J,\gamma_J) + f_1 \cdot \mathcal{G}(\Delta m;\mu_1,\sigma_1) && (4.3)\\ &+ f_2 \cdot \mathcal{G}(\Delta m;\mu_2,\sigma_2) + (1-f_J-f_1-f_2)\cdot \mathcal{G}(\Delta m;\mu_3,\sigma_3), && (4.4)\end{aligned}$$

where

$$\mathcal{J}(\Delta m;\mu_J,\sigma_J,\delta_J,\gamma_J) = \frac{1}{I_J}\frac{\exp\left\{-\frac{1}{2}\left[\gamma_J+\delta_J\cdot\sinh^{-1}\left(\frac{\Delta m-\mu_J}{\sigma_J}\right)\right]^2\right\}}{\sqrt{1+\left(\frac{\Delta m-\mu_J}{\sigma_J}\right)^2}}, \tag{4.5}$$

$$\mathcal{G}(\Delta m;\mu,\sigma) = \frac{1}{I_G}\exp\left[-\frac{1}{2}\left(\frac{\Delta m-\mu}{\sigma}\right)^2\right], \tag{4.6}$$

I_J and I_G are the proper normalisation factors in the fit range $[140, 154]\,\mathrm{MeV}/c^2$ and $\boldsymbol{\theta}_{\rm sig} = (f_J,\mu_J,\sigma_J,\delta_J,\gamma_J,f_1,\mu_1,\sigma_1,f_2,\mu_2,\sigma_2,\mu_3,\sigma_3)$ is the vector of the signal parameters to be fitted to the data. The random pions background, instead, is modelled with an empirical threshold function

$$\mathcal{P}_{\rm bkg}(\Delta m;\boldsymbol{\theta}_{\rm bkg}) = \frac{1}{I_B}\left[1-\exp\left(-\frac{\Delta m - m_0}{\alpha}\right)+\beta\left(\frac{\Delta m}{m_0}-1\right)\right]$$

where I_B is the normalisation factor and $\boldsymbol{\theta}_{\rm bkg} = (m_0,\alpha,\beta)$ is the vector of background parameters. The total, extended probability density function, can thus be written as

$$\mathcal{P}(\Delta m;\boldsymbol{\theta}) = \frac{N_{\rm sgn}}{N_{\rm sgn}+N_{\rm bkg}}\mathcal{P}_{\rm sgn}(\Delta m;\boldsymbol{\theta}_{\rm sig}) + \frac{N_{\rm bkg}}{N_{\rm sgn}+N_{\rm bkg}}\mathcal{P}_{\rm bkg}(\Delta m;\boldsymbol{\theta}_{\rm bkg})$$

where $\boldsymbol{\theta} = (N_{\rm sig}, N_{\rm bkg}, \boldsymbol{\theta}_{\rm sig}, \boldsymbol{\theta}_{\rm bkg})$ are all the parameters to be fitted to the data. An example of a fit is reported in Fig. 4.8. The purity in the signal region is found to be nearly independent of the subsample $\{2015,\ 2016\} \times \{\textit{MagUp},\ \textit{MagDown}\}$, and is about 96%, 93% and 88% for the $D^0 \to K^-\pi^+$, $D^0 \to K^+K^-$ and $D^0 \to \pi^+\pi^-$ samples, respectively.

4.6 Signal yield

The final number of candidates after the sideband subtraction is displayed in Table 4.5. The size of the data sample has more than doubled with respect to the Run 1 analysis, although the total integrated luminosity has nearly halved. The increase of the number of candidates per integrated

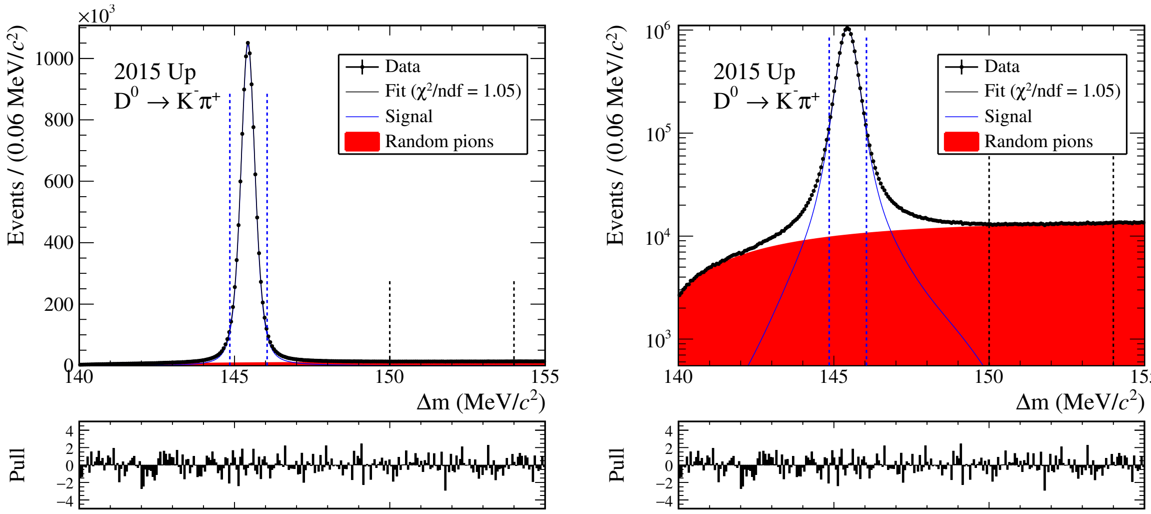

(a) Linear scale.

(b) Logarithmic scale.

Figure 4.8: Distribution of the mass difference Δm for the $D^0 \to K^-\pi^+$ decays in the 2015 *MagUp* period. The fit result and the residuals of the data with respect to the fit curve are also shown.

Table 4.5: Number of signal candidates after the Δm sideband subtraction, in millions; the total number of candidates collected in the Run 1 analysis is reported for comparison.

Data sample	$\int \mathcal{L}\,\mathrm{d}t$ (fb^{-1})	$D^0 \to K^-\pi^+$	$D^0 \to K^+K^-$	$D^0 \to \pi^+\pi^-$
2015 *MagUp*	0.12	12.2	1.4	0.42
2015 *MagDown*	0.16	19.1	2.1	0.52
2016 *MagUp*	0.71	79.1	8.9	2.8
2016 *MagDown*	0.75	83.1	9.5	3.0
tot Run 2 (2015–2016)	1.74	193.5	21.9	6.7
tot Run 1 (2011–2012)	3.19	87.5	9.6	2.98

luminosity, by about a factor of 4, can be ascribed to several factors. First, the production cross section of charm quarks in *pp* collisions has increased, passing from 7–8 TeV to 13 TeV, by a factor of 1.8 [5]. Second, the HLT1 two-tracks line, that selected more than one third of all the collected decays in addition to the single-track line, was not present in Run 1. Third, the reduction of the amount of data needed to record one event in Run 2 with respect to Run 1, thanks to the implementation of the Turbo paradigm in the trigger, and the parallel increase of the rate at which data are stored to disk, allowed to loosen some of the trigger requirements, particularly on the flight distance of the D^0.

Handling huge amount of data introduces relevant computing difficulties into the analysis.[7] For example, filling a single histogram with the data from just one subsample requires about 15 minutes, and the time needed to read the data that are used to perform the determination of A_Γ for the whole data sample is of the order of two hours. Most of the tests shown in the next two chapters have been performed multiple times with different selection requirements; moreover, they had to be performed on the whole data sample, since the analysis of a partial amount of data would not have been able to evidence possible systematic deviations, as small as $\mathcal{O}(10^{-4})$, caused by the approximations of the analysis procedure. Therefore, a consistent part of the work

[7] Another problem is to assure a good convergence of the fits for all the decay modes and data subsamples.

of this thesis has been devoted to the reduction of the time needed to analyse the data, and to re-execute the analysis with modified analysis parameters. In particular, the analysis framework that was developed, mainly based on the BASH programming language, makes extensive use of parallelisation, allowing for a reduction of the time needed to read the data by about a factor of 5, and is designed to allow executing the whole analysis—contemporarily for all three decay modes and all four data subsamples—in a semi-automated way multiple times.

The studies that are presented in the next two chapters show that the requirements of the new Run 2 two-track HLT1 line introduce some undesired correlations between the kinematic variables of the decaying particles, whose effects on the measurement of A_Γ are not completely understood to date. Moreover, the reduction of the systematic uncertainty due to the contribution to the measured A_Γ from secondary decays requires a modification of the data selection, as described in Chap. 6. Therefore, the final selection requirements that are adopted in order to perform the preliminary measurement of A_Γ with the data of the 2015–2016 data-taking period of Run 2 that is presented in this thesis are slightly different from those described in this chapter, that are mainly inspired by the previous measurement of A_Γ with the data of LHCb Run 1. They are described in Sect. 6.3, while the final yields and the projections of the fits to the Δm distributions for all decay modes and subsamples are displayed in Sect. 7.1.

Chapter 5

Detector-induced time-dependent charge asymmetries

This chapter pinpoints the origin of the detector-induced, time-dependent charge asymmetries that have been introduced in Sect. 2.2.2, highlighting both the origin of the correlations between the D^0 decay time and the slow pion momentum, and that of the detection asymmetries dependent on the momentum of the slow pion. Then, the correction procedure that is used to neutralise these effects is presented, and the impact on the A_Γ measurement of the requirements of the various HLT1 lines that have been introduced in Run 2 is assessed. Finally, the main features of an ideal trigger that should be satisfied to guarantee a better precision in the foreseen measurements of A_Γ with larger statistics are identified, and the final selection that is used for this preliminary measurement with the data of 2015 and 2016 is chosen.

5.1 Introduction

The measurement of A_Γ is performed in this thesis through the method of the linear fit to the time-dependent asymmetry between the number of reconstructed $D^0(t) \to f$ and $\overline{D}^0(t) \to f$ decays, with $f = K^+K^-$, $\pi^+\pi^-$, that is described in Sect. 2.2.2. As it is reported in Eq. (2.1), this raw asymmetry can be written as

$$A_{\text{raw}}(t) \approx A_{CP}^{\text{dir}} - A_\Gamma \cdot \frac{t}{\tau_{D^0}} + A_{\text{D}}^{\pi_s}(t) + A_{\text{P}}(t), \tag{5.1}$$

where $A_{\text{D}}^{\pi_s}(t)$ is the detection asymmetry due to the different efficiencies in reconstructing the positive and negative slow pions that are used to infer the flavour of the D^0 meson at production and $A_{\text{P}}(t)$ is the production asymmetry between D^{*+} and D^{*-} mesons, caused by the fact that the initial *pp* state at LHC is not *CP*-symmetric. If these two terms did not depend on the proper decay time of the D^0, they would not affect the measurement of A_Γ, that is sensitive only to time-dependent asymmetries. However, as it will be shown in the next sections, they exhibit slight time dependencies owing to complex correlations among the kinematic variables of the event, including the D^0 decay time, that are induced by the trigger requirements, and to momentum-dependent detection asymmetries. This effect can be significant, and must be corrected up to a precision better than that on the final measurement of A_Γ.

The studies to develop and assess the performance of the needed correction procedure are carried out on the Cabibbo-favoured $D^0 \to K^-\pi^+$ sample, where no *CP* violation is expected to be detectable within the current experimental sensitivity. For these decays, the raw asymmetry can be written as

$$A_{\text{raw}}^{K\pi}(t) = A_{\text{D}}^{\pi_s}(t) + A_{\text{D}}^{K\pi}(t) + A_{\text{P}}(t)$$

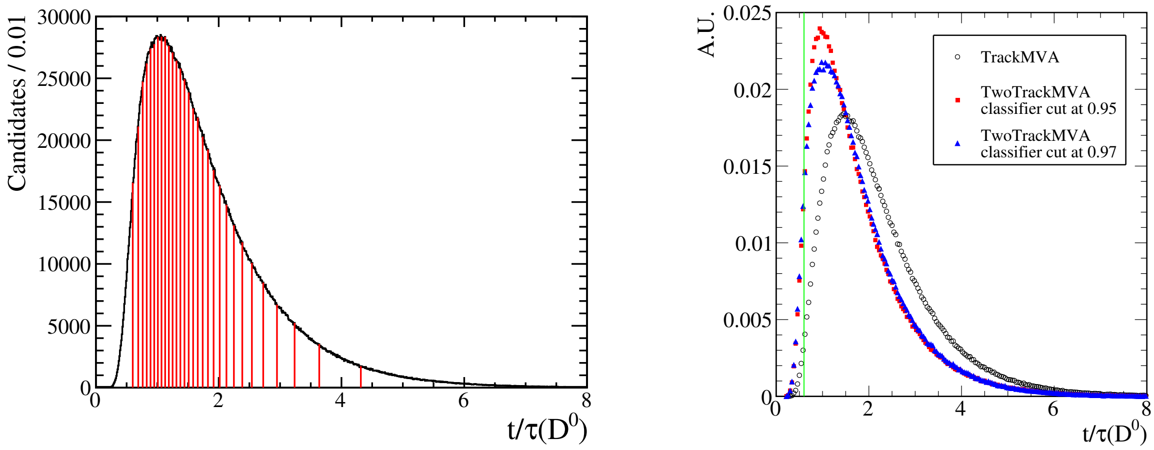

Figure 5.1: Distribution of the D^0 decay time for the whole sample and division in time bins (left) and normalised distributions, separately for each HLT 1 line (right). The vertical green line represents the lower cut on the decay time ($0.6\tau(D^0)$; upper cut at $8\tau(D^0)$).

where no physical asymmetries are present, but a further term appears with respect to Eq. (5.1), as the final state $K^-\pi^+$ is not *CP*-symmetric and positive and negative kaons are characterised by different detection efficiencies. However, this last term is expected to be much smaller than $A_{\rm D}^{\pi_s}(t)$, and can be safely neglected within the current sensitivity.[1] If this is the case, the value of $A_{\rm raw}^{K\pi}(t)$ is exactly equal to the undesired terms of Eq. (5.1). Therefore, if the measurement of $A_\Gamma^{K\pi}$ through a linear fit to the asymmetry after the correction procedure turns out to be compatible with zero within the statistical uncertainty, the correction procedure can be safely used to measure the physical A_Γ on the $D^0 \to K^+K^-$ and $D^0 \to \pi^+\pi^-$ samples.

For all three samples, $D^0 \to h^+h^-$ with $h^+h^- = K^-\pi^+$, K^+K^- or $\pi^+\pi^-$, the asymmetry is modelled, both before ($A_{\rm raw}$) and after the correction ($A_{\rm corr}$), through

$$A^{h^+h^-}(t) = A_0^{h^+h^-} - A_\Gamma^{h^+h^-} \cdot \frac{t}{\tau_{D^0}},$$

where $A_\Gamma^{h^+h^-}$ is expected to be null after the correction for the $K^-\pi^+$ decay mode, and to be equal to A_Γ in the other two decay channels. $A_\Gamma^{h^+h^-}$ is measured through a linear fit of the asymmetry. A binned maximum likelihood fit is preferred with respect to an unbinned one, as it greatly reduces the computational power needed to perform the fit, without significant loss of precision. The whole sample is split into 30 bins of proper decay time in the range $[0.6, 8]\tau(D^0)$; the sizes of the bins are different from each other and are chosen so that each bin contains nearly the same number of decay candidates. This choice implies that every bin weights about the same amount in the fit, and allows an easy visualisation and interpretation of the results of the fit.[2] The number of bins and their ranges are chosen as described in Appendix A; the decay time distribution for the whole sample is shown in Fig. 5.1, together with the normalised distributions by HLT1 line. In particular, the `TrackMVA` line is enriched with high decay times with respect to the `TwoTrackMVA` lines. The raw asymmetry in the $i^{\rm th}$ decay time bin is calculated as

$$A_{\rm raw}^{h^+h^-}(t_i) = \frac{N^+(t_i) - N^-(t_i)}{N^+(t_i) + N^-(t_i)},$$

where $N^+(t_i)$ and $N^-(t_i)$ are the number of reconstructed $D^0(t)$ and $\overline{D}^0(t)$ decays into final state h^+h^- in the $i^{\rm th}$ bin of decay time, and the centre of the bin t_i is calculated as the average

[1] This approximation is further discussed at the end of this chapter.

[2] As the distribution of the decay time is exponential, if bins of equal width were employed, the bins related to highest time would have larger and larger errors.

decay time of all the $N^+(t_i)$ and $N^-(t_i)$ decays. This choice ensures that no bias is introduced on the A_Γ measurement owing to the binning procedure when fitting the asymmetry with a linear model.

Only the results from the $D^0 \to K^-\pi^+$ decays are displayed in the following, in order to study the correction and its precision before applying it to the $D^0 \to K^+K^-$ and $D^0 \to \pi^+\pi^-$ samples. This is done in order not to bias the decisions on the details of the analysis procedure by looking at the $D^0 \to K^+K^-$ and the $D^0 \to \pi^+\pi^-$ data. Only once the reliability of the whole analysis method is demonstrated, the analysis is applied to the $D^0 \to K^+K^-$ and $D^0 \to \pi^+\pi^-$ decay modes (see Chap. 7). The following studies are performed separately for different HLT1 lines, as their selection requirements are substantially different, introduce different correlations among the kinematic quantities and, therefore, also different detector-induced time-dependent asymmetries. As an example of the fit to the raw asymmetry, the results for the $D^0 \to K^-\pi^+$ decays and the `TrackMVA` line for the four subsamples $\{2015,\ 2016\} \times \{$*MagUp*, *MagDown*$\}$ are displayed in red in Fig. 5.7; the values of $A_\Gamma^{K\pi}$ and the averages for each HLT1 line are displayed in Fig. 5.8. In the last figure, the values of $A_\Gamma^{K\pi}$ in the different subsamples turn out to be incompatible with each other, their values being incompatible with zero up to 7σ for the `TrackMVA`, 2016 *MagUp* sample, demonstrating the need for a correction procedure to eliminate the detector-induced time-dependent asymmetries, as in the Run 1 measurement [4]. Their origin is described in detail in the next section, the following one being devoted to the description of the correction procedure.

5.2 Production mechanism

The detector-induced, time-dependent asymmetries that enter the raw asymmetry of Eq. (5.1) are caused by the interplay of three factors:

1. the correlation between the proper decay time and the momentum of the D^0 that is induced by the trigger and offline selection requirements;

2. the presence of significant charge asymmetries in the momentum distribution of the π_s^+, caused by the different acceptance and detection efficiency for particles of opposite charge;

3. the strong correlation between the momentum of the D^0 and that of the π_s^+, provoked by the low Q-value ($\approx 6\,\text{MeV}/c^2$) of the $D^{*+} \to D^0\pi^+$ decay.

All three factors are indispensable in order to produce these undesired time-dependent asymmetries, and they are separately described in the next subsections.

5.2.1 Correlation between the D^0 proper decay time and momentum

The decay time of the D^0 is measured at LHCb as

$$t = \frac{d}{c\beta\gamma} = d \cdot \frac{m}{p}, \tag{5.2}$$

where all quantities are referred to the D^0, d is the displacement between the PV and its decay vertex, β its velocity in natural units, γ its relativistic factor, m its invariant mass and p the magnitude of its momentum. In the absence of detection effects, the decay time of the D^0 is independent of its momentum. However, the selection requirements of the trigger and of the offline selection on the kinematics of the decay introduce correlations between these two quantities. In particular, the trigger asks the D^0 displacement from the PV, as well as other displacement-related quantities such as the impact parameter (IP) of the D^0 daughter particles,

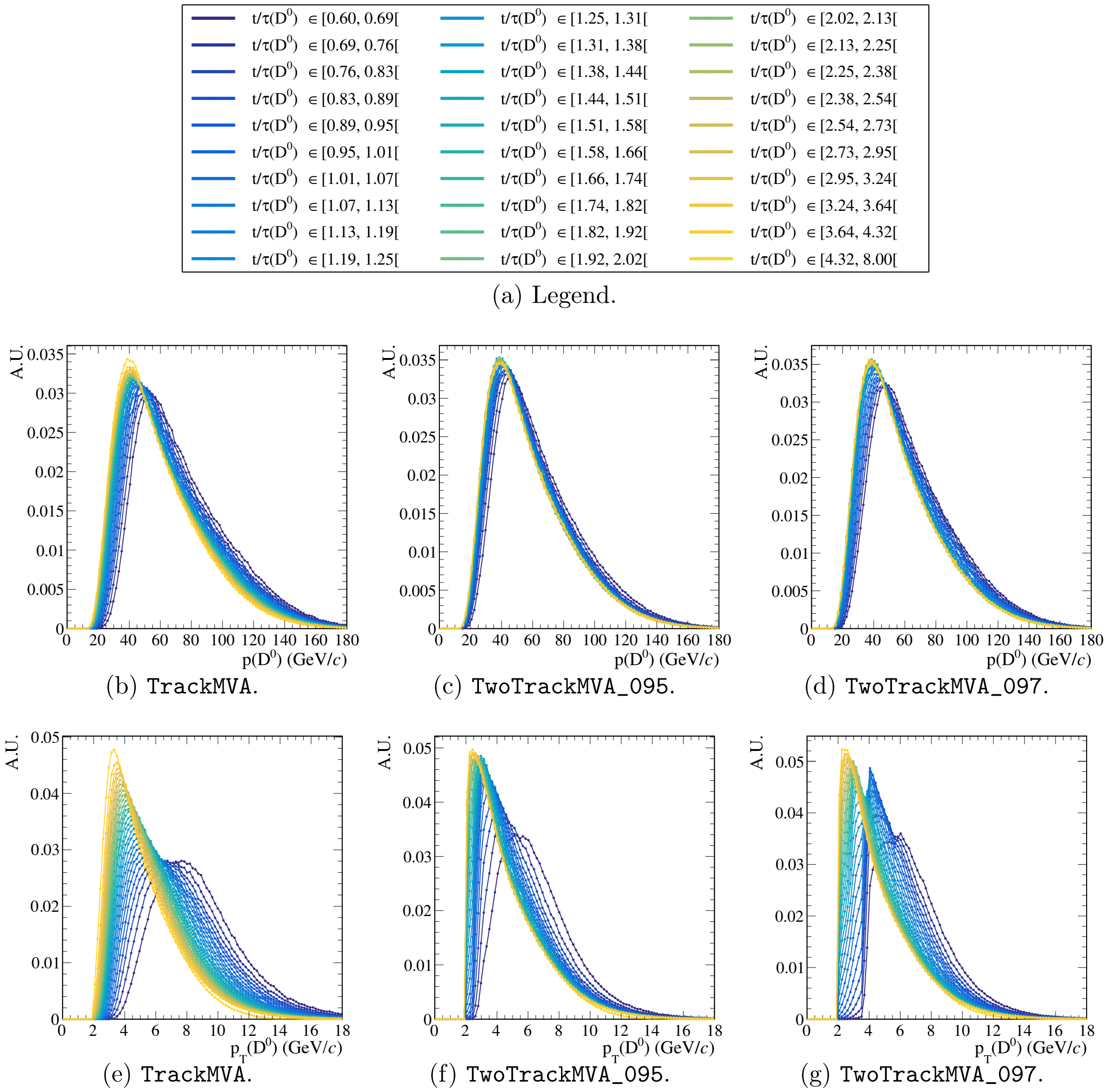

Figure 5.2: $p(D^0)$ and $p_{\mathrm{T}}(D^0)$ distributions, in a different colour for every decay time bin, separately for each HLT 1 line.

to be higher than a threshold, in order to distinguish the decays of interest from the overwhelming background of particles produced in the PV. The lower cut-off on the distribution of d translates in the fact that low decay times can be measured only if the momentum of the D^0 is high enough (see Eq. (5.2)). This is shown in the top line of figures of Fig. 5.2, where the distributions of the momentum of the D^0 are drawn with different colours for each bin of decay time. The lower the time (colours tending to blue), the higher the mean momentum of the distribution.

For primary decays the displacement vector is proportional to the momentum, $\vec{\mathbf{d}} = (\vec{\mathbf{p}}/m)t$, so that a requirement on the D^0 flight distance $|\vec{\mathbf{d}}|$ (or on the IP of the D^0 daughters) is expected to induce similar correlations between the D^0 decay time and the three components of its momentum, *i.e.* the ratio of the shift between the momentum distributions at different decay times to their typical width is expected to be the same for all three directions x, y and z. However, the trigger requirements of the LHCb experiment are not directly on the D^0 flight distance and tracks IPs, but rather on χ^2_{FD} and χ^2_{IP} observables, that include the information of the relative uncertainties.

Since the accuracy of the measurement of the position of vertices, and hence also of the flight distance and the IPs, is typically much better in the plane transverse to the beam (x–y plane) than that in the longitudinal direction z,[3] the cuts on the χ^2_{FD} and the χ^2_{IP} are more selective in the transverse plane than in the longitudinal direction. As a consequence, the correlation between the D^0 decay time and its transverse momentum (bottom line of figures of Fig. 5.2) is much larger than the correlation with its momentum.

As can be clearly seen, the momentum distributions as a function of the decay time show different behaviours for different HLT1 lines. In particular, the `TrackMVA` line shows the largest shift among the distributions, owing to the very tight requirement on the χ^2_{IP} of the track that fired the trigger. This can be seen in Fig. 4.1, where the lower cut on the χ^2_{IP} of the trigger track is larger than 10 for typical reconstructed transverse momenta of $p_{\mathrm{T}} < 15\,\mathrm{GeV}/c$. On the contrary, for the `TwoTrackMVA_095` and `TwoTrackMVA_097` lines, the requirement on the χ^2_{IP} observables of the pair of tracks that fired the trigger is looser ($\chi^2_{\mathrm{IP}} > 4$), as the early reconstruction of the D^0 decay vertex, performed during the HLT1 stage, results into an increased ability to discriminate the D^0 decays from the background of tracks originating in the PV. Therefore, the average χ^2_{FD}—and also the average displacement—of the candidates that fired the `TwoTrackMVA_095` and `TwoTrackMVA_097` lines is lower than that of `TrackMVA` candidates (Fig. 4.2), and consequently low decay times can correspond to lower reconstructed momenta. The correlation between the D^0 decay time and momentum is therefore lesser than in the `TrackMVA` case. However, an evident discontinuity in the distributions of the transverse momentum for different times arises for both the `TwoTrackMVA_095` and `TwoTrackMVA_097` lines (Fig. 5.2(f) and 5.2(g)). This is due to the rectangular cuts that are implemented by the classifier of the HLT1 two-track line (Fig. 4.2), that have a significant impact on the correlations—the effect is more visible for the `TwoTrackMVA_097` line because of its tighter rectangular cuts—. In fact, the sum of the transverse momenta of the two decay particles, $p_{\mathrm{T}}(h^+) + p_{\mathrm{T}}(h^-)$, is nearly equal to $p_{\mathrm{T}}(D^0)$, whereas the χ^2_{FD} is somewhat proportional to the decay time. As a consequence, the rectangular cut $\{p_{\mathrm{T}}(h^+)+p_{\mathrm{T}}(h^-) > 4\,\mathrm{GeV}/c\} \vee \{\chi^2_{\mathrm{FD}} > 125\}$ reflects in the distributions of low times showing a cut at about $p_{\mathrm{T}}(D^0) = 4\,\mathrm{GeV}/c$.

5.2.2 Momentum-dependent detection charge asymmetries

Notwithstanding the D^0 decay final state h^+h^- is neutral and is not expected to be affected by detection charge asymmetries between D^0 and $\overline{D}{}^0$ decays,[4] the slow π^+_{s} that is used to infer its flavour is characterised by large, momentum-dependent charge asymmetries. The most evident cause of these asymmetries is given by the presence of the vertical magnetic field between the TT tracker and T-stations. Even if they have equal momenta, slow pions of opposite charge are bended in opposite directions by the magnet (Fig. 5.3(a)), and it is possible that one exits the acceptance of the LHCb detector before passing through the T-stations, whereas the other does not. This effect can be nearly completely corrected taking advantage of the symmetry of the LHCb detector with respect to the vertical y–z plane,[5] by reversing the sign of the x-component of the momentum of negative pions, *i.e.* multiplying $p_x(\pi_{\mathrm{s}})$ by the sign q_{s} of the charge of the slow pion (Fig. 5.3(b)).

It is useful to visualise the distributions of the momenta of the slow pions using a coordinate system that is more natural than the Cartesian components of the momentum as far as the

[3] This is a consequence of the fact that the angular acceptance of the LHCb experiment is very low, $\theta \lesssim 250\,\mathrm{mrad}$, causing most reconstructed tracks to have small angles among each other.

[4] The asymmetries between the $D^0 \to K^-\pi^+$ and $\overline{D}{}^0 \to K^+\pi^-$ decays that are due to the different cross sections with matter of K^+ and K^- can be safely neglected at the current level of precision.

[5] The LHCb detector employs a right-handed coordinate system centred in the nominal pp interaction point, with the x axis pointing towards the centre of the LHC ring, the y axis pointing upwards and the z axis pointing along the beam, in the direction of the downstream subdetectors.

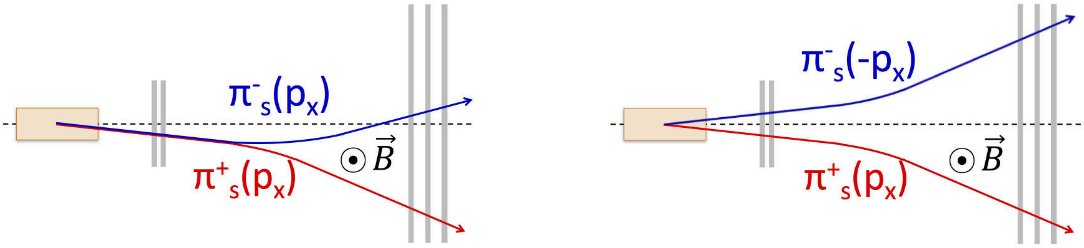

(a) π_s^+ and π_s^- with equal momenta.

(b) π_s^+ and π_s^- with equal momenta, except for the sign of p_x, that is reversed for the π_s^-.

Figure 5.3: Graphical representation of the bending through the magnet of two π_s with opposite charge. The red rectangle represents the VELO, the two vertical lines represent the two layers of the TT and the rightmost lines represent the three layers of the T-stations; the magnetic field is placed between the last two detectors. Even if the momenta of the two pions are equal (left figure), they are bended in opposite directions, one of them possibly exiting the LHCb acceptance.

acceptance is concerned, parametrising $\vec{\mathbf{p}} = (p_x, p_y, p_z)$ in terms of the three following kinematic variables

$$q_s \cdot \theta_x = q_s \cdot \arctan\left(\frac{p_x}{p_z}\right), \qquad \theta_y = \arctan\left(\frac{p_y}{p_z}\right), \qquad k = \frac{1}{\sqrt{p_x^2 + p_z^2}}, \tag{5.3}$$

where θ_x and θ_y parametrise the emission angle of the momentum at production of the π_s, and k is proportional to the curvature of the π_s in the x–z plane. The angles θ_x and θ_y define the π_s trajectory before entering the dipole magnetic field, whereas k quantifies its deflection when passing through the magnet. The distributions of the momentum of the slow pions in this coordinate system and the asymmetry between the π_s^+ and π_s^- distributions are reported for the *MagUp* polarity in Fig. 5.4. The effect of the magnetic field is shown in Fig.5.4(a), where negative $q_s \cdot \theta_x$ are measured only if the momentum of the π_s is high enough—*i.e.*, the curvature is low enough—, otherwise the particle is bended outside the LHCb acceptance. A further, more complex acceptance effect is visible in Fig. 5.4(c), where the number of events with positive $q_s \cdot \theta_x$ is suppressed for $\theta_y \approx 0$. This is because the slow pions that are produced in this region, being bended by the magnet towards lower values of $q_s \cdot \theta_x$, are likely to intersect the T-stations layers in the region corresponding to the beam pipe, that is not instrumented, so that they are not detected as *long tracks* by LHCb.

As can be seen in Fig. 5.4(b) and 5.4(d) statistically significant asymmetries between the π_s^+ and the π_s^- momentum distributions, of order of few per cent, are present also if the sign of the x-component of the momentum of negative pions is reversed. Asymmetries as large as 10% can be spotted in low acceptance regions, both near the beam pipe ($\theta_x \approx \theta_y \approx 0$) and near the borders of the distributions. However, they are not the only asymmetries that affect the measurement of A_Γ and, even when they are excluded from the data sample, high values of $A_\Gamma^{K\pi}$ are obtained. In fact, also in the central and more populated regions of the distributions residual asymmetries of the order of the per cent survive. They are likely due to a combination of various factors, including:

- misalignments between the LHCb detector and the beam pipe, resulting in slight acceptance differences in the $x > 0$ and $x < 0$ regions that are not corrected by reversing the sign of θ_x for the π_s^-;
- slight asymmetries of the LHCb experiment—caused by both geometrical imperfections or different detection efficiencies for different components of the detector—with respect to the y–z plane;

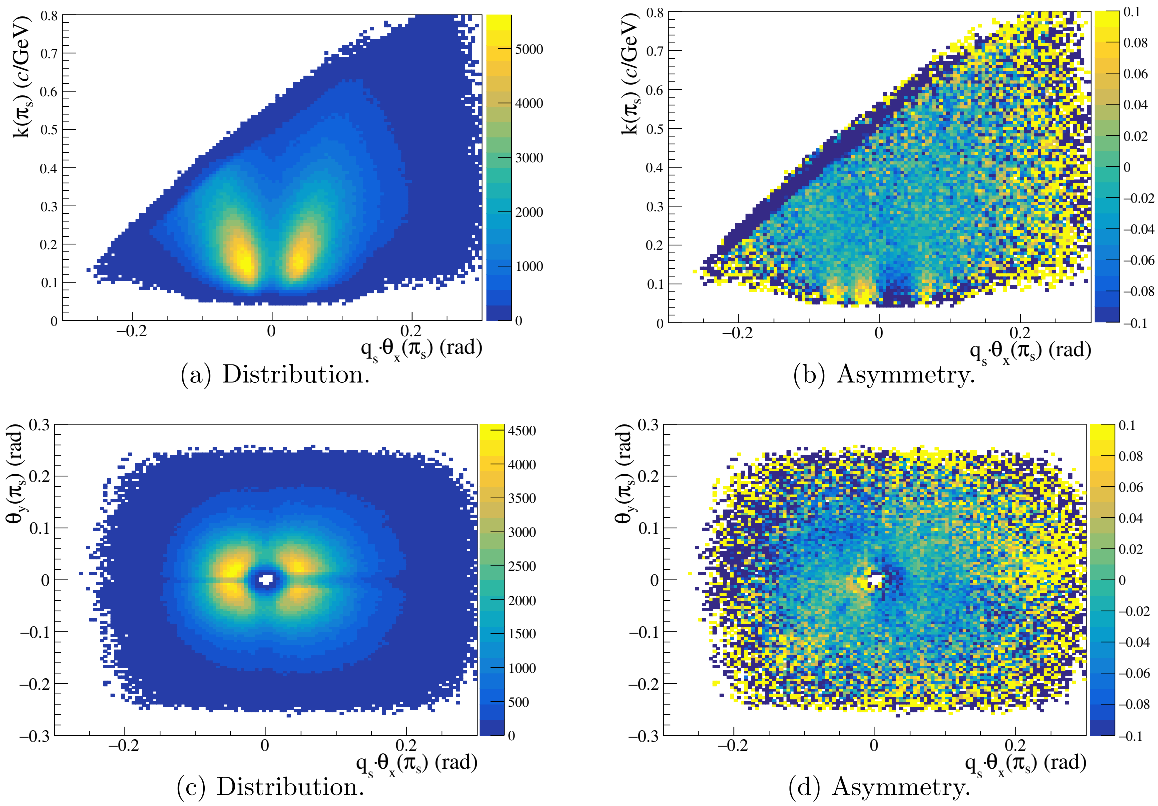

(a) Distribution. (b) Asymmetry.

(c) Distribution. (d) Asymmetry.

Figure 5.4: Distribution (left) and asymmetry (right) of the momentum of the slow pion, parametrised in terms of θ_x, θ_y and k, for the 2016 *MagUp* data sample. The sign of θ_x is reversed for negative pions, *i.e.* θ_x is multiplied by the charge q_s of the slow pion, in order to cancel the main acceptance asymmetries.

- inhomogeneities of the magnetic field that are not symmetric with respect to the y–z vertical plane passing through the beam pipe;
- momentum-dependent production asymmetries between the D^{*+} and D^{*-} mesons, that reflect in a momentum-dependent asymmetry of the distributions of the π_s.

These detector asymmetries are expected to change over time, due to changes in the run conditions of the experiment, and with the magnet polarity.[6] In particular, they are known to be much lower for the *MagDown* polarity with respect to the *MagUp* one, and they do not necessarily cancel completely averaging the distributions between the two polarities.[7] Therefore, the division of the sample according to the magnet polarity is used in order to check that the measurement of A_Γ is consistent independently of the entity and characteristics of the asymmetries, rather than to reduce the asymmetries by averaging the results obtained with *MagUp* and *MagDown* polarities.

As far as the measurement of A_Γ is concerned, since the strongest correlations that have been shown in the previous section are relative to the transverse momentum, the most important asymmetry is the asymmetry between the transverse momentum distributions of the π_s, displayed in Fig. 5.5. The asymmetry shows an overall variation of about 2% over the momentum range, increasing smoothly from low to high momenta, for the *MagUp* sample, whereas, as previously anticipated, is much lower for the *MagDown* sample.

[6] *Inter alia*, the size and the position of collision region between the bunches of protons is known to change between the *MagUp* and *MagDown* polarities.

[7] It is meant that the sign of θ_x is additionally reversed for *MagDown* polarity, in addition to the multiplication by q_s.

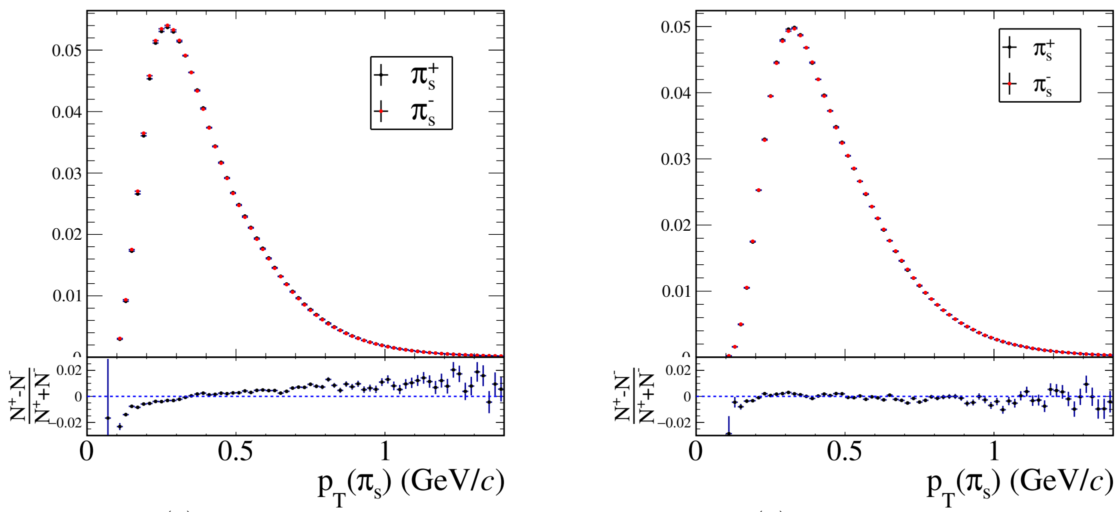

(a) 2016 *MagUp*. (b) 2016 *MagDown*.

Figure 5.5: Normalised distributions of the transverse momentum of positive and negative slow pions and their relative asymmetry.

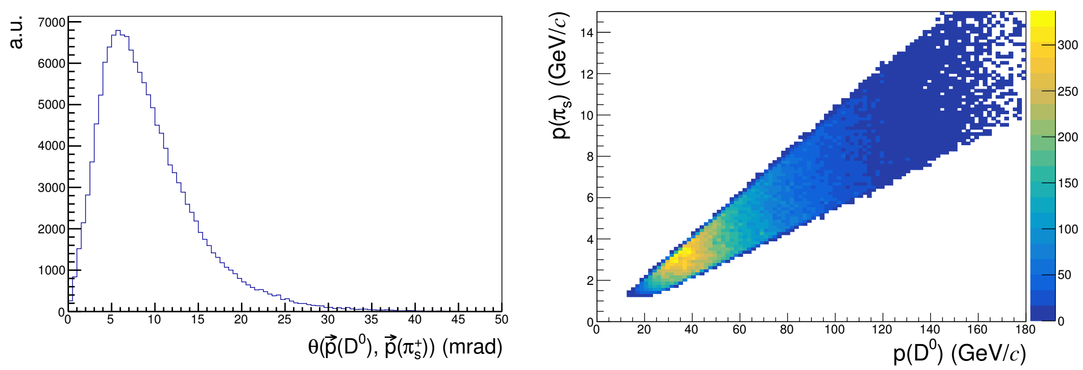

Figure 5.6: Correlation between the momenta of the D^0 and of the π_s^+: angle between the momenta of the D^0 and of the π_s^+ (left), and distribution of the candidates in the $p(D^0)$–$p(\pi_s)$ plane.

5.2.3 Correlation between the kinematics of the D^0 and of the π_s

The correlations between the D^0 decay time and momentum and the momentum-dependent charge asymmetries of the distributions of the slow pions alone would not be able to explain the appearance of time-dependent charge asymmetries. However, the momenta of the D^0 and of the π_s are strongly correlated, owing to the low Q-value of the $D^{*+} \to D^0\pi^+$ decay ($\approx 6\,\mathrm{MeV}/c^2$), that is much lower than the π^+ mass ($\approx 140\,\mathrm{MeV}/c^2$). Therefore, the D^0 and the π_s^+ are produced nearly at rest in the D^{*+} rest frame, and their momenta result to be nearly parallel in the laboratory frame, the angle between them being lesser than 1° on average, and their size being also highly correlated (Fig. 5.6).

In light of the above, the origin of the time-dependent charge asymmetries can be clearly identified. As an example, let us consider the evident time-dependent asymmetries of the raw data of Fig. 5.7(c) (red points, 2016 *MagUp* subsample). As seen in Fig. 5.5(a), the charge asymmetry between the number of D^{*+} and D^{*-} reconstructed decays increases as a function of the momentum of the slow pion. Since this momentum is highly correlated to that of the D^0, the charge asymmetry increases as a function of the D^0 momentum, too. Finally, as the average momentum of decay candidates at high decay times is lower than that of candidates at low decay times (Fig. 5.2(e)), the detection asymmetry is expected to decrease as a function of the decay time, mimicking the presence of an $A_{\Gamma}^{K\pi}$ different from zero.

At this point, the different sizes of the detector-induced, time-dependent charge asymmetries of Fig. 5.8 for different HLT1 lines and magnet polarities can be also understood. In particular, they are larger for the *MagUp* polarity than for the *MagDown* one as the detection asymmetries are larger in the former case (Fig. 5.5), and they are larger for the `TrackMVA` and `TwoTrackMVA_097` lines than for `TwoTrackMVA_095` because in the first two cases the dependence of the transverse momentum distribution of the D^0 on its decay time is much larger than in the last one.

5.3 Correction procedure

Having highlighted the origin of the detector-induced, time-dependent charge asymmetries, it is now possible to develop a correction procedure to cancel their influence on the A_Γ measurement. As explained in the previous section, the presence of these asymmetries is due to the cooperation of three essential ingredients: the correlations between the D^0 decay time and momentum, the presence of charge asymmetries in the distribution of the π_{s} momentum and the strong correlation between the D^0 and π_{s} momenta. All three factors are essential for their presence; therefore, in order to eliminate them from the data sample, it suffices to remove one of the three factors. As the correlation between the D^0 and π_{s} momentum is unavoidable, two strategies can be followed:

1. remove the correlation between the proper decay time and momentum of the D^0, by reweighing in each bin of decay time the momentum distribution of the D^0 to a reference one;
2. eliminate the charge asymmetries of the π_{s} distribution, reweighing the π_{s}^+ and π_{s}^- time-integrated momentum distributions so that they eventually coincide.

Both methods have been tried; the second was finally chosen since it allows a lower decrease of statistical precision. In fact, the momentum distribution of the D^0 shifts significantly as a function of decay time, especially for the `TrackMVA` line (Fig. 5.2(e)). Since the reference momentum distribution for the reweighing must have a non-null overlap with all the decay time bins, this procedure requires to discard a large fraction of the events, corresponding to the lower tails of the distributions at high decay time, and to the upper tails of the distributions at low decay times.

The equalisation of the π_{s}^+ and π_{s}^- distributions has been performed with a binned procedure in the three-dimensional space $(q_{\mathrm{s}} \cdot \theta_x, \theta_y, k)$ of the soft pion, reweighing the number of D^{*+} and D^{*-} reconstructed decays in each bin so that the number of D^{*+}, $N^+(\theta_x, \theta_y, k)$, be equal to that of D^{*-} with the sign of θ_x flipped, $N^-(-\theta_x, \theta_y, k)$.[8] It has been shown that reweighing the number of D^{*+} to that of D^{*-} decays (or *vice versa*) can introduce a significant bias in the final asymmetry [30]. Therefore, the number of candidates are reweighted to the geometrical mean of the D^{*+} and D^{*-} events, $\sqrt{N^+(\theta_x, \theta_y, k) \cdot N^-(-\theta_x, \theta_y, k)}$, assigning every event with momentum (θ_x, θ_y, k) a weight that is equal to:

- $\sqrt{\frac{N^-(-\theta_x,\theta_y,k)}{N^+(\theta_x,\theta_y,k)}}$, if the decay is a D^{*+};
- $\sqrt{\frac{N^+(-\theta_x,\theta_y,k)}{N^-(\theta_x,\theta_y,k)}}$, if the decay is a D^{*-}.

Different parametrisations of the momentum have been tried, being found to perform equivalently or slightly worse than this one. The same holds also for the case in which the candidates are

[8] In this way, the symmetry of the detector under the transformation $x \to -x$, $q_{\mathrm{s}} \to -q_{\mathrm{s}}$ is employed, so that most weights are ≈ 1.

reweighted to the arithmetic and not the geometric mean. The binning scheme has been chosen according to the studies that have been performed in Run 1 (55 bins in the range $[-0.3, 0.3]$ rad for θ_x, 11 bins in the range $[-0.3, 0.3]$ rad for θ_y and 50 bins in the range $[0., 0.8]c/\text{GeV}$ for k). It was verified that finer binning schemes did not improve the correction precision.

A direct consequence of the equalisation procedure is that the whole, time-integrated asymmetry between the number of reconstructed D^{*+} and D^{*-} is cancelled by construction. However, it has been shown with simulation studies that it does not affect the measurement of a time-dependent *CP* violation effect, like that due to the presence of an A_Γ different from zero. This is done through the following steps:

1. $A_\Gamma^{K\pi}$ is measured after the application of the correction procedure to the data;
2. the raw data sample that was used for the previous measurement is filtered according to an efficiency function that increases linearly with decay time,
$$\epsilon_\pm \propto \frac{1 \pm A_\Gamma^{\text{art}} \cdot t/\tau(D^0)}{2},$$
with opposite signs for positive and negative D^*. In this way, an artificial value of $A_\Gamma^{K\pi}$, A_Γ^{art}, completely indistinguishable from a real *CP*-violating time-dependent asymmetry, is injected in the data;
3. the measurement of $A_\Gamma^{K\pi}$ is repeated following the same method as at point 1 but using the modified data sample, that is characterised by exactly the same correlations and detection asymmetries as the original one, but presents an additional artificial time-dependent asymmetry, A_Γ^{art}, that mimics the presence in the data of a *CP*-violating time-dependent asymmetry (of course, the weighting coefficients are calculated consistently from this modified data sample).

The correction procedure does not bias the measurement of a real *CP*-violating, time-dependent asymmetry if and only if the difference between the fitted values of $A_\Gamma^{K\pi}$ at point 3 and 1 is equal to A_Γ^{art}. It is found by injecting in the data values of A_Γ^{art} as large as 20 times the statistical resolution of the $D^0 \to K^-\pi^+$ decay mode, that the dilution of the value of the measured A_Γ^{art} due to the correction procedure is smaller than 5% of its value.[9] Since the relative dilution is expected to be independent of the value of A_Γ, and A_Γ is currently compatible with zero within a precision of $3 \cdot 10^{-4}$, the bias of the correction procedure on the measurement of A_Γ is expected to be $< 5\% \cdot 3 \cdot 10^{-4}$, and is completely negligible within the current experimental sensitivity.

5.4 Results for the $D^0 \to K^-\pi^+$ sample and final HLT1 configuration

As an example of the effect of the correction procedure on the measurement of A_Γ, the linear fits to the time-dependent asymmetries for all the four subsamples, $\{2015,\ 2016\} \times \{\textit{MagUp},\ \textit{MagDown}\}$, are displayed in Fig. 5.7 for the `TrackMVA` line. The raw asymmetry is drawn in red and the corrected asymmetry, after the reweighing of the events to equalise the π_s distributions, in black. The obtained values of A_Γ and their averages over the four subsamples are shown, for all three HLT1 lines, in Fig. 5.8. For each HLT1 line, the results from the raw asymmetry are not compatible with each other (see the χ^2/ndf of the average, in red, of Fig. 5.8), nor with zero, with a significance that can be as large as 7σ (`TrackMVA` line, 2016 *MagUp*). As anticipated, the average between the *MagUp* and the *MagDown* data samples does not solve the problem, as also the three averages of the raw A_Γ are incompatible with zero at the level of about 5σ for

[9] This value is chosen to be much larger than the current statistical uncertainty in order to be sensitive to possible dilution effects; if A_Γ was equal to zero, no dilution effects might be detectable.

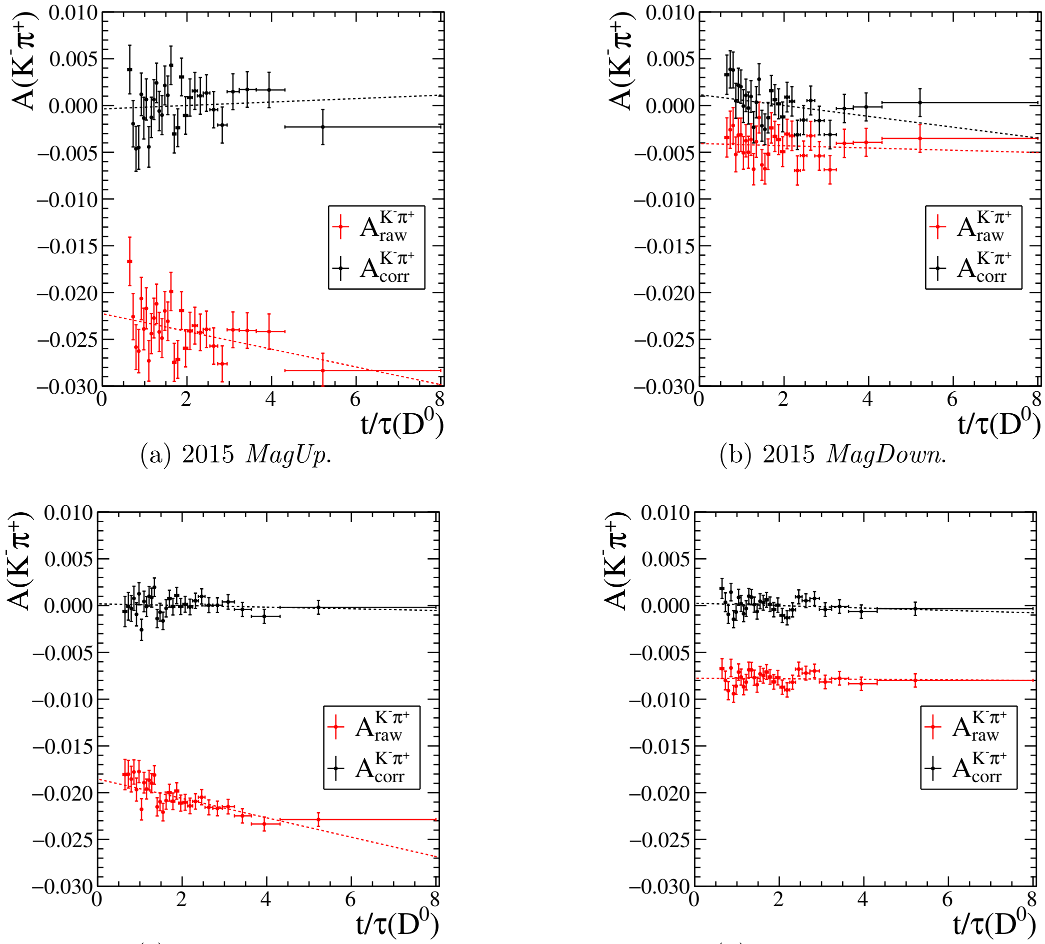

(a) 2015 *MagUp*.

(b) 2015 *MagDown*.

(c) 2016 *MagUp*.

(d) 2016 *MagDown*.

Figure 5.7: Linear fit to the time-dependent asymmetry for the $D^0 \to K^-\pi^+$ decays, for the `TrackMVA` HLT 1 line.

the `TrackMVA` and the `TwoTrackMVA_097` lines. However, the correction procedure removes these tensions, ensuring the compatibility among the four subsamples and the full compatibility with zero of their averages, with a precision of about $1.0 \cdot 10^{-4}$.

It is difficult to quantify how much the averages of the separate HLT1 lines are in agreement with each other since, even if the overlaps among the three lines are well known (see Fig. 4.3), the precision on the measurement of A_Γ is not simply proportional to $1/\sqrt{N}$. In fact, the measurement of the slope of the time-dependent asymmetry is mainly affected by the first and the last bins of decay time, and the decay time distributions of the three lines are very different (see Fig. 5.1). However, as no undesired behaviours were observed in the three plots of Fig. 5.8, the measurement of A_Γ was repeated using the whole data sample, taking the logic "OR" of the three HLT1 trigger lines. The results are reported in Fig. 5.9. Also in this case, the correction procedure shifts the average of the measurements of $A_\Gamma^{K\pi}$ from a tension larger than 5σ to the full compatibility with zero within 1σ. However, a tension of about 2.5σ is observed between the 2016 *MagUp* and *MagDown* subsamples. Many checks have been performed in order to decide whether this was just a statistical fluctuation or not. In particular, since in Run 1 the measurement was performed using a selection that was very similar to that of `TrackMVA` with no detected problems and no tensions are visible in this sample between the 2016 *MagUp* and *MagDown* subsamples, too, the whole sample has been split between the candidates that fired the `TrackMVA` line and

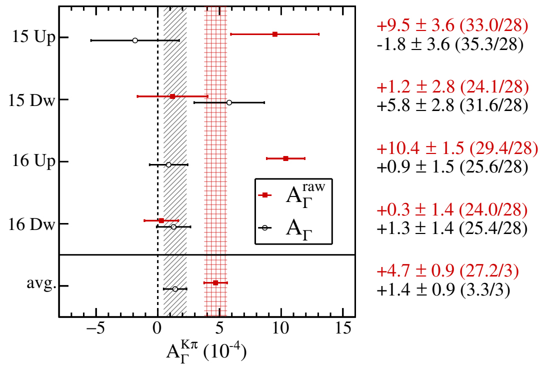

(a) `TrackMVA`.

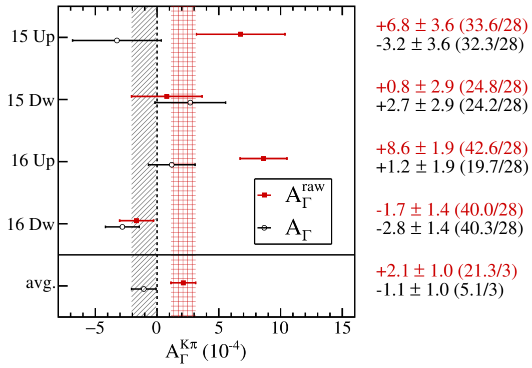

(b) `TwoTrackMVA_095`.

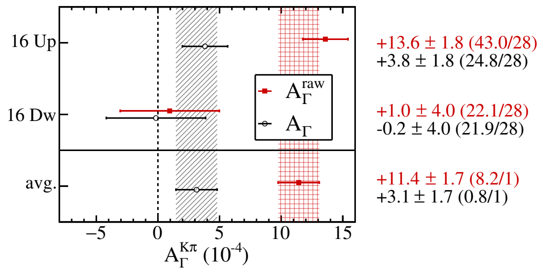

(c) `TwoTrackMVA_097` (no data were taken in 2015 with this trigger configuration).

Figure 5.8: Measurement of $A_\Gamma^{K\pi}$ in the four subsamples, $\{2015,\ 2016\} \times \{\mathit{MagUp},\ \mathit{MagDown}\}$, separately for each HLT 1 line. For every fit, the final value of $A_\Gamma^{K\pi}$ is displayed on the right, as well as its reduced χ^2. Red points correspond to the measurement from the raw asymmetry; black points after the correction procedure of Sect. 5.3. The average over the four subsamples is represented as a hatched region.

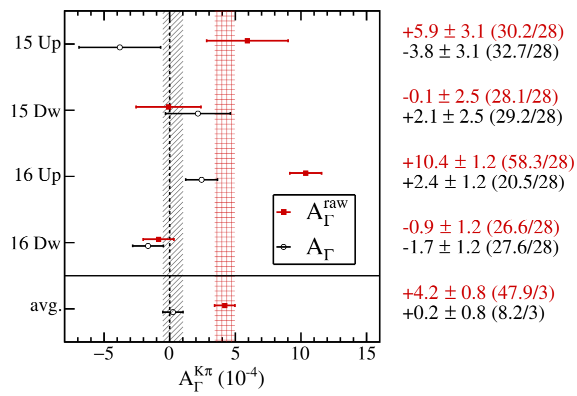

Figure 5.9: Measurement of $A_\Gamma^{K\pi}$, simultaneously for all HLT 1 lines.

the complementary sample, !(`TrackMVA`). Even if this choice highly modifies in an unnatural way the kinematic distributions of the events for the !(`TrackMVA`) sample, it is useful to highlight possible large effects that might be introduced by these additional events, collected thanks to the implementation of the two new `TwoTrackMVA` lines, specifically developed for Run 2 running conditions, in order to take advantage of the features of the new trigger system. The results are reported in the first line of Fig. 5.10. The initial asymmetries for the !(`TrackMVA`) sample are much larger, and the tension between the values of A_Γ for the 2016 *MagUp* and *MagDown* subsamples after the correction is more evident ($\approx 3\sigma$). Then, the attention was further focussed on the asymmetry of the candidates of this sample with $p_T(\pi_s) < 300\,\mathrm{MeV}/c$, that are known

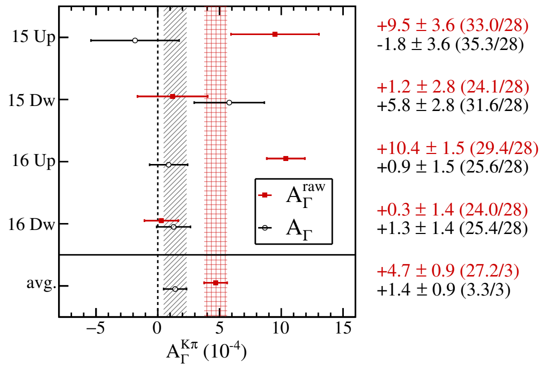

(a) `TrackMVA`.

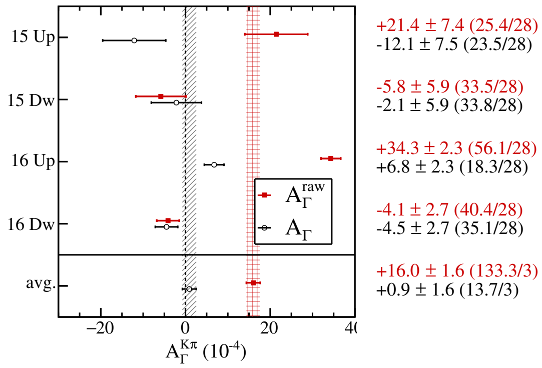

(b) !(`TrackMVA`).

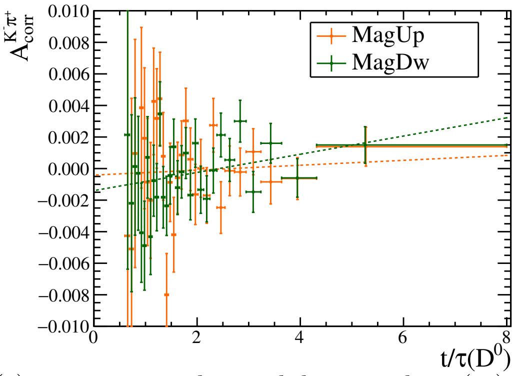

(c) `TrackMVA`; only candidates with $p_{\mathrm{T}}(\pi_s) < 300\,\mathrm{MeV}/c$.

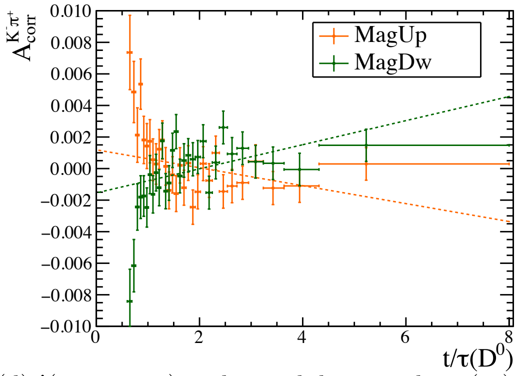

(d) !(`TrackMVA`); only candidates with $p_{\mathrm{T}}(\pi_s) < 300\,\mathrm{MeV}/c$.

Figure 5.10: Measurement of $A_\Gamma^{K\pi}$, separately for the `TrackMVA` HLT 1 line and its negation (note the different scales on the x-axis); below, result of the fits for the 2016 *MagUp* and *MagDown* subsamples, only for candidates with $p_{\mathrm{T}}(\pi_s) < 300\,\mathrm{MeV}/c$.

to be affected by the largest detection asymmetries, as it has been shown for example in [46]. The corrected asymmetries for both the *MagUp* and *MagDown* 2016 subsamples are plotted in the bottom line of Fig. 5.10; non-linear tails, with opposite signs for opposite polarities can be clearly spotted for low decay times, being likely responsible for the tension. This behaviour cannot be easily ascribed to the physics of the D^0 meson decays and is due to some second order effect that is not accurately accounted for by the correction procedure. One possibility may be that the detection asymmetry depends on further variables, in addition to the momentum of the soft pion. However, detailed studies of the asymmetry of the main kinematic variables of the events (in particular, the momentum of the kaon, that is expected to be affected by charge detection asymmetries) did not evidence significant tendencies after the correction procedure. Another well-motivated possibility may be that the multiple hyper-rectangular cuts that are introduced at HLT1 stage by the classifier of the `TwoTrackMVA` lines (see Sect. 4.3.2) may limit the accuracy of the correction procedure in removing the time-dependent asymmetries. In fact, different hyper-rectangular regions are characterised by different time-momentum correlations and, possibly, by different charge detection asymmetries. If that were the case, in order to remove the time-dependent asymmetries it would be necessary to apply the correction procedure separately for each hyper-rectangular region. However, the current number of events is too low to try to implement such a strategy and verify if this is really the case or not.

Therefore, as far as the preliminary Run 2 measurement of A_Γ with the data collected only during 2015–2016 is concerned, notwithstanding that the discrepancies observed between

MagUp and *MagDown* seem to cancel in the average between the results obtained with the two magnet polarities, it was prudently decided to use only the data sample corresponding to the `TrackMVA` line, where possible discrepancies are expected to be absent or undetectable within current experimental sensitivity. As it can be seen from Figs. 5.8 and 5.9, the statistical uncertainty on A_Γ moves from $0.8 \cdot 10^{-3}$ to $0.9 \cdot 10^{-3}$ when the additional events collected with the new `TwoTrackMVA` lines are removed from the whole sample, corresponding to a degradation of the resolution of about 15%, despite the size of the sample being halved.[10] This loss of statistical power is certainly affordable and it has been verified that it is smaller than losses resulting from alternative approaches where tighter momentum requirements are applied (16% for $p_{\mathrm{T}}(\pi_{\mathrm{s}}) > 300\,\mathrm{MeV}/c$ and 20% for $p_{\mathrm{T}}(h^+) + p_{\mathrm{T}}(h^-) > 4\,\mathrm{GeV}/c$), adopted to reduce the observed tensions and to equalise the kinematics of the three HLT1 trigger lines (see Fig. 4.2). The option of discarding for the time being the additional events collected with the new `TwoTrackMVA` trigger lines has also another advantage. In fact, the kinematics of the final data sample has more homogeneous decay time–momentum correlations, and the accuracy of the correction procedure at present seems to be still much more precise than the current statistical uncertainty, allowing not to assess any systematic uncertainty on the procedure.

Once the data collected in 2017 and 2018 will be available and it will be possible to perform the A_Γ measurement on the whole Run 1 + Run 2 data sample, further extensive studies will be performed to pinpoint the origin of these observed correction inaccuracies in the `TwoTrackMVA` lines. The size of the sample will then allow probing any subtle effects and developing a more precise and reliable correction, or a completely new strategy, to keep under control detector-induced, time-dependent charge asymmetries, also in preparation of the future LHC runs where a large increase of the samples size is expected. However, in the meanwhile, the results obtained from the work of this thesis did already impact the trigger strategies in collecting data in 2017 and 2018.

5.5 Towards a new HLT1 trigger line for measurements at still higher precision

The results obtained in this thesis have been presented to the LHCb Trigger Working Group, with a view to the remaining data-taking period of Run 2 (2017–2018) and the future runs at higher luminosity that are foreseen between 2021 and 2029. As it has been shown in the previous sections, the hyper-rectangular cuts that are currently introduced by the two-track line induce undesired, complex correlations between the decay time of the D^0 and the other kinematic variables of the events. However, if the hyper-rectangular cuts were removed, the two-track line would offer several advantages over the single track line. In fact, as it can take advantage of the discriminant power provided by the D^0 vertex reconstruction, the two-track line allows a better purity for the collected sample, and can therefore employ looser cuts than the single track line on the IPs of the particles coming from the decay of the D^0, resulting into lower decay time–momentum correlations. This can be clearly seen by comparing Fig. 5.2(e) for the `TrackMVA` line with Fig. 5.2(f), for the `TwoTrackMVA` line, where the impact of the classifier is limited, at least with respect to Fig. 5.2(g), owing to the lower threshold that is required for the HLT1 two-track classifier. An alternative possibility that has been already implemented in the LHCb trigger during the past few years to avoid complex correlations between the D^0 decay time and the kinematics of the event is given by the so called "lifetime-unbiased" trigger lines,

[10] This is due to the fact that the additional events collected by the two-track HLT1 lines are mainly distributed in a very small region at low decay times, where is concentrated also the larger part of the `TrackMVA` sample. Therefore, they do not further constrain the slope of the asymmetry in a significant way, as do the much rarer events at high decay times.

where no requirements on the impact parameters, the flight distance or other quantities that might bias the decay time distribution are requested, but only on reconstruction quality variables and on the measured lifetime of the D^0 [47, 48]. However, this approach requires even today to prescale the number of events that are collected, by rejecting randomly a predefined fraction of them, as the absence of IP-related requirements implies the collection of a high number of background events, resulting in a poor purity of the final sample that cannot be sustained at the high trigger rates that characterise the $D^0 \to h^+h^-$ decays. Therefore, this approach does not appear to be feasible in the future runs of LHCb, and can be considered only a temporary solution. Nevertheless, it is worth mentioning that under the input of the results of this thesis the prescale factor has been moved from 20%, used during the 2015–2016 data-taking periods, to 50% for the 2017–2018 data-taking, with the aim of performing studies on a sample where the correlation between momentum and proper decay time is almost negligible. As a possible solution, it was also proposed to the Trigger Working Group a new two-track trigger line where the requirement on the classifier output is substituted by simple, independent cuts on the IPs of the tracks coming from the decay of the D^0, on their p_{T} and on the D^0 flight distance. Rate and purity tests are ongoing in order to assess the precise thresholds that would be required by this trigger line; meanwhile, the threshold of the classifier of the two-track line is being kept at 0.95, in order to avoid the strong correlations of Fig. 5.2(g).

Chapter 6

Contamination from b-hadron decays

This chapter addresses the problem of the contamination of the data sample by the secondary decays, that dominated the systematic uncertainty of the Run 1 measurement. A novel approach is presented in order to subtract their contribution to the asymmetry, thus reducing the systematic uncertainty by about a factor of 5. As in the previous chapters, the studies are performed on the Cabibbo-favoured $D^0 \to K^-\pi^+$ sample.

6.1 Contribution to the raw asymmetry from secondary decays

Throughout the discussion of the previous chapter, it was assumed that the data sample was composed exclusively of signal events. However, even if the purity of the data sample is larger than 95%, some residual contaminations from background events are present. In particular, the largest source of residual background is that of secondary decays, where the D^{*+} is not produced in the primary vertex (PV), but rather in the decay of a hadron containing a b quark (see Fig. 6.1). In general, the secondary decays are expected to contribute to the measured raw asymmetry in the following way:

$$\begin{aligned} A_{\text{raw}}(t) &= [1 - f_{\text{sec}}(t)] \cdot A_{\text{prim}}(t) + f_{\text{sec}}(t) \cdot A_{\text{sec}}(t) \\ &= A_{\text{prim}}(t) + f_{\text{sec}}(t) \cdot [A_{\text{sec}}(t) - A_{\text{prim}}(t)] \end{aligned} \tag{6.1}$$

where $f_{\text{sec}}(t) = N_{\text{sec}}(t)/\left[N_{\text{prim}}(t) + N_{\text{sec}}(t)\right]$ is fraction of secondary decays in the data sample, $N_{\text{prim}}(t) = N^+_{\text{prim}}(t) + N^-_{\text{prim}}(t)$ is the sum of the reconstructed D^{*+} and D^{*-} primary decays

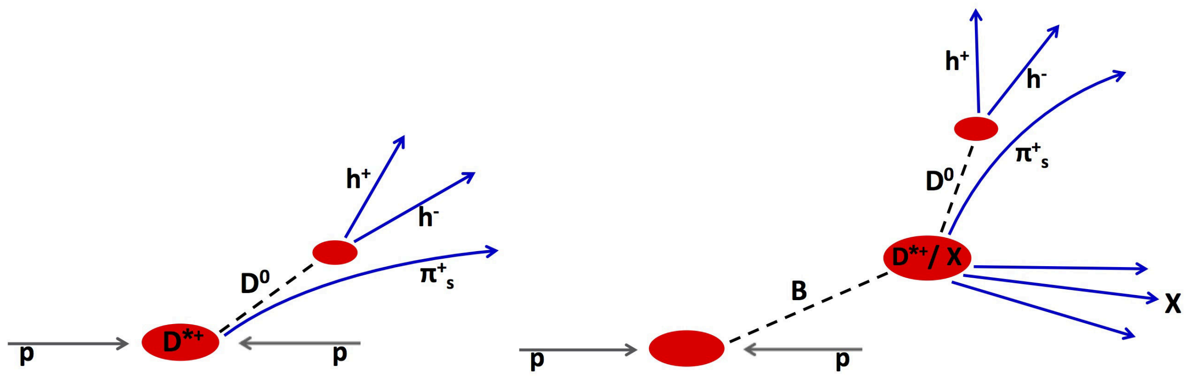

(a) Primary decay.

(b) Secondary decay; X stays for all particles other than the D^{*+} that are produced in the b-hadron decay.

Figure 6.1: Topologies of primary and secondary decays.

at time t, $N_{\rm sec}(t) = N^+_{\rm sec}(t) + N^-_{\rm sec}(t)$ that of secondary decays, and the raw asymmetries of the primary and secondary decays are defined as usual,

$$A_{\rm prim}(t) = \frac{N^+_{\rm prim}(t) - N^-_{\rm prim}(t)}{N^+_{\rm prim}(t) + N^-_{\rm prim}(t)},$$
$$A_{\rm sec}(t) = \frac{N^+_{\rm sec}(t) - N^-_{\rm sec}(t)}{N^+_{\rm sec}(t) + N^-_{\rm sec}(t)}.$$

$A_{\rm sec}(t)$ is expected to be different from $A_{\rm prim}(t)$, mainly because b-hadrons and D^{*+} mesons are characterised by different production asymmetries, but also since the trigger selection can induce different decay time–momentum correlations and different asymmetries in the momentum distribution of the slow pions for primary and secondary decays, because of their different decay topologies. In particular, from Eq. (6.1) it follows that $A_{\rm sec}(t)$ can induce an artificial time-dependency of $A_{\rm raw}(t)$ even if it does not depend explicitly on time, provided that $A_{\rm sec} \neq A_{\rm prim}$, since the fraction of secondary decays depends strongly on the reconstructed decay time. In fact, at LHCb the decay time is measured as

$$t = \frac{d}{c\beta\gamma} = d \cdot \frac{m}{p},$$

where all quantities are referred to the D^0 and d is the displacement between the PV and its decay vertex, *i.e.* the D^0 is supposed to originate from the PV (for further details, see Sect. 4.2 and 5.2.1). However, the D^0 mesons of the secondary decays are not produced in the PV, but in the decay vertex of the b-hadron and, since the average lifetime of the mixture of b-hadrons that are produced at LHC ($\approx 1.57\,$ps [10]) is larger by nearly a factor of 4 than the lifetime of the D^0 meson (0.41 ps), the measurement of the decay time of the secondary D^0 is biased towards higher times. As a consequence, most secondary decays are concentrated at high measured decay times and the fraction of secondary decays increases with the D^0 measured decay time.

In conclusion, the contribution to the raw asymmetry from secondary decays, Eq. (6.1), can mimic the presence in the sample of a real time-dependent asymmetry of the decay rates, even if the asymmetry of the secondary decays does not depend explicitly on the decay time, but is just shifted from that of the primary decays because of their different production asymmetry. In order to subtract it, it is necessary to discriminate the secondary decays from the primary ones. The techniques employed to achieve this purpose are discussed in the next section.

6.2 Discriminating variables

As displayed in Fig. 6.1, while in the primary decays the D^0 is produced in the PV and its momentum points by definition to the PV, in the secondary decays its momentum does not necessarily point in that direction. A direct consequence of this fact is that the measured impact parameter (IP) of the primary D^0 is identically null, within the experimental uncertainty, whereas the IP distribution of the secondary D^0 is broader, with long tails especially for high times. In fact, D^0 secondary candidates with high reconstructed decay time are likely to possess also high flight distances, translating into high IPs as long as the angle between the D^0 and the PV is not exactly null. The three, most used IP-like variables that are used to discriminate primary from secondary decays are, apart from the IP, the $\chi^2_{\rm IP}$ (defined in Sect. 4.2), and the transverse impact parameter TIP, defined as the distance of closest approach of the line of the trajectory of the D^0 from the line parallel to the proton beam and passing through the PV (see Fig. 6.2). If $\vec{p}$ is the momentum of the D^0 and the beam direction is along the z axis, the TIP b can be calculated as

$$b = \frac{\hat{z} \wedge \vec{p}}{|\hat{z} \wedge \vec{p}|} \cdot (\overrightarrow{\rm DV} - \overrightarrow{\rm PV}),$$

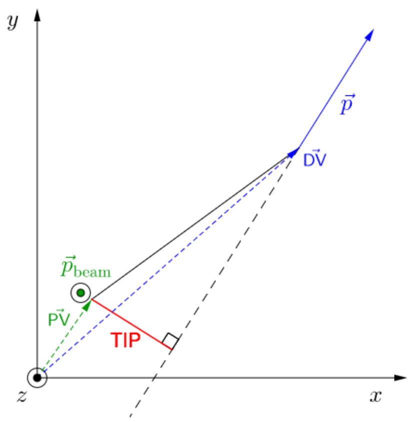

Figure 6.2: Definition of the TIP (projection on the x–y plane).

where $\overrightarrow{\mathrm{DV}}$ is the vector defining the position of the D^0 decay vertex and the sign of the TIP depends on the angle between the projection on the x–y plane of the $(\overrightarrow{\mathrm{DV}} - \overrightarrow{\mathrm{PV}})$ vector and that of the D^0 momentum being positive or negative. The distributions of the IP, the χ^2_{IP} and the TIP of the D^0 in the first, in the middle and in the last bins of decay time for the sample selected according to the procedure described in Chap. 4, but without the cut $\chi^2_{\mathrm{IP}}(D^0) < 9$, are displayed in Fig. 6.3. A non-negligible fraction of secondary decays lies below the distribution of the primary ones, especially at high decay times (corresponding, on average, to high displacements of the D^0), but possibly also at low ones, where the primary and the secondary decays are however nearly indistinguishable. This component contributes to the raw asymmetry, also when requirements on the IP-related variables are requested for the final data sample. Both its size and asymmetry can be precisely evaluated by measuring their values in the well distinguishable tails of the distributions, and then by extrapolating them to the region under the distribution of the primary decays. Of course, this procedure requires a good knowledge of the shapes of the distributions of the observables (IP, χ^2_{IP} or TIP) for both the primary and the secondary decays.

In the LHCb experiment, the standard variable employed to assess the number of secondary decays in the sample is the χ^2_{IP} of the D^0 meson. This observable offers in principle an excellent discrimination between primary and secondary decays at high decay times, since it exploits not only the geometrical information enclosed in the IP observable, but also that related to its uncertainty.[1] Nevertheless, for the same reason that makes it a powerful observable, it is very difficult to accurately know the features of its distribution at the desired level of precision. In fact, owing to the complex correlations among tracking variables and uncertainties, any realistic Geant4-based Monte Carlo simulations would not be reliable with the degree of precision needed for the A_Γ measurement, even if the available computing power allowed generating simulated samples of the same size of the collected ones. As a consequence, in most LHCb analyses the contributions from secondary decays are studied, and then subtracted, with fully data-driven techniques exploiting the discriminant power of the χ^2_{IP} observable. Unfortunately, they are not completely free from approximations and assumptions.

For instance, a standard method used in LHCb (see for example [4, 18, 30]) to disentangle the distribution of the χ^2_{IP} for primary decays is the following. The model of the χ^2_{IP} for primary decays is assumed to be independent of the decay time and it is taken from the first lower time bin, where the relative fraction of secondary decays is assumed to be null.[2] The fraction of secondary decays as a function of the proper decay time is then determined through a fit

[1] This is the reason why the χ^2_{IP} is often referenced as the IP significance.
[2] This assumption is not guaranteed to hold, as it will be shown in the next sections.

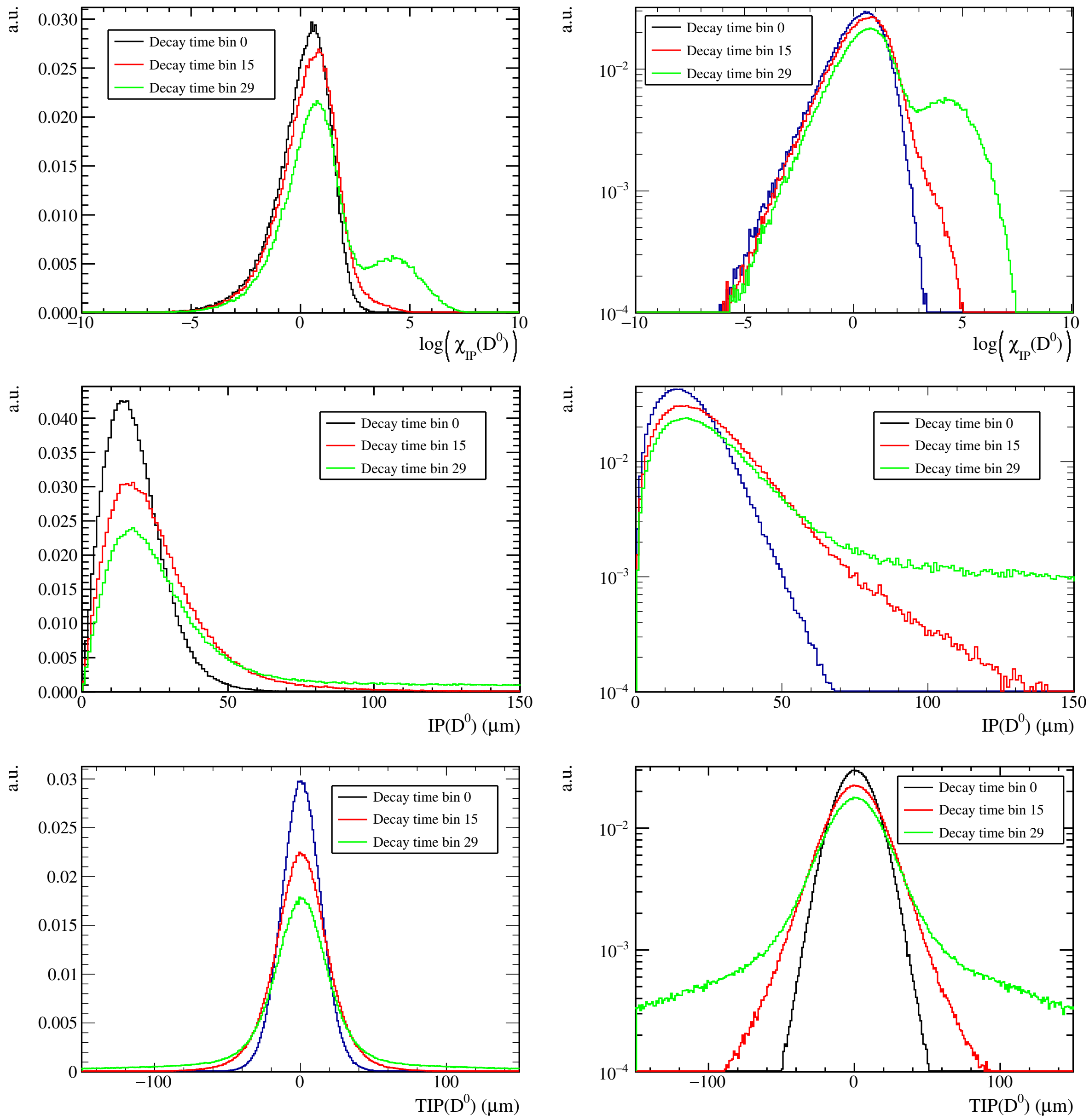

Figure 6.3: Normalised distributions of the $\log(\chi^2_{\rm IP})$ (top), the IP (centre) and the TIP (bottom) of the D^0, in linear and logarithmic scales, for the first, the middle and the last bin of decay time, corresponding to the ranges $[0.6000, 0.8038[$, $[1.9533, 2.0408[$ and $[4.9412, 8.000[$ respectively, in units of D^0 mean lives. The cut $\chi^2_{\rm IP}(D^0) < 9$ is removed by the selection of Chap. 4.

where the $\chi^2_{\rm IP}$ is fixed to the model of the first time bin, while that of secondary decays is parametrised with an empirical function. The systematic uncertainty of this procedure drastically reduces moving to higher time bins, where the contribution of secondary decays can be clearly disentangled. In particular, for decay times larger than $3.5\tau(D^0)$ the extraction of the relative fraction is considered reliable and can be safely used. On the other hand, the asymmetry of secondary decays is determined by reversing the cut on the $\chi^2_{\rm IP}$, selecting for example only the D^0 mesons with $\log[\chi^2_{\rm IP}(D^0)] > 4$, where the component of secondary decays is dominant. The contribution to the asymmetry from secondary decays is then estimated from Eq. (6.1) assuming their asymmetry to be independent of decay time, and extrapolating the fraction of secondary decays to low times through empirical models. This was exactly the strategy followed in the Run 1 measurement of A_Γ [4, 30]. However, the large uncertainties of the models that are used to extrapolate the fraction of secondary decays at low times, along with approximations and assumptions that are implied by the procedure, do not allow a precise subtraction of the asymmetry of secondary decays, resulting in a systematic uncertainty of order $1.0 \cdot 10^{-4}$, that conservatively covers the full size of the bias due to the residual contamination of secondary decays present in the data sample. Even if this approach is satisfactory at the current precision of A_Γ, it will be not for its future measurements.

In order to reduce this systematic uncertainty, it is necessary to subtract precisely the contribution of the secondary decays to the asymmetry, also at low decay times. This procedure cannot be performed looking at the $\chi^2_{\rm IP}$ distributions, as their shape for primary and secondary decays at low decay times is not known with a precision sufficient to discriminate among them, owing to the uncertainties of the Monte Carlo simulations. On the contrary, the distributions of the IP and of the TIP can be obtained with a reasonable degree of accuracy also by means of a simple kinematic simulation of the D^* and $B \to D^* X$ decays (see Appendix B), as they are less sensitive to the correlations among the experimental uncertainties on the tracks and vertices reconstruction. In this thesis, the TIP is preferred notwithstanding its discriminant power is slightly lower than that of the IP, since it does not employ all the information on the positions of the track and of the PV, but only that of their projections on the transverse plane, its empirical modelling is easier than that of the IP. In fact, the distribution of the IP is suppressed near $\mathrm{IP} = 0$ by a phase space Jacobian factor, owing to the fact that it is the distance between a line and a point. The TIP has already been used for the measurement of A_Γ in experiments different from LHCb, but with much lower number of decay candidates [33, 49, 50].

However, in order to reasonably determine the TIP distributions for the primary and secondary decays, it is important to remove from the selection all requirements that might sculpt its distributions for different bins of decay time in a non reproducible way. The idea is to use a simple kinematic simulation (see Appendix B) to infer the main features of the TIP distributions, that should be very simple by construction, in order to determine an empirical model able to disentangle the primary and secondary components with the necessary level of precision for the A_Γ measurement (see Sect. 6.4.1). The other two most discriminating variables between primary and secondary decays, apart from the IP-related ones, are the $\theta_{\rm DIRA}$ and the Δm—if the $D^{*+} \to D^0(\to h^+h^-)\pi^+$ decay chain has been globally fitted constraining the D^{*+} to originate in the PV (see Sect. 4.5)—. While it is clear why the $\theta_{\rm DIRA}$ variable is distributed differently for primary and secondary decays, the differences for the Δm distributions have a subtler origin. This variable is defined as

$$\begin{aligned}\Delta m &= m(D^0\pi_{\rm s}) - m(D^0)\\ &= \sqrt{m(D^0)^2 + m(\pi_{\rm s})^2 + 2\left[E(D^0)E(\pi_{\rm s}) - p(D^0)p(\pi_{\rm s})\cos\theta\right]} - m(D^0).\end{aligned}$$

While the measurements of the magnitudes of the momenta (and, therefore, of the energies) are nearly independent of the tracking variables and are not affected by the vertex fit, the measurement of the small angle θ between the momenta of the D^0 and of the $\pi_{\rm s}$ is highly influenced by the kinematic vertex fit. In particular, for the secondary decays, the constraint of the D^{*+} to originate in the PV reduces the size of θ, thus reducing also the value of Δm. This effect is shown in 6.4(a), where a clear second peak appears on the left of the central one for high decay times. Cutting on Δm around the signal peak has therefore a non negligible impact on the fraction of secondary decays and in particular on the their kinematic distributions, as the IP-related quantities. This effect cannot easily reproduced with a simple kinematic-based simulation, as the results of the complicated fit to the whole $D^{*+} \to D^0(\to h^+h^-)\pi^+$ decay chain, constraining the D^{*+} to originate in the PV, depend critically on the values and on the complex correlations among tracking uncertainties. Therefore, it was decided not to use the kinematic fit

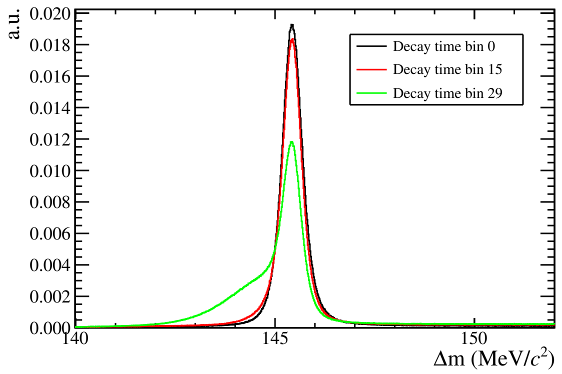

(a) Distributions with the global kinematic fit.

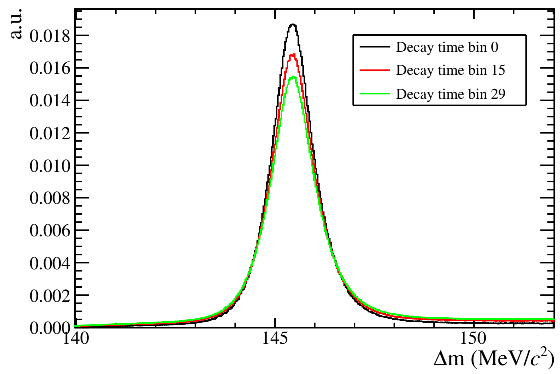

(b) Distributions without the global kinematic fit.

Figure 6.4: Distributions of the Δm, with and without applying the global kinematic fit of the $D^{*+} \to D^0(\to h^+h^-)\pi^+$ decay chain, constraining the D^{*+} to be produced in the PV [44], for the first, the middle and the last bin of decay time, corresponding to the ranges $[0.6000, 0.8038[$, $[1.9533, 2.0408[$ and $[4.9412, 8.000[$ respectively, in units of D^0 mean lives.

with the constraint to the PV, but the raw distribution of the Δm (see Fig. 6.4(b)) for the final measurement. This choice increases the small contamination from random pion events by about a factor of 1.8, corresponding to a degradation in Δm resolution by the same factor, but greatly improves the reliability of the task of subtracting secondary decays.[3]

The requirement on the direction angle ($\theta_{\mathrm{DIRA}} < 17.3\,\mathrm{mrad}$) is implemented at the trigger level and cannot be removed from the selection. However, it does not critically depend on the tracking uncertainties and its impact can be reproduced in a simple kinematic simulation, as all other requirements on basic kinematic observables.

6.3 Final selection

The selection requirements that are used to perform an accurate subtraction of secondary decays are the same as those described in Chap. 4, with the following exceptions:

- at least one of the particles coming from the decay of the D^0 is required to fire the `TrackMVA` HLT1 line, in order to avoid inaccuracies in the correction procedure observed in the events collected with the `TwoTrackMVA` HLT1 lines, as described in Chap. 5 (see Fig. 5.10(d));
- no offline requirement on the χ^2_{IP} of the D^0 is requested, the cut $\chi^2_{\mathrm{IP}}(D^0) < 9$ being substituted by a looser cut on the TIP of the D^0 ($|\mathrm{TIP}| < 200\,\mu\mathrm{m}$), coincident with the fit range used to subtract the contribution from secondary decays, as described in the next sections of this chapter;
- no global kinematic fit of the $D^{*+} \to D^0(\to h^+h^-)\pi^+$ decay chain with the constraint that the D^{*+} is produced in the PV is performed, so that the cut on the Δm distribution does not bias the distribution of the TIP. The signal region is modified accordingly, in order to conserve a central interval containing 95% of the total signal candidates ($[143.95, 147.50]\,\mathrm{MeV}/c^2$).[4]

[3] The systematic uncertainty on the random pion background in the Run 1 measurement of A_Γ was $0.1 \cdot 10^{-4}$, smaller by a factor of 10 than the uncertainty on the secondary decays, $1.0 \cdot 10^{-4}$.

[4] The signal region, differently from that of the D^0 mass, is the same for all $D^0 \to K^-\pi^+$, $D^0 \to K^+K^-$ and $D^0 \to \pi^+\pi^-$ decay modes.

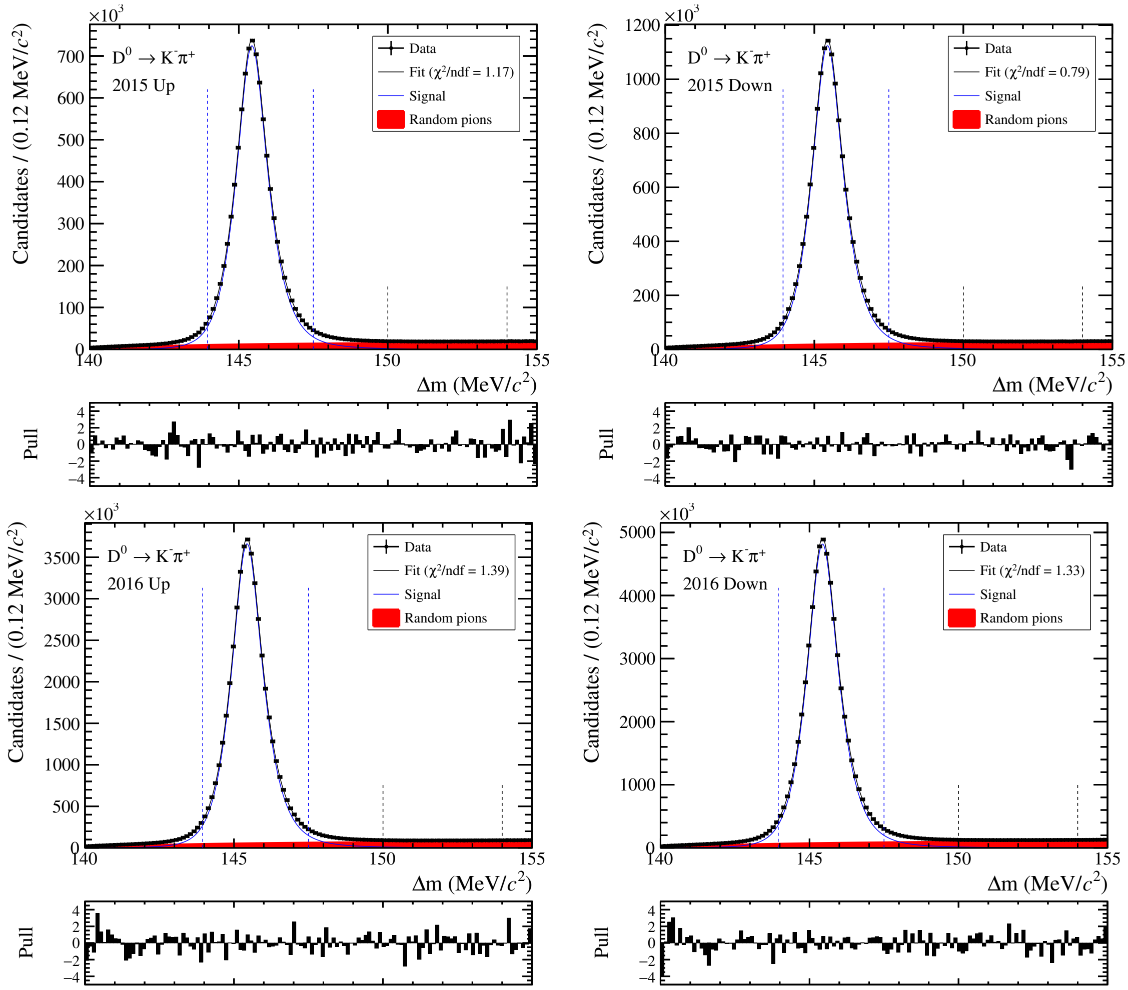

Figure 6.5: Distribution of the mass difference Δm for the $D^0 \to K^-\pi^+$ decays. The fit result and the residuals of the data with respect to the fit curve are also shown.

- D^0 candidates with decay time $< 1\tau(D^0)$ are discarded from the final data sample, in order to remove large uncertainties on the subtraction procedure. This will be discussed later in the next sections of this chapter.

The fits to the final distributions of the Δm for the $D^0 \to K^-\pi^+$ decay mode are displayed in Fig. 6.5, and the total number of decays that are selected by the new requirements described in this section is reported in Table 7.1. The same distributions for the $D^0 \to K^+K^-$ and $D^0 \to \pi^+\pi^-$ decay modes are displayed in Chapter 7 (Figs. 7.1 and 7.2).

6.4 Subtraction of the contribution from secondary decays

In this thesis, a novel approach is developed to subtract the contribution of secondary decays to the raw asymmetry, disentangling the primary and the secondary asymmetries independently in each bin of decay time by means of two successive fit stages. This approach takes full advantage of the huge data samples that are being recorded by the LHCb experiment. The functional form of the TIP distributions of primary and secondary decays are chosen according to a kinematic simulation, as described in Appendix B. Then, the parameters of these distributions and the fraction of secondary decays are extracted, in each bin of decay time, through a fit to the flavour-integrated distributions of the TIP, assuming the TIP distributions of D^0 and $\overline{D}^0$ events to be equal. At this point, the shapes of the distributions and the total fraction of secondary decays in each bin of decay time are fixed, and a simultaneous fit of the TIP distributions of D^0 and $\overline{D}^0$ events is performed in each bin of decay time, leaving as free parameters only the primary and the secondary asymmetries. Finally, the thus obtained primary asymmetry is fitted through a linear function, like in the previous chapter, to extract the value of A_Γ.

6.4.1 Fit of the TIP distributions: stage 1

The true distributions of the TIP of the primary and secondary decays, without considering the experimental uncertainty of the TIP measurement, are modelled in each bin of decay time with a Dirac delta function and a double exponential function, respectively:

$$\begin{aligned}\mathcal{P}^{i,\,\text{true}}_{\text{prim}}(b) &= \delta(b),\\ \mathcal{P}^{i,\,\text{true}}_{\text{sec}}(b;\lambda^i) &= \frac{e^{-\frac{|b|}{\lambda^i}}}{2\lambda^i},\end{aligned}$$

where the subscript i labels the time bin, and the choice of the double-exponential function is motivated by the simulation studies reported in Appendix B. In order to account for the finite experimental resolution of the TIP reconstruction, both distributions are convoluted with a resolution function modelled as the sum of two Gaussian functions

$$\mathcal{R}(b;\boldsymbol{\theta}^i_{\text{res}}) = f^i_{\text{res}}\cdot\mathcal{G}(b;\mu^i,\sigma^i) + [1-f^i_{\text{res}}]\cdot\mathcal{G}(b;\mu^i,\Sigma^i),$$

where

$$\mathcal{G}(b;\mu,\sigma) := \frac{1}{\sqrt{2\pi\sigma^2}}\exp\left[-\frac{1}{2}\left(\frac{b-\mu}{\sigma}\right)^2\right],$$

$\boldsymbol{\theta}^i_{\text{res}} = (f^i_{\text{res}},\mu^i,\sigma^i,\Sigma^i)$ is the vector of the parameters of the resolution function of the i^{th} bin of decay time, μ^i takes into account a possible bias of the measurement of the TIP, shared by the two Gaussian functions, and f^i_{res} is the relative fraction of the resolution function that is described by the first Gaussian. Slight deviations from a pure exponential behaviour of the distributions of the true TIP for the secondary decays are expected to be smoothed by the convolution with the resolution function, as the standard deviation of the resolution function is comparable to the decay length of the exponential distribution.

The probability density functions to describe the observed distributions of the TIP of primary and secondary decays can therefore be written as

$$\begin{aligned}\mathcal{P}^i_{\text{prim}}(b;\boldsymbol{\theta}^i_{\text{res}}) &= \frac{1}{I_{\text{prim}}}\cdot\left\{\mathcal{P}^{i,\,\text{true}}_{\text{prim}}(b)*\mathcal{R}(b;\boldsymbol{\theta}^i_{\text{res}})\right\} = \frac{1}{I_{\text{prim}}}\cdot\mathcal{R}(b;\boldsymbol{\theta}^i_{\text{res}}),\\ \mathcal{P}^i_{\text{sec}}(b;\lambda^i,\boldsymbol{\theta}^i_{\text{res}}) &= \frac{1}{I_{\text{sec}}}\cdot\left\{\mathcal{P}^{i,\,\text{true}}_{\text{sec}}(b;\lambda^i)*\mathcal{R}(b;\boldsymbol{\theta}^i_{\text{res}})\right\},\end{aligned}$$

where I_{prim} and I_{sec} are the proper normalisation factors, after the convolution, in the fitting range ($|\text{TIP}| < 200\,\mu\text{m}$). The final probability density function for the i^{th} decay time bin is

$$\mathcal{P}^i(b;\boldsymbol{\theta}^i) = [1-f^i_{\text{sec}}]\cdot\mathcal{P}^i_{\text{prim}}(b;\boldsymbol{\theta}^i_{\text{res}}) + f^i_{\text{sec}}\cdot\mathcal{P}^i_{\text{sec}}(b;\lambda^i,\boldsymbol{\theta}^i_{\text{res}})$$

where $\boldsymbol{\theta}^i = (f^i_{\text{sec}},\lambda^i,\boldsymbol{\theta}^i_{\text{res}})$ is the vector of the parameters to be fitted to data and f^i_{sec} is the total fraction of secondary decays in the i^{th} bin of decay time. The parameters are extracted through a binned maximum likelihood approach, with a simultaneous fit to the TIP flavour-integrated distributions for all bins of decay time.

Various models have been tested to describe the dependency of the parameters of the resolution model on decay time, whereas the most important physical parameters, f^i_{sec} and λ^i, are always

Table 6.1: Summary of the parametrisations of $f^i_{\rm res}$, σ^i_1 and σ^i_2 as a function of decay time, for the five models considered in the analysis.

Model	$f^i_{\rm res}$	σ^i	Σ^i
free	–	–	–
constant - free	$f^0_{\rm res}$	σ_0	–
linear	–	$\sigma_0 + \sigma_1 \frac{t^i}{\tau(D^0)}$	$\Sigma_0 + \Sigma_1 \frac{t^i}{\tau(D^0)}$
quadratic	–	$\sigma_0 + \sigma_1 \frac{t^i}{\tau(D^0)} + \sigma_2 \left(\frac{t^i}{\tau(D^0)}\right)^2$	$\Sigma_0 + \Sigma_1 \frac{t^i}{\tau(D^0)} + \Sigma_2 \left(\frac{t^i}{\tau(D^0)}\right)^2$
quadratic (shared)	–	$\sigma_0 + \sigma_1 \frac{t^i}{\tau(D^0)} + \sigma_2 \left(\frac{t^i}{\tau(D^0)}\right)^2$	$s_0 \left[\sigma_0 + \sigma_1 \frac{t^i}{\tau(D^0)} + \sigma_2 \left(\frac{t^i}{\tau(D^0)}\right)^2\right]$

left free to change independently from bin to bin of decay time. The bias μ is found to be significantly different from zero, and to change slightly in the first bins of decay time, eventually approaching a constant value after about $2\tau(D^0)$. Therefore, it is parametrised as a function of decay time with an erf function ($\mu^i = \mu_0 \cdot \mathrm{erf}\left[(t^i - \mu_1)/\mu_2\right]$).[5] Finally, $f^i_{\rm res}$, σ^i_1 and σ^i_2 are allowed to vary in the following ways:

- "*free*" model: all $f^i_{\rm res}$, σ^i_1 and σ^i_2 completely independent of each other for different time bins;
- "*constant - free*" model: $f^i_{\rm res}$ and σ^i_1 constant as a function of time, σ^i_2 independent for different time bins;
- "*linear*" model: $f^i_{\rm res}$ independent for different time bins, σ^i_1 and σ^i_2 described by two functions that are linear in time;
- "*quadratic*" model: $f^i_{\rm res}$ independent for different time bins, σ^i_1 and σ^i_2 described by two functions that are quadratic in time;
- "*quadratic (shared)*" model: $f^i_{\rm res}$ independent for different time bins, σ^i_1 and σ^i_2 described by a single quadratic function of time, but with a different global scale factor.

The different parametrisations are summarised in Table 6.1. The models cover a broad class of hypothesis on the physical origin of the resolution, that is composed by a part that is constant in time, being due to the finite resolution of the reconstruction of the vertices, and another one that is expected to increase with time, due to the uncertainty on the direction of the D^0 meson. It is very difficult to accurately know the resolution function of the TIP observable and, in particular, how it depends on the decay time. Even a realistic simulation based on the GEANT4 package, along with a detailed knowledge of the LHCb detector geometry and material, may be not reliable at this level of precision.[6] In order to overtake this challenge, the only feasible path to be pursued, also in preparation for future A_Γ measurements at much higher precision, seems the usage of simple reliable models, that can be derived from first principles and empirically parametrised with a limited number of degrees of freedom. Of course, an appropriate systematic uncertainty must be assessed for this procedure.

The fitted values of the parameters of the various models for the 2016 *MagUp* subsample are displayed in Fig. 6.6. Examples of the fit projections on the data for different models in the first, the middle and the last time bins are displayed in Figs. 6.7, 6.8, 6.9. The "*quadratic (shared)*" model shows the worst agreement with the data (see Fig. 6.7), owing to the stiff

[5] This choice is not expected to influence significantly the discrimination of the primary and of the secondary components of the data sample, since their TIP distributions are both expected to be symmetric with respect to μ.

[6] Moreover, it should be kept in mind that the current available LHCb computing power is not sufficient to simulate, in a reasonable time scale, a sample with the same (or larger) size of the available data sample.

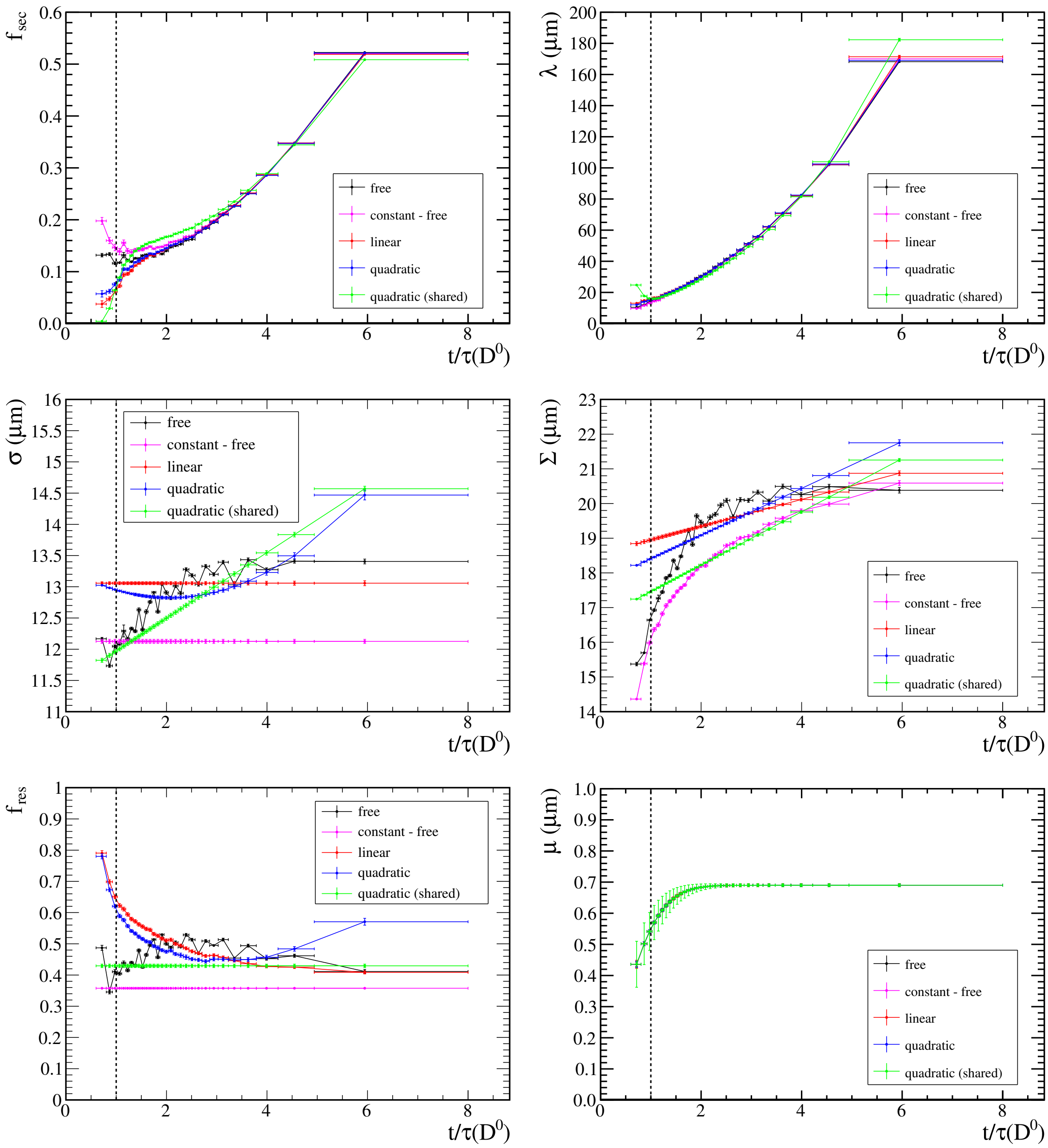

Figure 6.6: Values of the fitted parameters, as a function of decay time, for the models listed in Table 6.1. The cut at $1\tau(D^0)$, removing the first three bins of decay time, is displayed by the black dashed line.

parametrisation of σ_1^i and σ_2^i, and does not describe satisfactorily the data at both the edges of the time distribution. In the other models, although the values of σ_1^i and σ_2^i are very different from model to model, the fraction of secondary decays and the values of λ show a good agreement with each other for decay times larger than $2\tau(D^0)$. On the contrary, at lower times, the fraction of secondary decays changes significantly, depending on the parametrisation of the two σ. This is because in this range a little non-Gaussian tail of the resolution function, mainly populated by primary decays, would be nearly indistinguishable from the tails of the TIP distribution that are due to the contamination from secondary decays (see uppermost plots of Figs. 6.7, 6.8, 6.9). Comparing the results for different models (see Fig. 6.6) it was found that the values of f_{sec} as a function of decay time are very similar except for bins at lower decay times. In particular, the first three lower bins, corresponding to decay times lower than $1\tau(D^0)$, show the largest variations in the determination of f_{sec}. This is probably an unavoidable effect, due to the indistinguishability of primary and secondary decays at low decay times, and likely any alternative method or discriminating observable would have similar weaknesses. In addition, it was also found that some fluctuations are present in the value of f_{sec} for the "*free*" model in the first three bins of decay time, by comparing results in different subsamples. The are likely due to the same difficulties of the fits with different models, as explained above.

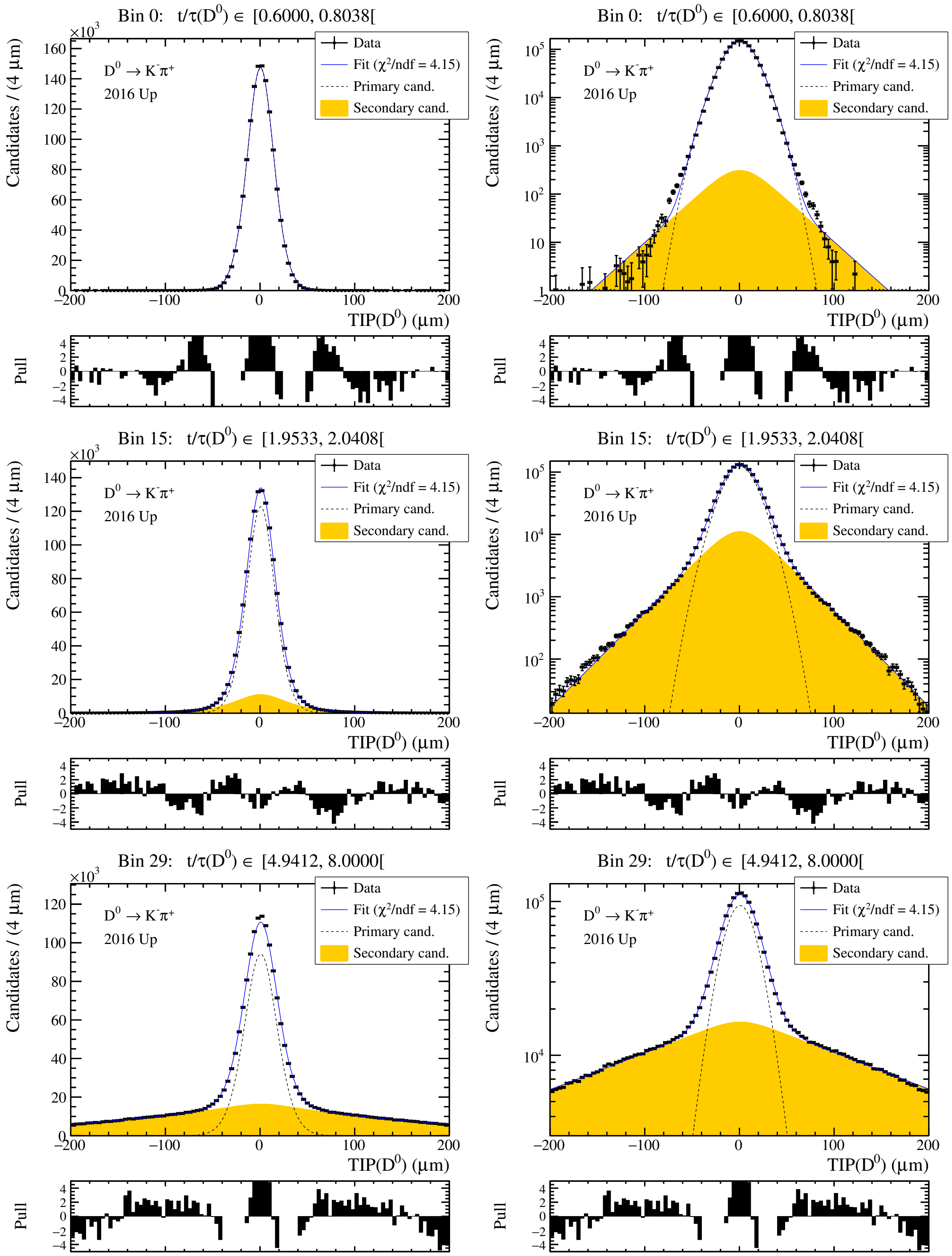

Figure 6.7: Projection of the fit and residuals of the data with respect to the fit, normalised by the relative error, for the first, the middle and the last decay time bins ("*quadratic (shared)*" model).

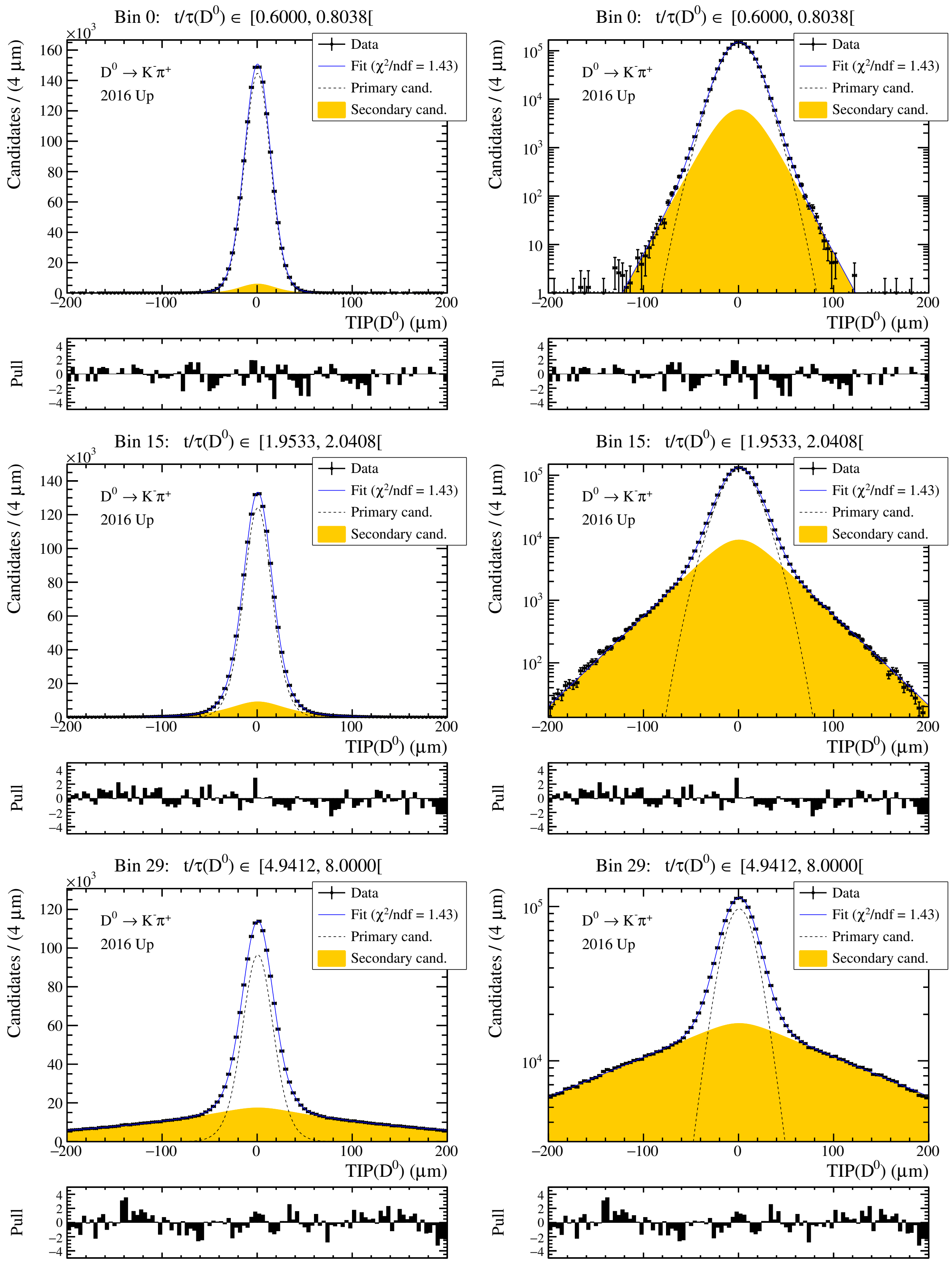

Figure 6.8: Projection of the fit and residuals of the data with respect to the fit, normalised by the relative error, for the first, the middle and the last decay time bins ("*free*" model).

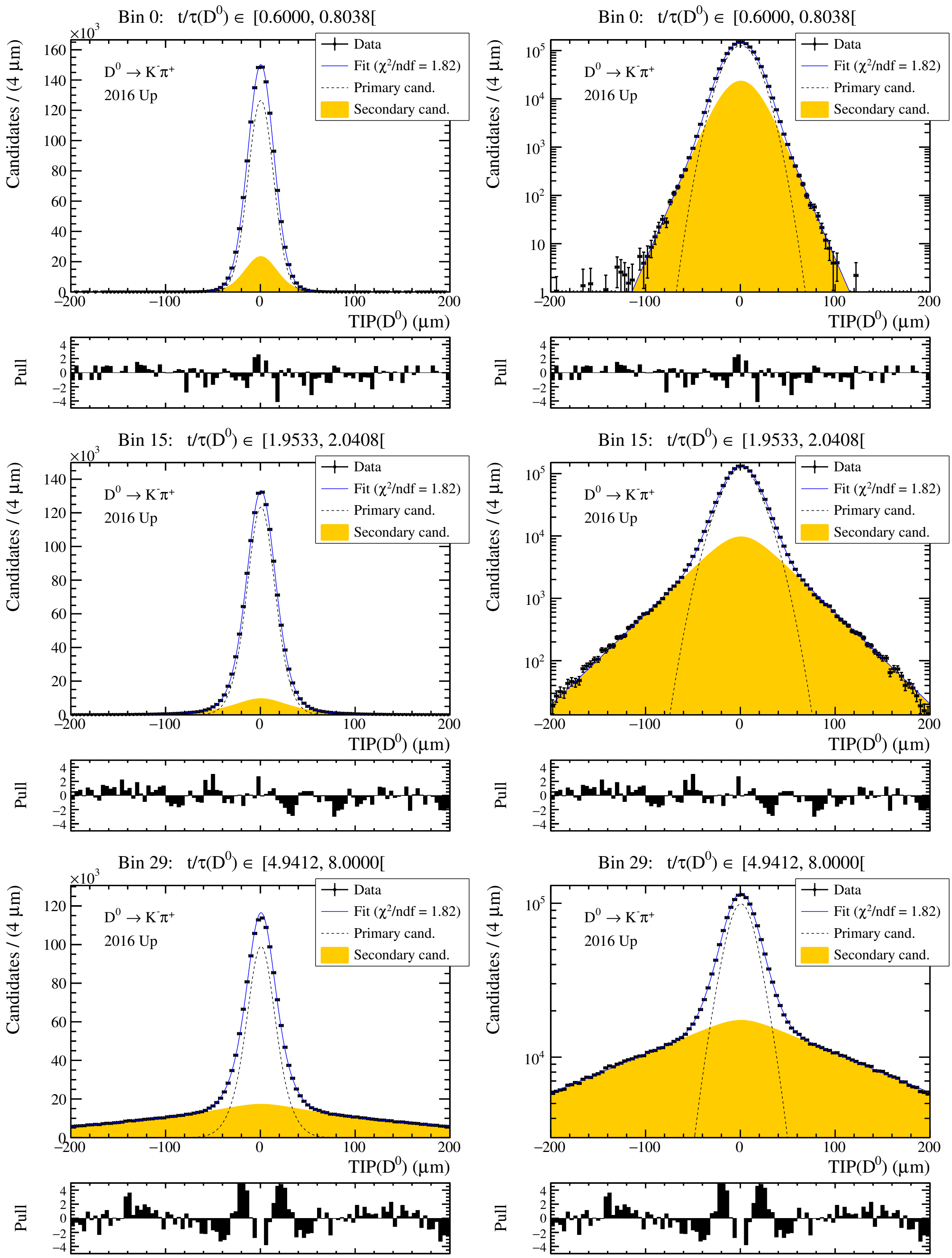

Figure 6.9: Projection of the fit and residuals of the data with respect to the fit, normalised by the relative error, for the first, the middle and the last decay time bins ("*constant - free*" model).

6.4.2 Fit of the TIP distributions: stage 2

At this point, the distributions of primary and secondary decays and the total fraction of secondary decays are fixed in each bin of decay time to the values obtained in the fit described in the previous section. Then, the TIP distributions of D^0 and $\overline{D}^0$ decays are fitted, independently for each time bin, but simultaneously for D^0 and $\overline{D}^0$ decays, using the following distribution functions:

$$\mathcal{P}^i_{\pm}(b;\boldsymbol{\theta}^i) = [1 - f^i_{\rm sec}] \cdot \frac{1 \pm A^i_{\rm prim}}{2} \cdot \mathcal{P}^i_{\rm prim}(b;\boldsymbol{\theta}^i_{\rm res}) + f^i_{\rm sec} \cdot \frac{1 \pm A^i_{\rm sec}}{2} \cdot \mathcal{P}^i_{\rm sec}(b;\lambda^i,\boldsymbol{\theta}^i_{\rm res}),$$

where "+" identifies the D^0 mesons and "−" the $\overline{D}^0$ ones. Only the primary and the secondary asymmetries, $A^i_{\rm prim}$ and $A^i_{\rm sec}$, are left free to vary. The fits are performed for both the TIP distributions as calculated from raw data and after the reweighing to remove detector-induced, time-dependent asymmetries that is described in Sect. 5.3 ("corrected" data).

6.4.3 Results for the $D^0 \to K^-\pi^+$ sample

The two-staged fit to the TIP distributions is performed independently for the four Cabibbo-favoured $D^0 \to K^-\pi^+$ subsamples, in order to subtract the contribution to the raw asymmetry from the secondary decays. This is repeated for all the different resolution models, as described in Sect. 6.4.1, and the results averaged over all subsamples are reported in Table 6.2 (left column), where the primary asymmetry is fitted with a linear function and the value of $A_\Gamma^{K\pi}$ is extracted as usual, as the opposite of the slope. As an example, the resulting asymmetry of primary and secondary decays for the "*free*" model, in the 2016 *MagUp* subsample, are displayed in Fig. 6.12, with the result of the linear fit superimposed. Fig. 6.11 instead shows, for the same subsample and resolution model, the difference between the raw asymmetry—as calculated before the subtraction of the contribution from secondary decays—and the primary asymmetry.

Since the determination of the relative fraction of secondary decays is affected by large uncertainties at low decay time bins, as described in Sect. 6.4.1, Table 6.2 also reports the $A_\Gamma^{K\pi}$ results, where events at lower decay times, $t < \tau(D^0)$, are discarded from the final data sample. The maximum variations of the $A_\Gamma^{K\pi}$ results, due to the uncertainties on the resolution model that directly influence the subtraction of the secondary decays component, moves from $0.6 \cdot 10^{-4}$ to $0.2 \cdot 10^{-4}$ when $t < \tau(D^0)$ is requested. In both cases the accuracy of the subtraction procedure is very precise, well below statistical uncertainties. This will be discussed in detail in the next chapter, where all systematic uncertainties will be assessed; however, it is important to compare these systematic variations, with or without the cut on the proper decay time, to the value of the same systematic uncertainty assigned in the Run 1 measurement, $1.0 \cdot 10^{-4}$, a factor of 1.6 or 5 larger than these variations, respectively. All other uncertainties related to the secondary decays subtraction procedure are expected to be negligible with respect to that of the TIP resolution model.

The "*free*" model is chosen as the central one to perform the measurement of A_Γ. This choice is motivated by the fact that the behaviour of the relative fraction of secondary decays as a function of decay time shows a dependence on time that is very similar to the one obtained with simulation studies (see Fig. B.2), and its fit to the TIP distributions returns the minimum χ^2 among all the models. The projections of its fit to the TIP distributions for each bin of decay time are displayed for the 2016 *MagUp* subsample, both in linear and in logarithmic scale, in Appendix C.

For the final measurement presented in this thesis the first three bins of decay time are discarded from the final data sample in order to demonstrate that systematic uncertainties on the secondary decays subtraction procedure can be taken under control at the unprecedented level of precision of $0.2 \cdot 10^{-4}$, with a view to future measurements at much higher precision. The

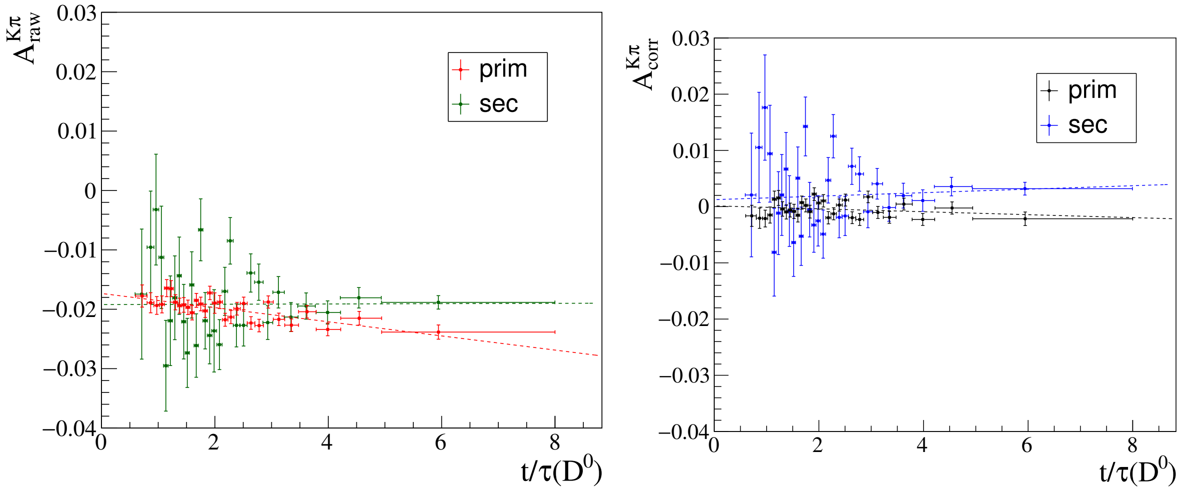

Figure 6.10: Asymmetry of primary and secondary decays in the 2016 *MagUp* subsample as calculated from the raw (left) and the corrected (right) TIP distributions.

final results, for all subsamples of the Cabibbo-favoured $D^0 \to K^-\pi^+$ decay mode, are displayed in Fig. 6.12, where the individual measurements are in good agreement with each other and the weighted average is in agreement within 2σ with the hypothesis of *CP* conservation,

$$A_\Gamma^{K\pi} = (2.7 \pm 1.3) \cdot 10^{-4}.$$

However, the choice of discarding events with $t < \tau(D^0)$ provokes a degradation of the statistical precision of about 15%, to be added to a further statistical degradation of 20% due to the intrinsic nature of the fitting method, where the uncertainty on the fraction and on the asymmetry of the secondary decays reflects in a larger statistical uncertainty of the primary asymmetry.[7] The total statistical degradation is about 35% with respect to the same measurement obtained without the secondary decays subtraction (see Fig. 5.8(a)), and it is not compensated by the fact that the systematic uncertainty moves from $1.0 \cdot 10^{-4}$ to $0.2 \cdot 10^{-4}$. This is particularly relevant for the $D^0 \to K^+K^-$ and $D^0 \to \pi^+\pi^-$ decay modes, where the statistical uncertainty is larger than that of the $D^0 \to K^-\pi^+$ sample, and one may decide to relax the systematic uncertainties in order to reduce as much as possible the statistical one,[8] and thus the total uncertainty. However, the LHCb experiment is quickly collecting new data (in the first half of 2017 it has already collected about $0.6\,\text{fb}^{-1}$ of integrated luminosity) and a degradation of the statistical uncertainty seems affordable in order to gain a much better knowledge of the available data. In addition, the short term plan is to recover as soon as possible the data collected with the `TwoTrackMVA` lines, already available on disk, that are discarded for the time being.

[7]In other words, part of the systematic uncertainty due to the presence of the secondary decays is transferred to the statistical uncertainty on the primary decays.

[8]The statistical uncertainty is equal to $3.8 \cdot 10^{-4}$ for the $D^0 \to K^+K^-$ decay mode and $6.7 \cdot 10^{-4}$ for the $D^0 \to \pi^+\pi^-$.

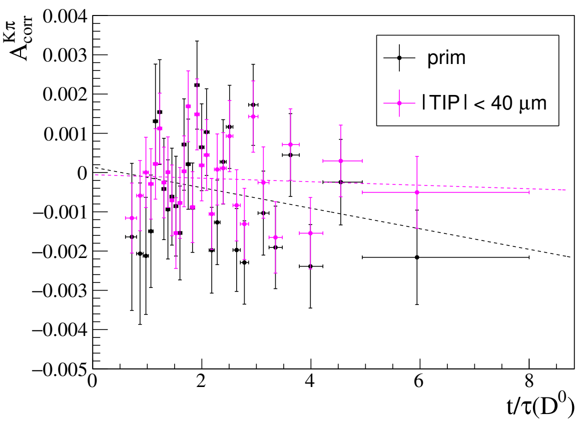

Figure 6.11: Asymmetry of primary decays and of all events with $\left|\mathrm{TIP}(D^0)\right| < 40\,\mu\mathrm{m}$, similar to the cut $\chi^2_{\mathrm{IP}}(D^0) < 9$ of Chap. 4 and 5, for the 2016 *MagUp* subsample (TIP distributions from corrected data).

Table 6.2: Values of $A_\Gamma^{K\pi}$, averaged over the four $\{2015,\ 2016\} \times \{MagUp,\ MagDown\}$ subsamples, for the four models of Table 6.1, in units of 10^{-4}. Both the values obtained using all the 30 decay time bins and those where the first three bins are discarded ($t/\tau(D^0) > 1$) are reported.

Model	$A_\Gamma^{K\pi}$	$A_\Gamma^{K\pi}$ $(t/\tau(D^0) > 1)$
free	2.4 ± 1.1	2.7 ± 1.3
free - constant	1.8 ± 1.2	2.5 ± 1.3
linear	2.3 ± 1.1	2.7 ± 1.2
quadratic	2.2 ± 1.1	2.6 ± 1.2
quadratic (shared)	2.2 ± 1.1	2.5 ± 1.3
max. variation with respect to the free model	0.6	0.2

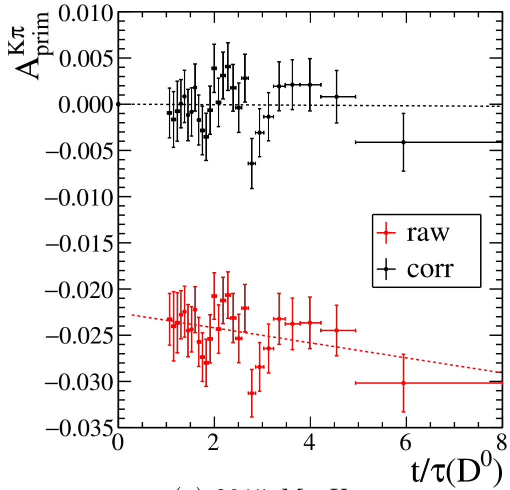

(a) 2015 *MagUp*.

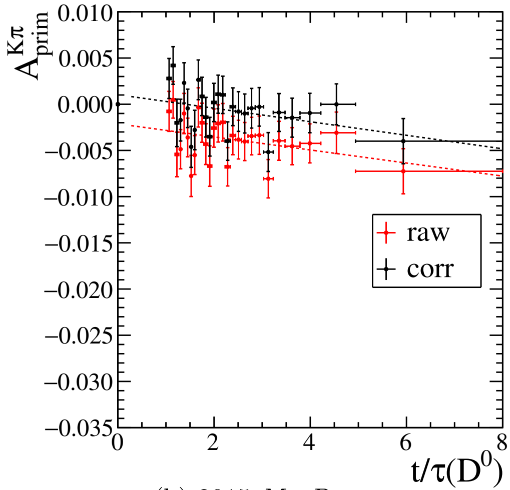

(b) 2015 *MagDown*.

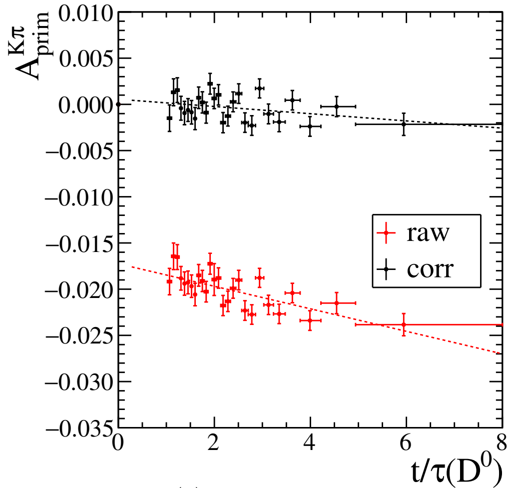

(c) 2016 *MagUp*.

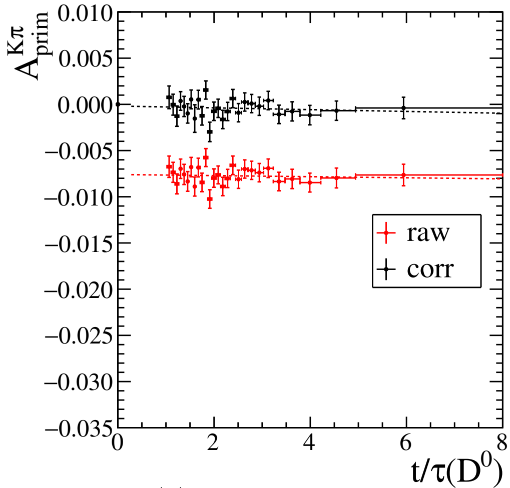

(d) 2016 *MagDown*.

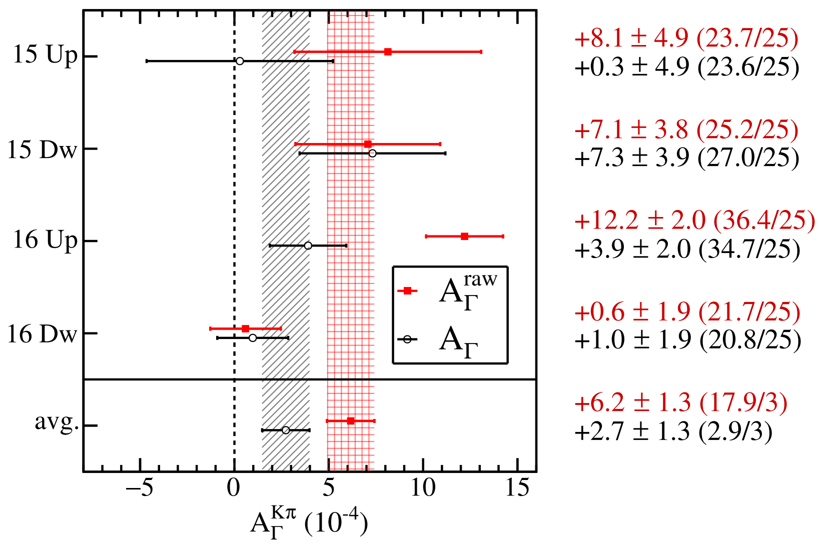

(e) Summary and average.

Figure 6.12: Linear fit to the time-dependent asymmetry after the subtraction of the secondary decays, for the $D^0 \to K^-\pi^+$ decay mode.

Chapter 7

Measurement of the A_Γ parameter

This chapter presents the preliminary measurement of A_Γ with the $D^0 \to K^+K^-$ and $D^0 \to \pi^+\pi^-$ samples. The value of A_Γ is blinded in order not to bias the decisions of the analysts before the final approval of the analysis procedure by the LHCb collaboration. The main systematic uncertainties that affect the measurement are briefly discussed, referring to the Run 1 analysis for the ones that are not expected to have changed.

7.1 Extraction of $A_\Gamma(D^0 \to K^+K^-)$ and $A_\Gamma(D^0 \to \pi^+\pi^-)$

Once the reliability of the analysis method has been verified with the high-statistics $D^0 \to K^-\pi^+$ sample, as it has been done in Chap. 5 for the procedure to remove the detector-induced time-dependent asymmetries and in Chap. 6 for the subtraction of the contribution from secondary decays, it is possible to extend the measurement to the $D^0 \to K^+K^-$ and $D^0 \to \pi^+\pi^-$ samples, in order to extract the value of the *CP* violation parameter A_Γ. However, the value of the measured A_Γ is blinded, pending the receipt of the approval of the measurement strategy by the LHCb collaboration. This is done by adding to all the measured asymmetries—$A_{\text{prim}}(t)$, $A_{\text{sec}}(t)$, *etc.*—a term that is constant and one that is linear in time:

$$A(t) \to A(t) + A_0^{\text{blind}} - A_\Gamma^{\text{blind}} \cdot \frac{t}{\tau(D^0)},$$

where the blinding parameters A_0^{blind} and A_Γ^{blind} are random numbers generated in the ranges $[-0.1, 0.1]$ and $[-0.02, 0.02]$, respectively. The range for A_Γ^{blind}, corresponding to about 120 times the current statistical uncertainty on A_Γ, ensures that no information on the real value of A_Γ can be extracted from the blinded value extracted from the linear fit. The constant shift A_0^{blind}, instead, is required because the total asymmetry of the data sample after the correction procedure is null by construction. Therefore, even if the asymmetry is shifted as a function of decay time with the linear blinding term, a negative value of the intercept of the asymmetry with the y axis would signal a positive value of the real slope of the asymmetry, and therefore a negative value of A_Γ, and *vice versa.* The blinding parameters are chosen to be the same for the $D^0 \to K^+K^-$ and $D^0 \to \pi^+\pi^-$ decay modes, so that the compatibility between the measurements of $A_\Gamma(K^+K^-)$ and $A_\Gamma(\pi^+\pi^-)$ can be assessed even if their values are blinded.

The data sample that is used for the measurement is mainly described in Chap. 4, but is properly modified following the prescriptions of Sect. 6.3 to allow the precise subtraction of the contribution from secondary decays that is described in Chap. 6. The measurement is performed separately for the four subsamples $\{2015,\ 2016\} \times \{$*MagUp*, *MagDown*$\}$, in order to highlight possible discrepancies among the results obtained with different data-taking conditions. The results of the fits to the Δm distributions are displayed in Figs. 7.1 and 7.2 for the $D^0 \to K^+K^-$

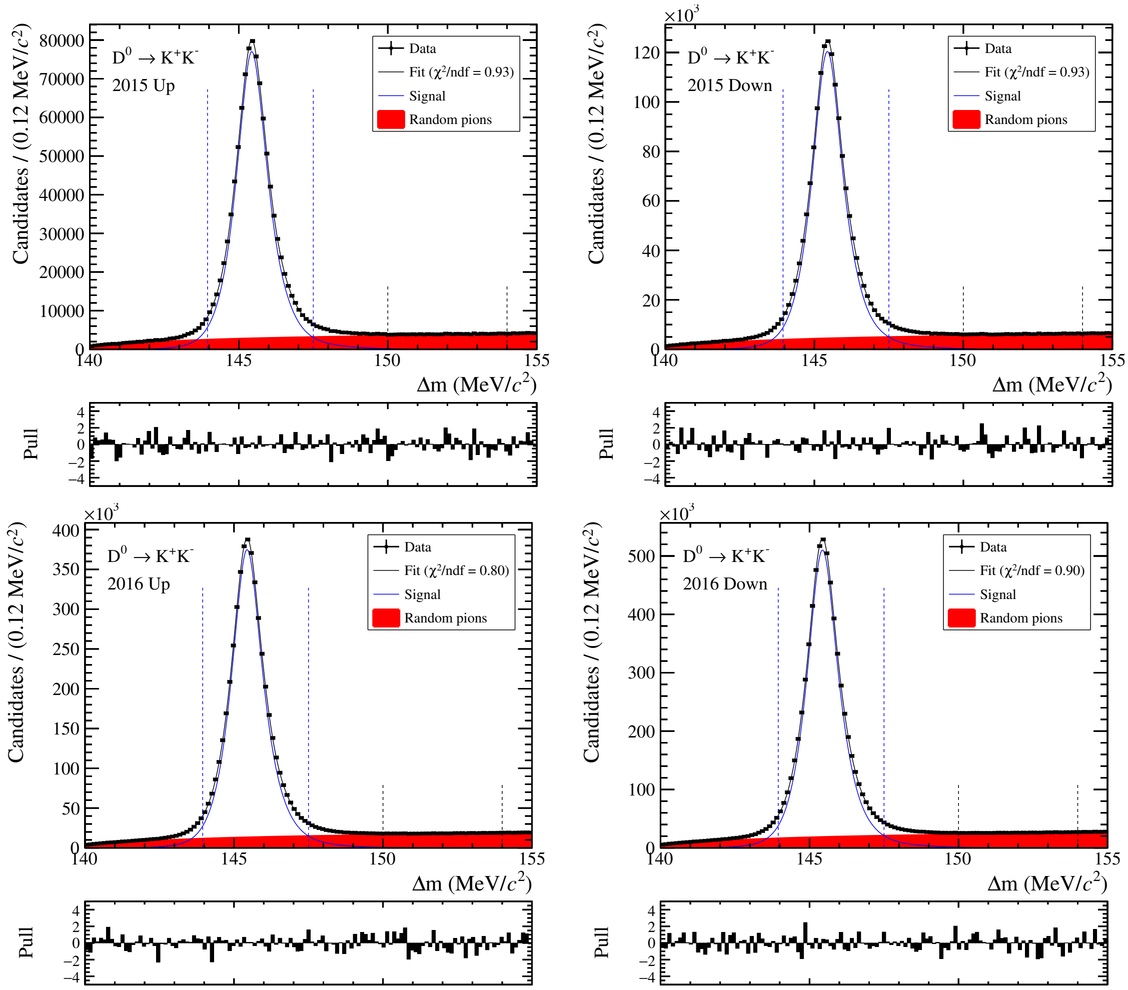

Figure 7.1: Distribution of the mass difference Δm for the $D^0 \to K^+K^-$ decays. The fit result and the residuals of the data with respect to the fit curve are also shown.

Table 7.1: Number of candidates selected by the cuts used in the final analysis, in millions.

Data sample	$\int \mathcal{L}\,\mathrm{dt}$ (fb^{-1})	$D^0 \to K^-\pi^+$	$D^0 \to K^+K^-$	$D^0 \to \pi^+\pi^-$
2015 *MagUp*	0.12	8.7	0.92	0.31
2015 *MagDown*	0.16	13.4	1.43	0.49
2016 *MagUp*	0.71	43.6	4.45	1.62
2016 *MagDown*	0.75	57.6	6.09	2.08
tot	1.74	123.3	12.89	4.50

and the $D^0 \to \pi^+\pi^-$ decay modes, respectively; the total number of candidates for all the decay modes are reported in Table 7.1. Once the fits have been performed, the weights for the correction procedure described in Sect. 5.3 are calculated from the sideband-subtracted distributions of the slow pion momentum in the (θ_x, θ_y, k) space. The weights are calculated independently for each decay mode and subsample. Then, for each bin of decay time, the raw (corrected) TIP distributions of D^0 and $\overline{D}^0$ decays are fitted simultaneously following the procedure described in Sect. 6.4.2, to subtract the contribution of secondary decays to the asymmetry, thus extracting the values of the primary raw (corrected) asymmetry. In these fits, the templates for the primary

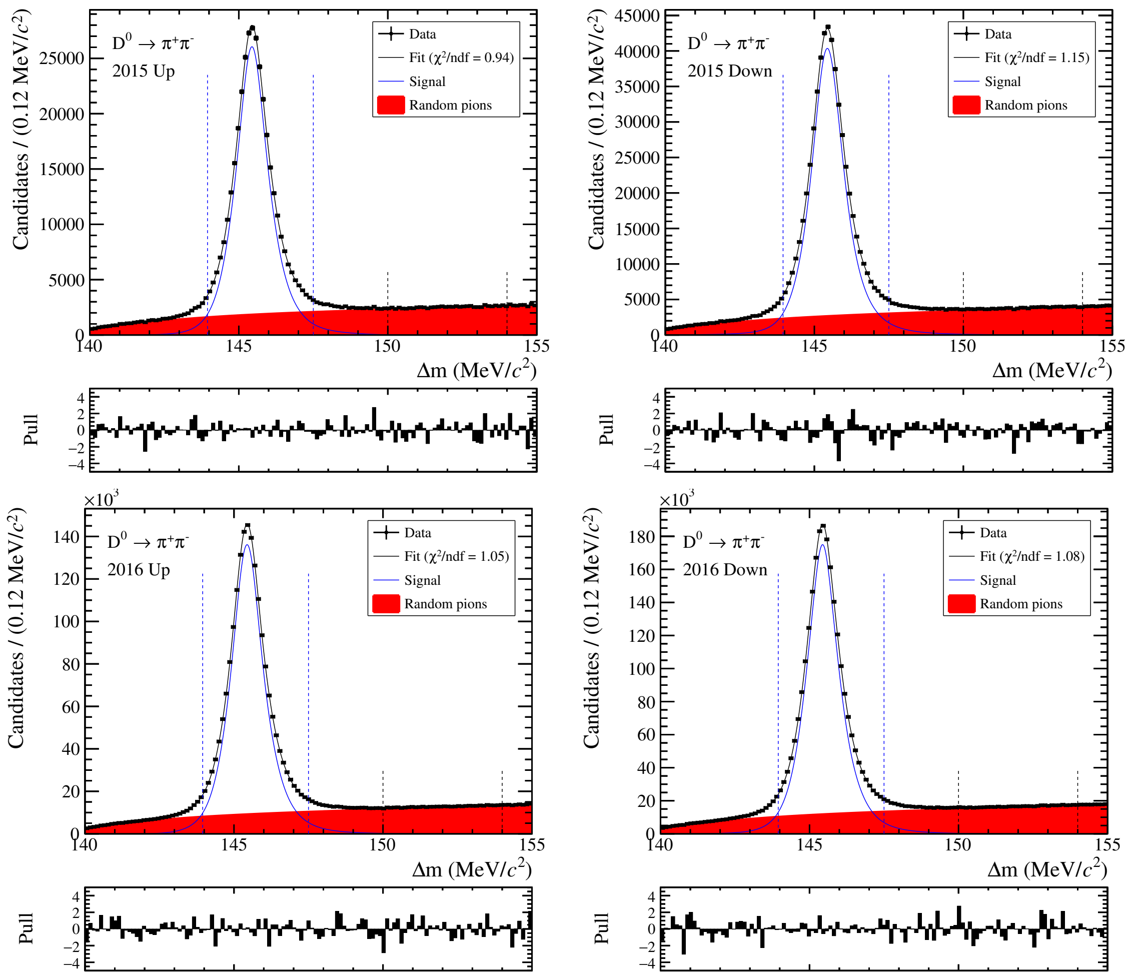

Figure 7.2: Distribution of the mass difference Δm for the $D^0 \to \pi^+\pi^-$ decays. The fit result and the residuals of the data with respect to the fit curve are also shown.

and secondary distributions of the TIP, as well as the total fraction of secondary decays, are fixed to those that were obtained in the fits performed in the same subsample, but using the high-statistics $D^0 \to K^-\pi^+$ decays. This choice improves the stability of the fits and the accuracy of the distributions for primary and secondary decays, without introducing significant systematic uncertainties in the measurement. Finally, the thus obtained values of the primary asymmetry as a function of decay time are shifted with the blinding procedure and are fitted with a linear function; A_Γ is then extracted as the opposite of the slope.

The results of the linear fit to the asymmetry are displayed, for all four subsamples, in Figs. 7.3 and 7.4 for the $D^0 \to K^+K^-$ and the $D^0 \to \pi^+\pi^-$ decay modes, respectively. The measurements among the four subsamples, for both the $D^0 \to K^+K^-$ and the $D^0 \to \pi^+\pi^-$ decay modes, are in agreement with each other within 2σ. A high χ^2 is obtained in the measurement of $A_\Gamma(K^+K^-)$ for the 2015 *MagDown* subsample; however, no significant patterns are pinpointed in the time behaviour of the asymmetry, and the effect is attributed to a statistical fluctuation. The final values of $A_\Gamma(K^+K^-)$ and $A_\Gamma(\pi^+\pi^-)$,

$$A_\Gamma(D^0 \to K^+K^-) = (-60.9 \pm 3.8 \pm 0.6) \cdot 10^{-4},$$
$$A_\Gamma(D^0 \to \pi^+\pi^-) = (-62.5 \pm 6.7 \pm 0.5) \cdot 10^{-4},$$

are compatible within 1σ.

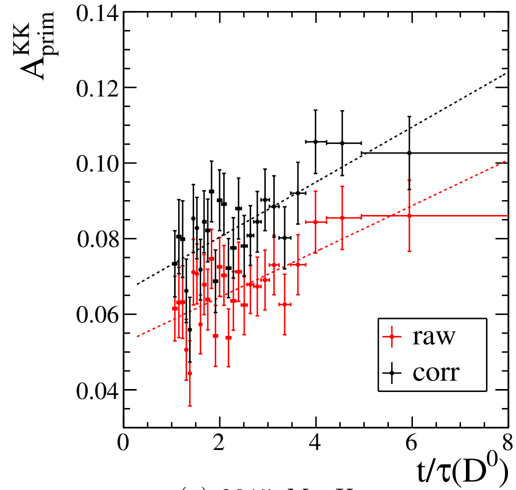

(a) 2015 *MagUp*.

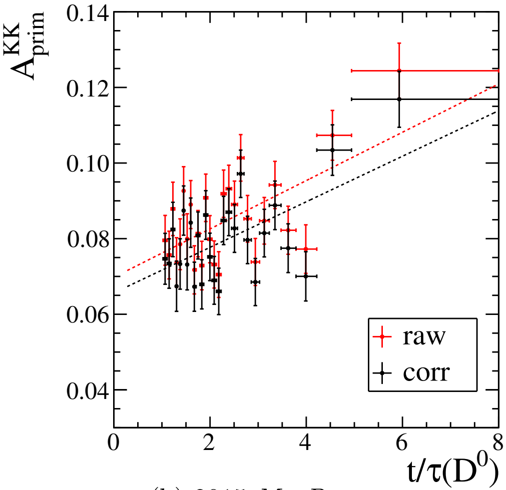

(b) 2015 *MagDown*.

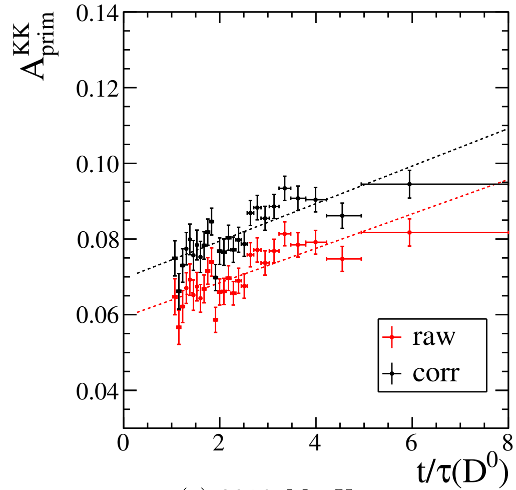

(c) 2016 *MagUp*.

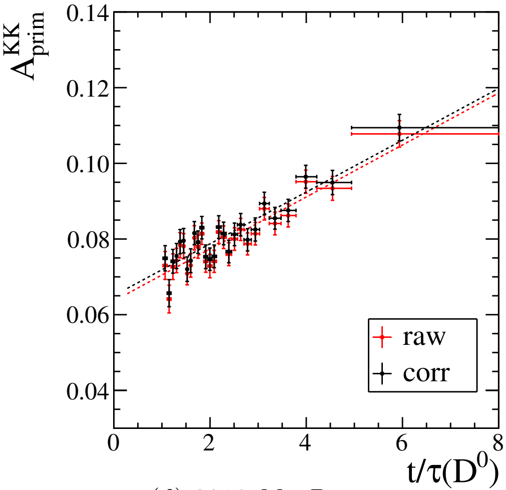

(d) 2016 *MagDown*.

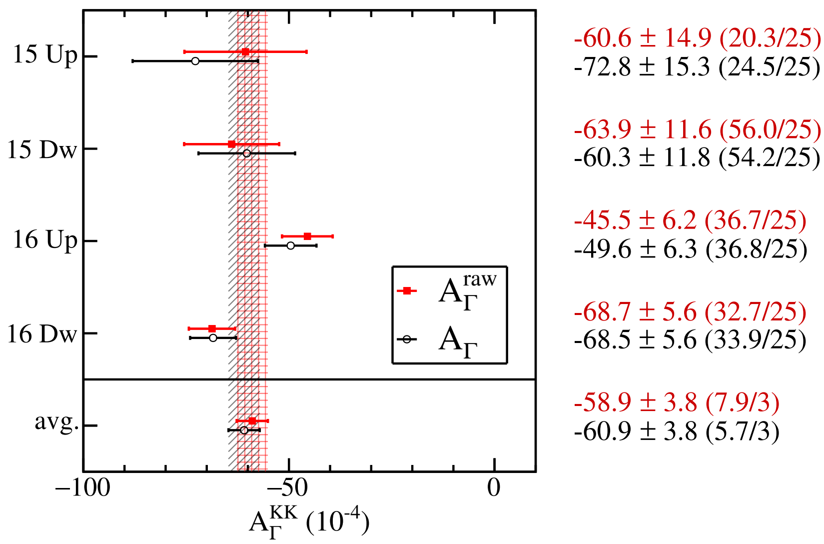

(e) Summary and average.

Figure 7.3: Linear fit to the time-dependent asymmetry after the subtraction of the secondary decays for the $D^0 \to K^+K^-$ decay mode.

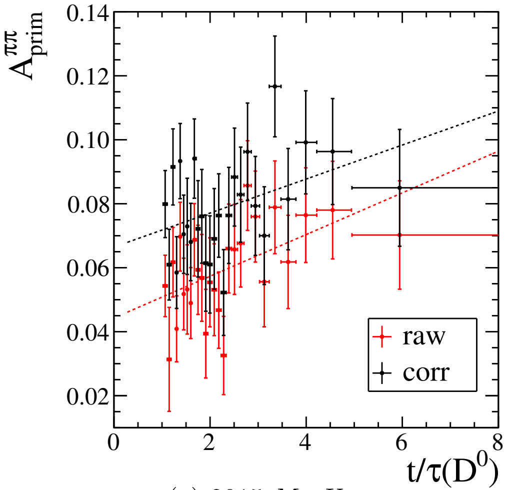

(a) 2015 *MagUp*.

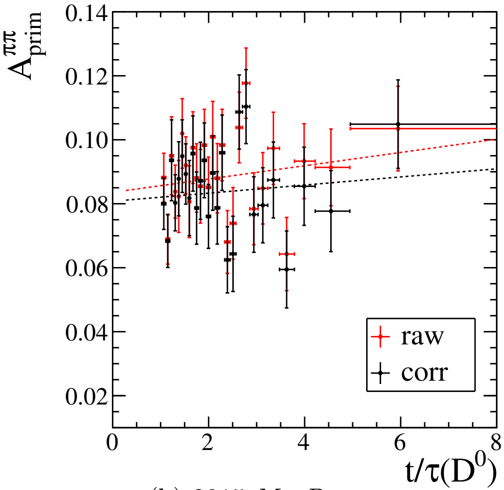

(b) 2015 *MagDown*.

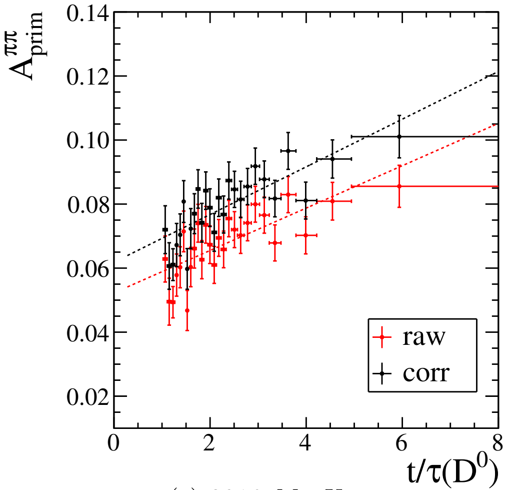

(c) 2016 *MagUp*.

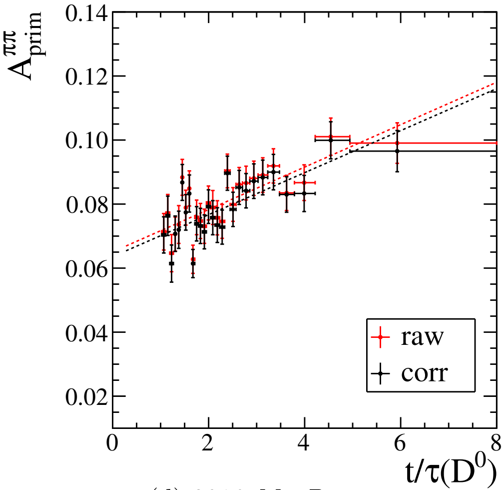

(d) 2016 *MagDown*.

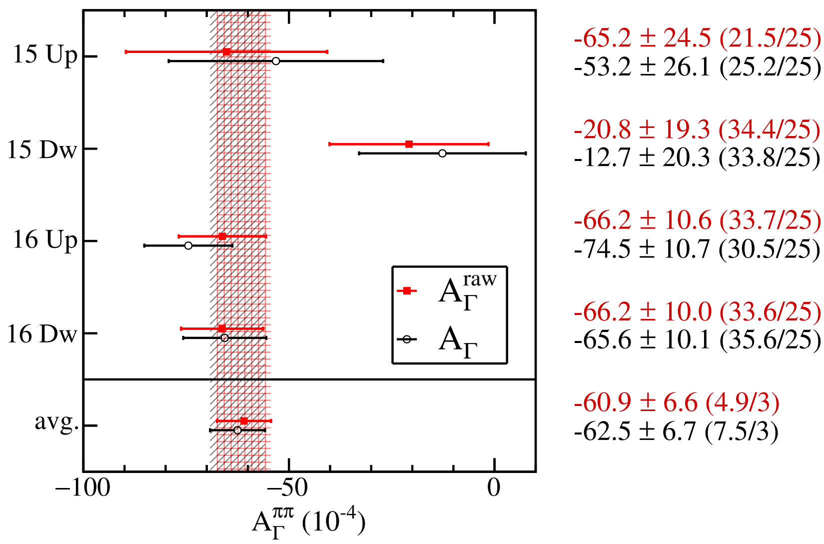

(e) Summary and average.

Figure 7.4: Linear fit to the time-dependent asymmetry after the subtraction of the secondary decays for the $D^0 \to \pi^+\pi^-$ decay mode.

7.2 Systematic uncertainties

This section briefly reviews the main systematic uncertainties that affect the measurement of A_Γ. Most of them are not expected to have changed from Run 1 measurement to that of Run 2. Therefore, since their precise evaluation would have taken a significant amount of time and computing power, for the time being they are only roughly estimated, waiting for the analysis procedure to be approved by the collaboration, in order not to evaluate them twice. On the contrary, the systematic uncertainty on the contribution to A_Γ from the secondary decays has substantially changed, owing to the introduction of the subtraction procedure of Chap. 6, and is described in detail.

Correction discretisation The correction procedure that is employed to remove the detector-induced, time-dependent charge asymmetries from the sample (see Sect. 5.3), performs an equalisation of the momentum distributions of the π_s^+ and π_s^- calculating the appropriate correction weights through a binned approach in the three-dimensional (θ_x, θ_y, k) space.[1] Nevertheless, the weighting functions are, in principle, continuous functions of the momentum of the slow pions. Therefore, the discretisation of the correction procedure intrinsically degrades its accuracy, even in the limit of large number of events per bin. During the Run 1 measurement, a systematic uncertainty was assessed to account for this effect, by varying the binning scheme for the $D^0 \to K^-\pi^+$ sample and observing the impact of these changes on the final value of $A_\Gamma^{K\pi}$.[2] As this thesis exploits the same binning scheme of the Run 1 measurement, the systematic uncertainty is assumed to be of the same size $(0.2 \cdot 10^{-4})$.

Sideband subtraction The sideband subtraction procedure that is used to subtract the residual, combinatorial background under the Δm peak that comes from random associations of D^0 mesons with slow pions that are independently produced in the primary pp collisions (see Sect. 4.5), relies on two main assumptions. The first is that the number of these background events that lie under the Δm peak is accurately estimated, and the second is that their kinematic distributions are equal to those of the random background of the sideband. Deviations from this behaviour were assessed in the Run 1 analysis by comparing the kinematic distributions of the events in the signal region and in the sideband, by measuring the value of $A_\Gamma^{K\pi}$ in the sideband, and by varying the range of the sideband that is used for the subtraction. The final systematic uncertainty on the sideband subtraction was, for Run 1 analysis, $0.1 \cdot 10^{-4}$. The behaviour of the sideband events is not expected to have changed in Run 2 with respect to Run 1. However, the removal of the global kinematic fit to the $D^{*+} \to D^0(\to h^+h^-)\pi^+$ decay chain in the final selection procedure has provoked a loss of precision in reconstructing the Δm peak by about a factor of 2. The contamination of the data sample from the random background has doubled, accordingly. Therefore, the systematic uncertainty is estimated to have doubled, too, reaching the value of $0.2 \cdot 10^{-4}$.

Subtraction of secondary decays The systematic uncertainty assessed for the contribution to the A_Γ value because of the presence of a residual contamination of secondary decays, in the previous iteration of this measurement, conservatively covered the full size of the effect. The contamination was reduced at the level of few per cents with a tight cut on the $\chi^2_{\rm IP}$ of the D^0 meson, and any attempt to subtract that from the final data sample resulted to produce uncertainties comparable or larger than the bias itself. That was the dominating the systematic uncertainty on final A_Γ measurement, with a value of $0.8 \cdot 10^{-4}$ and $1.2 \cdot 10^{-4}$ for the $D^0 \to K^+K^-$ and $D^0 \to \pi^+\pi^-$ decay modes, respectively.[3]

[1] For the definition of these quantities, see Eq. (5.3).

[2] In particular, the number of bins was both increased and reduced up to a factor of 8.

[3] In the $D^0 \to K^-\pi^+$ sample, it was estimated to contribute to $A_\Gamma^{K\pi}$ with a value of $1.0 \cdot 10^{-4}$.

The procedure developed in this thesis, on the contrary, is able to subtract this dangerous background and allows a significant reduction of the associated systematic uncertainty, well below the limit found in the Run 1 measurement. The methodology, described in detail in Chap. 6, uses the discriminant power of the TIP observable to disentangle the primary and the secondary components. The distribution of the primary component is modelled with the sum of two Gaussian functions, while that of secondary decays with the convolution of the same resolution model and a double exponential function. While the double exponential function is a good approximation of the true distribution of the secondary decays (see Appendix B), the chosen model for the resolution may be too simplistic, and in particular the so-called "*free*" model may be too unstable to extract accurately the behaviour of the resolution as a function of the decay time. That is why, in Chap. 6, several resolutions models, with different decay time dependencies, are used to determine the relative fraction f_{sec} of secondary decays and, consequently, the asymmetries of the primary and secondary components. The shifts of the measured value of $A_{\Gamma}^{K\pi}$ obtained by varying the resolution models (see Table 6.2) are a good estimate of the size of the systematic uncertainty on the final measurement because of a non perfect knowledge of the model and of its behaviour as a function of the decay time. Since the relative fraction f_{sec} changes significantly depending on the model that is used, as can bee seen in Fig. 6.6, the uncertainty on the resolution model can be considered as the dominant systematic uncertainty of the procedure. In fact, all other possible uncertainties affecting the subtraction procedure can be safely assumed to be negligible with respect to it. They include:

- the statistical uncertainty of the determination of the templates of the primary and secondary TIP distributions and of the relative fraction f_{sec} from the high-statistics Cabibbo-favoured $D^0 \to K^-\pi^+$ decay mode;
- possible deviations from the double exponential model for the true distribution of the secondary component;
- the uncertainty due to possible differences between the signal modes $D^0 \to K^+K^-$ and $D^0 \to \pi^+\pi^-$ and the control mode $D^0 \to K^-\pi^+$, since all models extracted from the $D^0 \to K^-\pi^+$ decays are rigidly applied to the $D^0 \to K^+K^-$ and $D^0 \to \pi^+\pi^-$ to subtract the secondary component.

Therefore, the systematic uncertainty associated to the procedure of subtracting the secondary decays is equal to the value of $0.2 \cdot 10^{-4}$, corresponding to the maximum variation of A_Γ measured with the central "*free*" model and the other resolution models described in Chap 6.

Peaking backgrounds The second largest source of systematic uncertainty of the Run 1 measurement is given by the backgrounds from partially reconstructed or misidentified decays of D mesons. This background is due to multi-body decays, such as $D^0 \to K^-\pi^+\pi^0$, $D^+ \to K^-\pi^+\pi^+$ and $D_s^+ \to K^+K^-\pi^+$, where one of the particles produced in the decay is not detected, but another one is wrongly assigned a kaon instead of a pion identity, possibly compensating the loss of invariant mass. Therefore, the $m(h^+h^-)$ distribution of this background has small, nearly linear tail that falls in the D^0 mass signal range for the $D^0 \to K^+K^-$ decays [18, 29, 51]. On the contrary, it is completely negligible for the $D^0 \to \pi^+\pi^-$ decays, as in this case the loss of invariant mass cannot be compensated by the wrong identification of another particle.

In particular, the most relevant of these multi-body backgrounds is that from $D^0 \to K^-\pi^+\pi^0$ decays, since in this case the part of the D^0 mesons that is produced in the decay of a D^{*+} has a distribution with a peak in Δm, even if with a larger standard deviation than the real $D^0 \to K^+K^-$ decays. Therefore, these decays are referenced as "peaking background". The number of these background events that is selected in data sample can be estimated by analysing the data in the sidebands of the signal region of the mass of the D^0. In these regions, the fraction

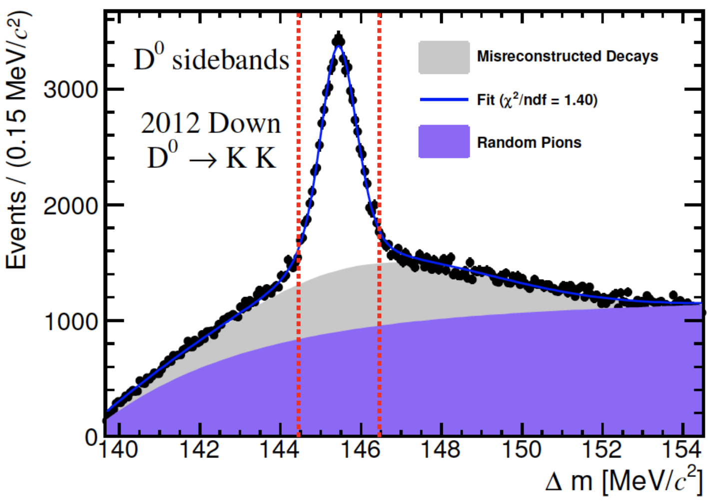

Figure 7.5: Δm distribution for events in the D^0 mass sidebands ($[m(D^0) - 6\sigma, m(D^0) - 3\sigma] \cup [m(D^0) + 3\sigma, m(\ Dz) + 6\sigma]$, where $m(D^0) = 1864.48\,\mathrm{MeV}/c^2$ and $\sigma = 8\,\mathrm{MeV}/c^2$), for the Run 1 measurement. The partially reconstructed background is drawn in grey. Figure taken from Ref. [30].

of partially reconstructed decays is larger, and can be precisely estimated by measuring their large peak in the Δm distribution (see Fig. 7.5). Extrapolating the result to the D^0 mass signal region with a linear model, a contamination of about 0.5% is obtained in the Run 1 measurement. The contamination is not expected to have change for the Run 2 data since, even if the global kinematic fit to the $D^{*+} \to D^0(\to h^+h^-)\pi^+$ decay chain with the D^{*+} constrained to originate in the PV is not performed any more, and the mass peak of signal events has therefore broadened by about a factor of 2, the peak of the partially reconstructed decays is expected to broaden by the same factor. The contribution of the aforementioned backgrounds to the measurement of A_Γ can then be assessed by measuring A_Γ^{bkg} for the background events in the Δm sidebands and multiplying it by the contamination fraction in the Δm signal region (assuming A_Γ^{bkg} to be the same in the signal and in the sideband Δm regions). A conservative systematic uncertainty of $0.5 \cdot 10^{-4}$ was estimated in the Run 1 analysis, mainly driven by the large uncertainty on A_Γ^{bkg}.

In the measurement presented in this thesis, after the reduction of the background due to secondary decays, the peaking background is expected to be the main source of systematic uncertainty. However, its value can be reduced quite easily if needed, at the expense of a loss of about 30% of the statistical precision, by tightening the cuts on the momenta of the D^0 daughter particles and on the particle identification information of the D^0. It has been verified that this procedure allows to lower this systematic uncertainty to a value $\lesssim 0.2 \cdot 10^{-4}$ [30].

The summary of all relevant systematic uncertainties, together with their total value, is reported in Table 7.2. The strategy to subtract the secondary decays that was developed in this thesis allowed a reduction of the relative systematic uncertainty by about a factor of 4 for the $D^0 \to K^+K^-$ decay mode an 6 for the $D^0 \to \pi^+\pi^-$ one, reducing the total systematic uncertainty by a factor of 1.7 and 4, respectively.

7.3 Results

The measurement of the *CP* violation A_Γ parameter with the data sample collected by the LHCb experiment during 2015 and 2016 (first half of LHC Run 2) corresponding to an integrated luminosity of $1.7\,\mathrm{fb}^{-1}$, is presented in this thesis. The flavour at production of the D^0 meson is inferred from the sign of the charged pion of the strong decay $D^{*+} \to D^0\pi^+$. The measurement is

Table 7.2: Summary of expected systematic uncertainties, in units of 10^{-4}. The systematic uncertainties of the Run 1 measurement are reported in parenthesis for comparison.

Systematic source	$\Delta A_\Gamma(D^0 \to K^+K^-)$	$\Delta A_\Gamma(D^0 \to \pi^+\pi^-)$
Correction discretisation	0.2 (0.2)	0.2 (0.2)
Combinatorial background	0.2 (0.1)	0.2 (0.1)
Peaking background	0.5 (0.5)	- (-)
Secondary decays	0.2 (0.8)	0.2 (1.2)
Total	0.6 (1.0)	0.3 (1.2)

performed for both the singly Cabibbo-suppressed decay modes $D^0 \to K^+K^-$ and $D^0 \to \pi^+\pi^-$, obtaining

$$A_\Gamma(D^0 \to K^+K^-) = (-60.9 \pm 3.8 \pm 0.6) \cdot 10^{-4},$$
$$A_\Gamma(D^0 \to \pi^+\pi^-) = (-62.5 \pm 6.7 \pm 0.5) \cdot 10^{-4},$$

where the first uncertainty is statistical, the second one systematic and the central values are blinded pending the receipt of the approval of the analysis procedure by the LHCb collaboration. Assuming that universality holds (see Sect. 1.5.5), the final averaged value for A_Γ is

$$A_\Gamma(K^+K^- + \pi^+\pi^-) = (-61.3 \pm 3.3 \pm 0.6) \cdot 10^{-4}.$$

This result improves by nearly a factor of 2 the value of the systematic uncertainty obtained in the LHCb measurement with the Run 1 data sample, $A_\Gamma = (-1.3 \pm 2.8 \pm 1.0) \cdot 10^{-4}$, that dominates the world average, paving the way to future measurements with still higher precision that are foreseen by the LHCb experiment. The statistical uncertainty is slightly lower than in the LHCb Run 1 measurement owing to the novel procedure to subtract the secondary decays from the data sample, that shifts part of the systematic uncertainty on the statistical one. However, this is expected to be beneficial in the long term, since the statistical precision on the measurement is falling rapidly. Combining the Run 1 measurement with that of this thesis, the total uncertainty on A_Γ is expected to approach the level of $2 \cdot 10^{-4}$.

7.4 Conclusions

This thesis presents the most recent and detailed studies on the measurement of A_Γ at the LHCb experiment. This analysis is the first high precision measurement to be performed at LHCb within the new data-taking Turbo paradigm [6, 7], using directly the online reconstruction of events, without further offline reprocessing. The number of collected events approximately doubled with respect to the measurement of Run 1, with a final number of about 200M of events; therefore, significant effort was put into the parallelisation of the reading and processing of this large data sample.

Detailed studies are performed to better understand the origin of the detector-induced, time-dependent asymmetries that were already observed in the Run 1 data. Moreover, the impact on the measurement of the trigger lines that are used to collect data in the Run 2 is assessed, and the main critical features that might induce undesired effects are pinpointed. For the preliminary measurement described in this thesis, only the data collected by the HLT1 single-track trigger line are used, discarding events collected with the new HLT1 two-track trigger lines, in order to allow a fast publication of the results. The two-track lines, specifically developed for Run 2 data taking, largely increased the efficiency of the trigger system in collecting pure samples of charm decays, but at the price of introducing wild and complex correlations between momenta and D^0 proper decay time, that are difficult to keep under control. Thus, the studies performed in this thesis highlighted for the first time the experimental issues and the systematic uncertainties that can derive from the implementation of a complex trigger selection, in the high precision regime of measuring CP asymmetries in the charm (and beauty) sector. Results have been presented to the LHCb Trigger Working Group, inducing an important modification of the trigger strategy for the collection of the decays of D^0 mesons into two charged hadrons for the remaining of the Run 2 data-taking periods (2017—2018).

Particular attention has been paid to the reduction of the systematic uncertainty on the secondary decays of D^{*+} mesons from the decay of b-hadrons, that dominated the systematic uncertainty of the Run 1 measurement with a value of $1.0 \cdot 10^{-4}$. In particular, a novel method is developed to precisely subtract their contribution to the measurement of A_Γ, relying on the discrimination between the distributions of the transverse impact parameter for primary and secondary decays. As a result, the relative systematic uncertainty is reduced by a factor of 5, paving the way to the measurements with still higher precision that are foreseen in the next few years by the LHCb experiment.

Appendix A

Time binning

The choice of the binning scheme for the linear fit to the time-dependent asymmetry is optimised with the following procedure. The lower cut on the decay times is set so as to avoid intervals of decay time where the trigger acceptance is very low. The final value, $0.6\tau(D^0)$, is chosen observing the decay time distribution of the `TrackMVA` HLT1 line, that is the HLT1 line with lower acceptance for low decay times, in Fig. 5.1. This value is the same as that of Run 1 measurement.

On the contrary, the chosen upper cut is considerably smaller than those used in the previous measurements of A_Γ [4, 33, 34], where it was as high as $20\tau(D^0)$. This is motivated by the fact that the fraction of background from secondary decays in the sample increases quickly as a function of decay time, as described in Chap. 6. Therefore, in order to reduce their amount in the sample and thus their bias on the measurement of A_Γ, it is desirable to choose a upper cut on the decay time as low as possible, as far as the statistical uncertainty on A_Γ is not degraded too much. Although primary decays at high decay times have a relative weight in determining the value of A_Γ that is much higher than that of decays at intermediate times, thanks to their higher lever arm, their number quickly decreases with time, compensating this effect.[1]

[1]For example, the number of decays whose decay time is higher than $12\tau(D^0)$, with respect to the total number of decays with decay time higher than $2\tau(D^0)$, that is the typical value for which the acceptance of the trigger reaches its maximum (see Fig. A.1), is suppressed at least by a factor of $e^{-10} \approx 5 \cdot 10^{-5}$ (the actual number is also lower, because the time acceptance starts decreasing already at $6\tau(D^0)$).

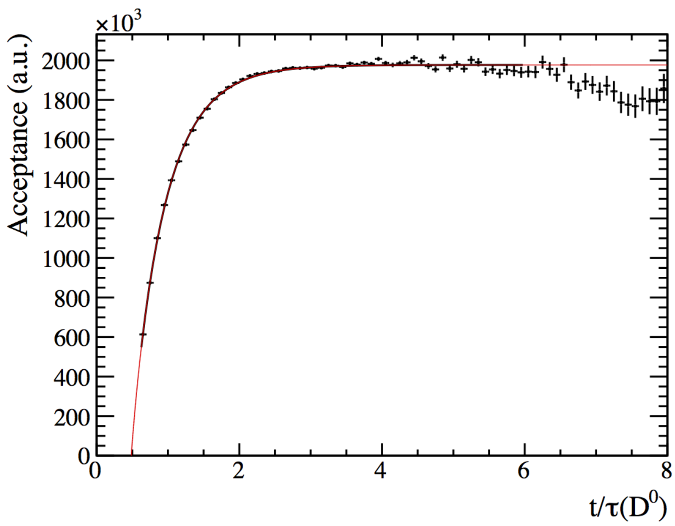

Figure A.1: Fit to the decay time acceptance of the collected data sample.

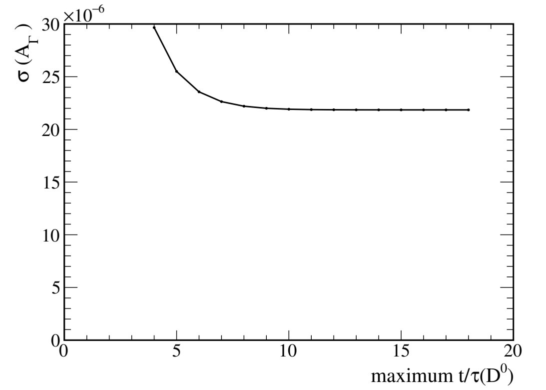

(a) Statistical uncertainty on A_Γ as a function of the upper threshold of the decay time (fit with 50 equally populated decay time bins).

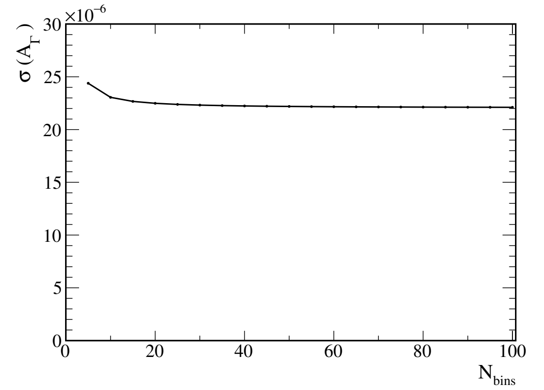

(b) Statistical uncertainty on A_Γ as a function of the number of equally populated time bins (upper threshold at $8\tau(D^0)$).

Figure A.2: Results of the simulation studies performed to decide the binning scheme for the A_Γ measurement.

Therefore, the upper cut on the decay times is chosen through simulation studies. First of all, the decay time acceptance of the trigger is determined by fitting an empirical threshold function to the decay time acceptance measured in the data sample (Fig. A.1). The choice of the function is conservative as far as the optimisation studies are concerned, as it does not take into account the loss of acceptance at high times that is observed in the data sample. Then, two decay time distributions of 10^9 events each are randomly generated according to an exponential distribution multiplied by the fitted acceptance function. At this point, the two distributions are divided into 50 equally populated bins and a linear fit to the asymmetry of the two distributions is performed; the division into time bins and the fit are repeated with progressively lower values of the upper threshold, in the range $[4, 18]\tau(D^0)$. The values of the uncertainty of the linear term (corresponding to an hypothetical A_Γ) as a function of the upper threshold are reported in Fig. A.2(a). The value $8\tau(D^0)$, corresponding to a statistical degradation of about 1.5% of the asymptotic uncertainty, is finally chosen as upper threshold.

An analogous study is performed in order to decide the number of bins, fixing the upper threshold at $8\tau(D^0)$ and dividing the distribution in different numbers of equally populated bins (Fig. A.2(b)). In this case, the number of bins of Run 1 (30) is maintained, corresponding to a statistical degradation of 1%.

Appendix B

Kinematic simulation of primary and secondary decays

In Chap. 6 the contamination of the data sample from secondary decays is subtracted by means of a fit of the TIP distributions of the primary and of the secondary decays. While the TIP of the primary decays is expected to be null within experimental sensitivity, the distribution of the TIP of the secondary decays is not known *a priori*. In order to choose the best empirical model to describe it, a kinematic phase-space simulation of the primary and secondary decays, where the secondary decays are modelled using the $\overline{B}^0 \to D^{*+}\mu^-\overline{\nu}_\mu$ decay, is performed using the `TGenPhaseSpace` library of ROOT. The input momentum spectra for both the D^{*+} and the B^0 mesons were taken from the official PYTHIA simulations of the LHCb experiment [37]; in both cases, only the $D^0 \to K^-\pi^+$ decay mode was considered, the kinematic differences between this decay mode and the $D^0 \to K^+K^-$ and $D^0 \to \pi^+\pi^-$ decays being expected to be very small. No resolution effects are implemented. A minimal set of kinematic requirements are applied, as reported in Table B.1, in order to reproduce the main acceptance features of the detector and trigger selections. In particular, all the reconstructed tracks are requested to form an angle in the range $[25, 250]$ mrad with the z axis. Since it is not possible to reproduce the requirements on the χ^2_{IP} of the two hadrons coming from the decay of the D^0 without simulating the full pp collision, they are substituted by a cut on their IP ($\mathrm{IP}(h^\pm) > 0.07\,\mathrm{mm}$) that approximately reproduces the IP distributions that are observed in the data. An analogous observation applies

Table B.1: Selection requirements for the kinematic simulation.

Candidate	Quantity	Requirement	Unit
$h^\pm$	$p_{\mathrm{T}}(h^\pm)$	> 800	MeV/c
	$p(h^\pm)$	> 5	GeV/c
	$\mathrm{IP}(h^\pm)$	> 0.07	mm
	$\arcsin(p_{\mathrm{T}}/p)(h^\pm)$	$\in [25, 250]$	mrad
D^0	$p_{\mathrm{T}}(D^0)$	> 2	GeV/c
	$\sqrt{[x(\mathrm{DV}) - x(\mathrm{PV})]^2 + [y(\mathrm{DV}) - y(\mathrm{PV})]^2}$	> 0.25	mm
	$z(\mathrm{DV}) - z(\mathrm{PV})$	> 2.5	mm
	$\theta_{\mathrm{DIRA}}(D^0)$	< 17.3	mrad
π_{s}^+	$p_{\mathrm{T}}(\pi_{\mathrm{s}}^+)$	> 100	MeV/c
	$p(\pi_{\mathrm{s}}^+)$	> 1	GeV/c
	$\arcsin(p_{\mathrm{T}}/p)(\pi_{\mathrm{s}}^+)$	$\in [25, 250]$	mrad

also to the cut on the $\chi^2_{\text{FD}}(D^0)$. Since the kinematic simulation does not take into account the uncertainties on the momenta of the final tracks, this cut is substituted by two cuts on the flight distance projections in the plane transverse to the beam and along the beam axis. The double cut is preferred over a single cut on the total flight distance since the relative uncertainty on the transverse flight distance is much lower than that on the longitudinal one for the data, so that the cut on the $\chi^2_{\text{FD}}(D^0)$ has different impacts on the transverse plane and in the longitudinal direction. The decay time of the D^0 is calculated, both for primary and secondary decays, as $t = d \cdot (m/p)$, where d is its displacement from the PV[1] and m/p the ratio of its mass to the magnitude of its momentum. Finally, the events are selected with an efficiency described by weight functions that are calculated to remove the little discrepancies in the distributions of both the momentum of the D^0 and its transverse component, between the primary decays of the simulation and those of the real data.

10M of events are simulated for both primary and secondary decays. For the secondary decays, the events are divided into 30 bins of proper decay time, with the same edges as the ones used in the analysis. The TIP distributions are found to be approximately described, in each bin of decay time, by a double-sided exponential function. The distributions of the TIP for six bins of decay time are displayed, together with the projection of the fits performed using a double-sided exponential function, in Fig. B.1. Even if the fitted function does not describe accurately the central part of the distributions, around TIP $= 0$, these small discrepancies are expected to be attenuated by the convolution with the resolution on the TIP, of the order of 15–20 µm. The fitted values of λ, as a function of the decay time, are plotted on the left of Fig. B.2. Their functional form is in good agreement with that fitted to the real data (Fig. 6.6), even if the normalisation factor is not exactly the same. Finally, the fraction of secondary decays f_{sec} is measured for the kinematic simulation as a function of the reconstructed decay time, by dividing the decay time distribution of secondary decays by the sum of the distributions of primary and secondary decays. However, the proper normalisation between the two distributions is unknown, as it depends on the production cross sections of D^{*+} and B-hadrons. The normalisation factor is chosen in order to match the distribution of f_{sec} that measured in the TIP fit of Fig. 6.6 at high times ($t/\tau(D^0) > 4$), where the fraction of secondary decays extracted from real data is reliable. The results are displayed in the right part of Fig. B.2. It is worth noting that, contrary to what is usually assumed in most LHCb analyses, the fraction of secondary decays is not null for low times.

[1] By definition, the primary vertex of the kinematic simulation coincides with the origin of the coordinate system.

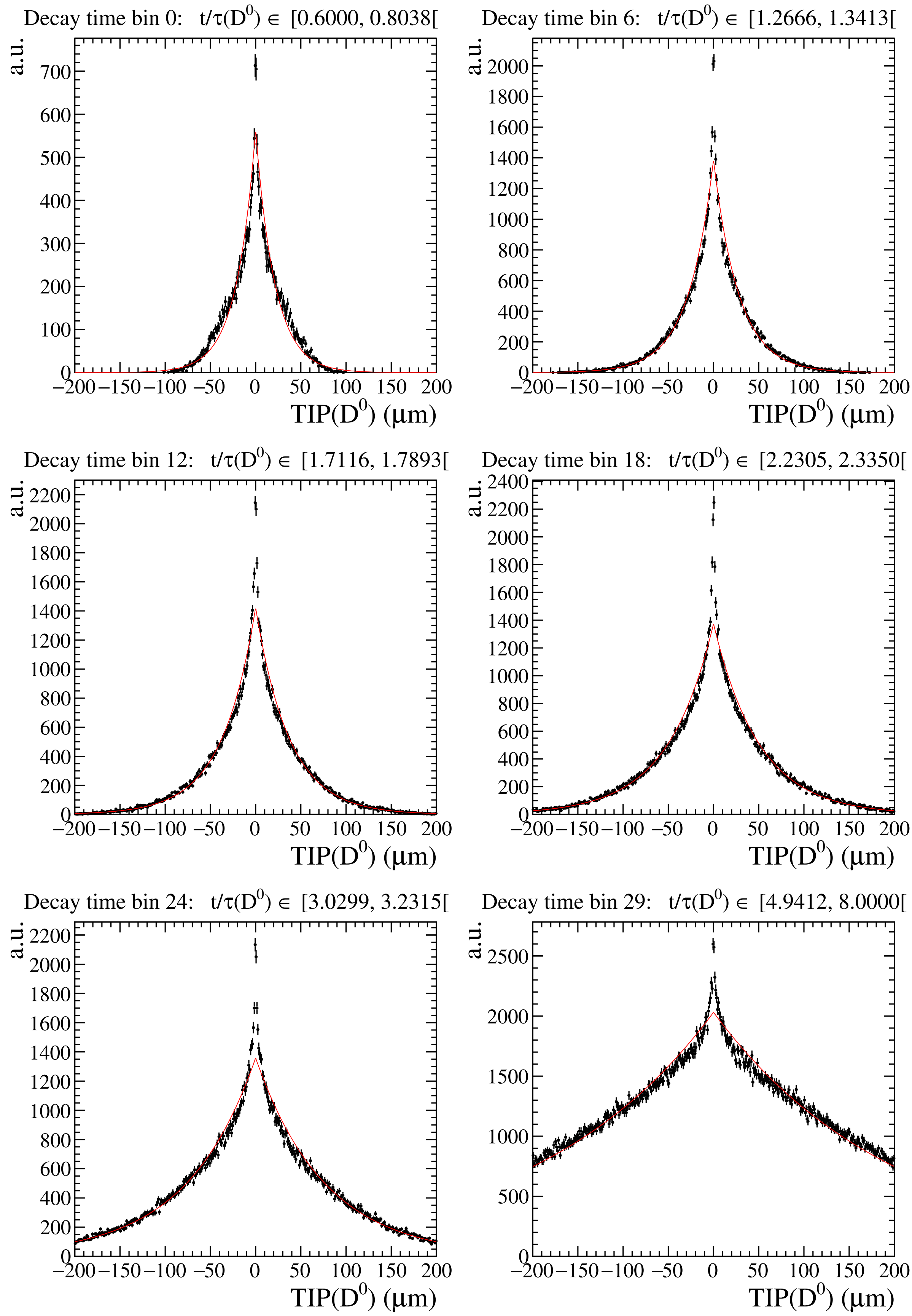

Figure B.1: Fits of a double-sided exponential function to the TIP distribution of secondary decays, for some bins of decay time.

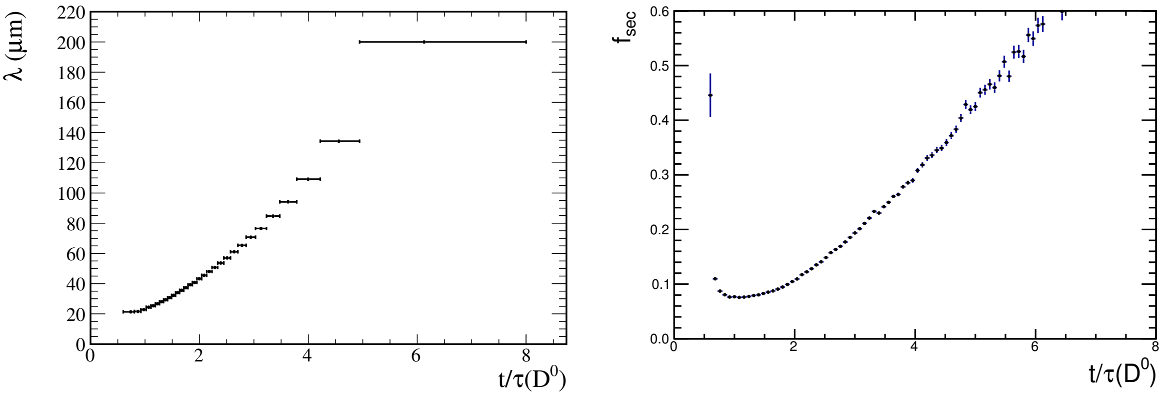

Figure B.2: Decay length λ of the double exponential function used to fit the TIP distribution of the secondary decays and fraction of secondary decays f_{sec} as a function of the D^0 decay time, as obtained from the kinematic simulation. The normalisation of f_{sec} is chosen so as to to fit the measured value of f_{sec} (Fig. 6.6) at high decay times ($t/\tau(D^0) > 4$).

Appendix C

TIP fits

This appendix reports the projections of the fits to the distributions of the TIP, performed as described in Sect. 6.4.1 and using the "*free*" model, for all bins of decay time. The data sample corresponds to the 2016 *MagUp* period; the events are weighted to correct for detector-induced, time-dependent charge asymmetries as described in Sect. 5.3. The projections are plotted both in linear and logarithmic scales, in order to evidence the small tails due to secondary decays.

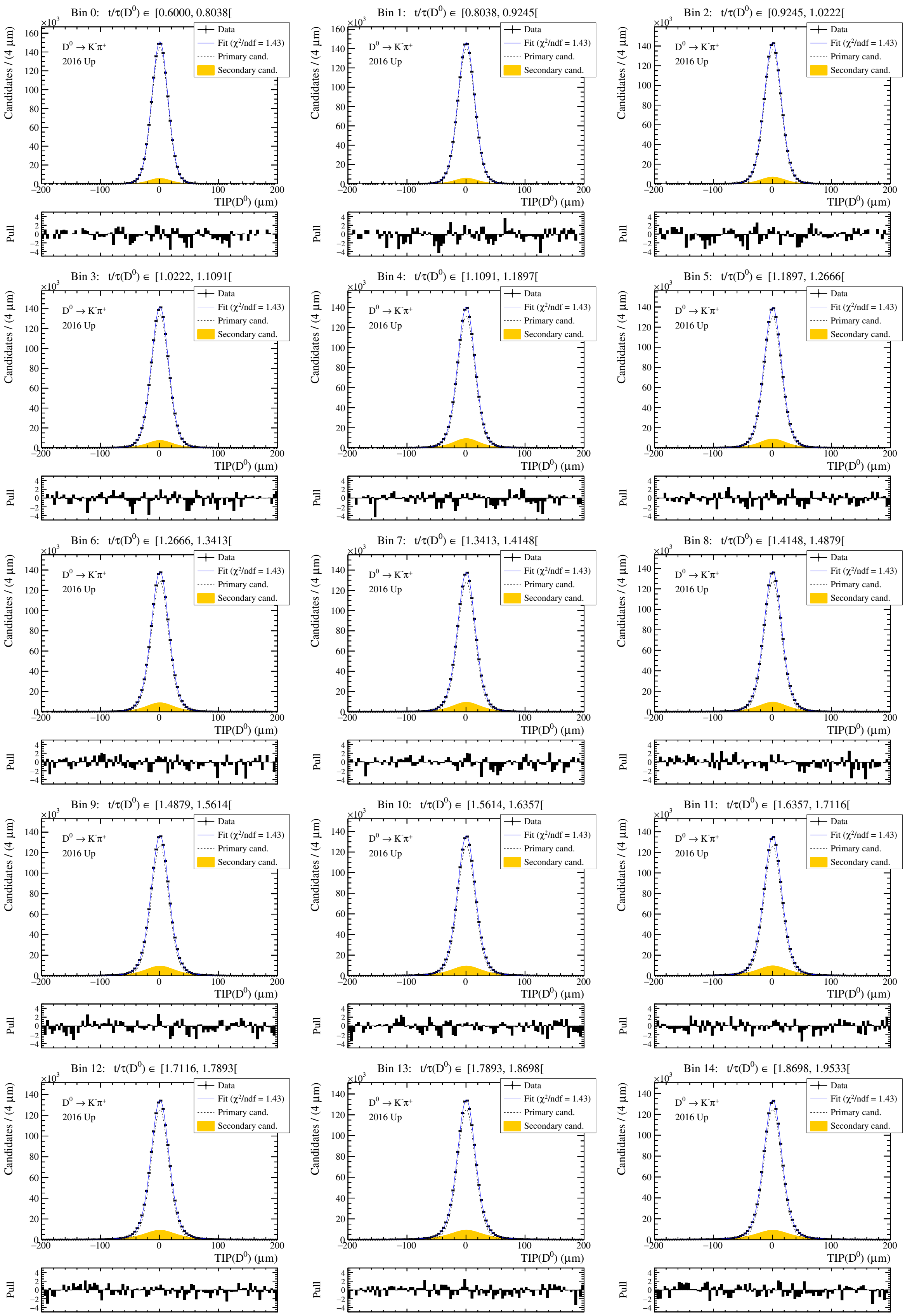

Figure C.1: Fit projections for time bins from 0 to 14 (linear scale).

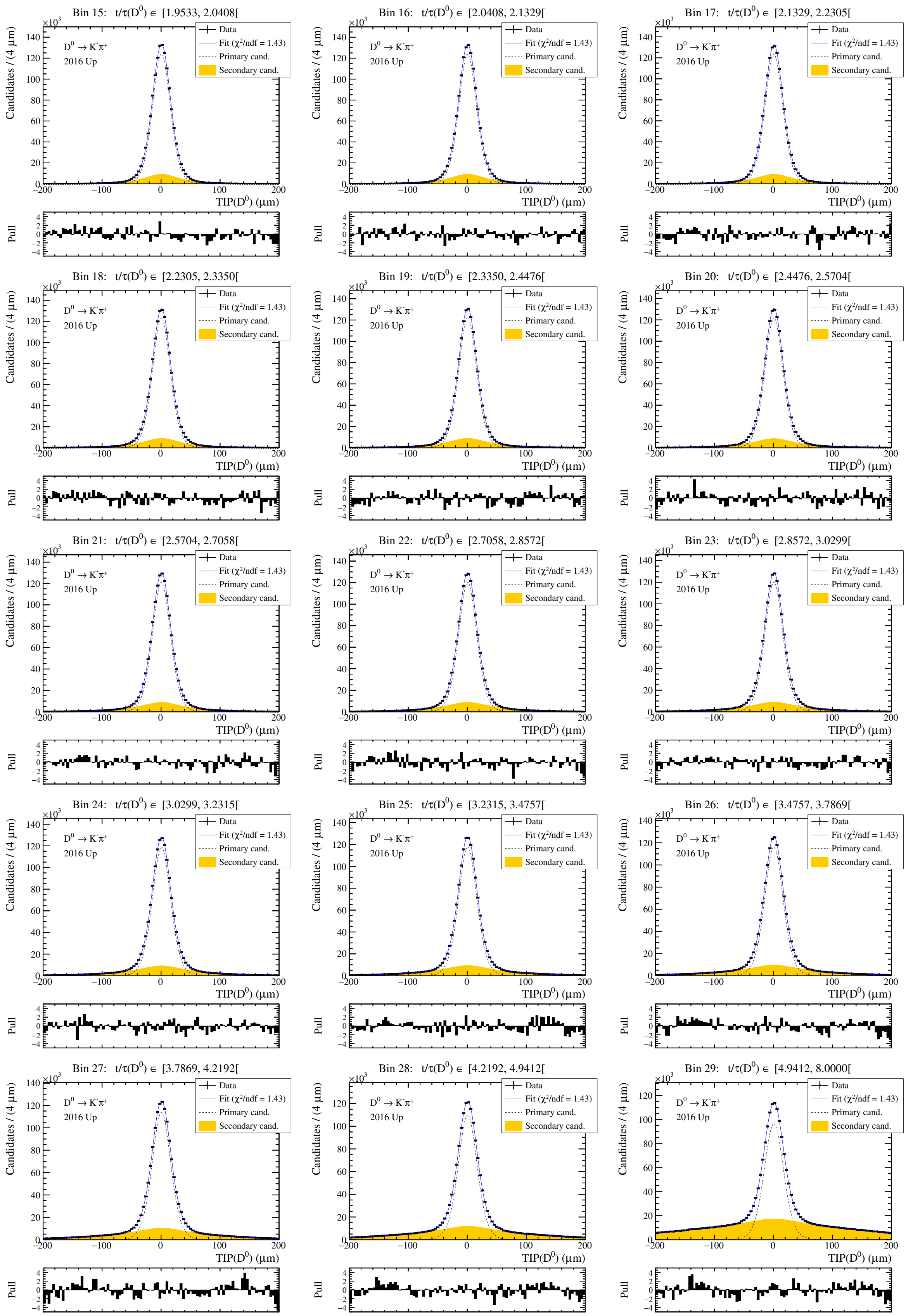

Figure C.2: Fit projections for time bins from 15 to 29 (linear scale).

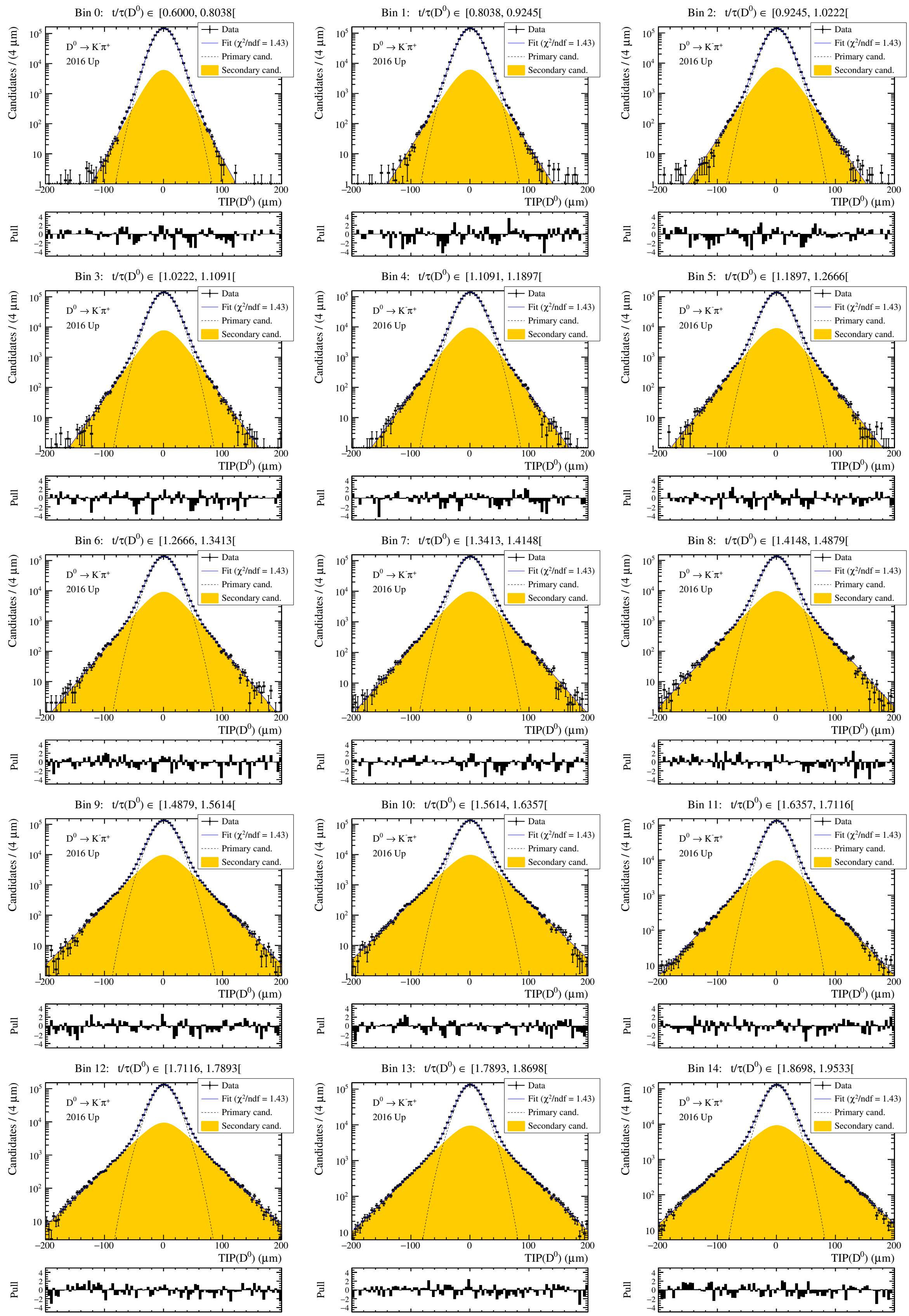

Figure C.3: Fit projections for time bins from 0 to 14 (logarithmic scale).

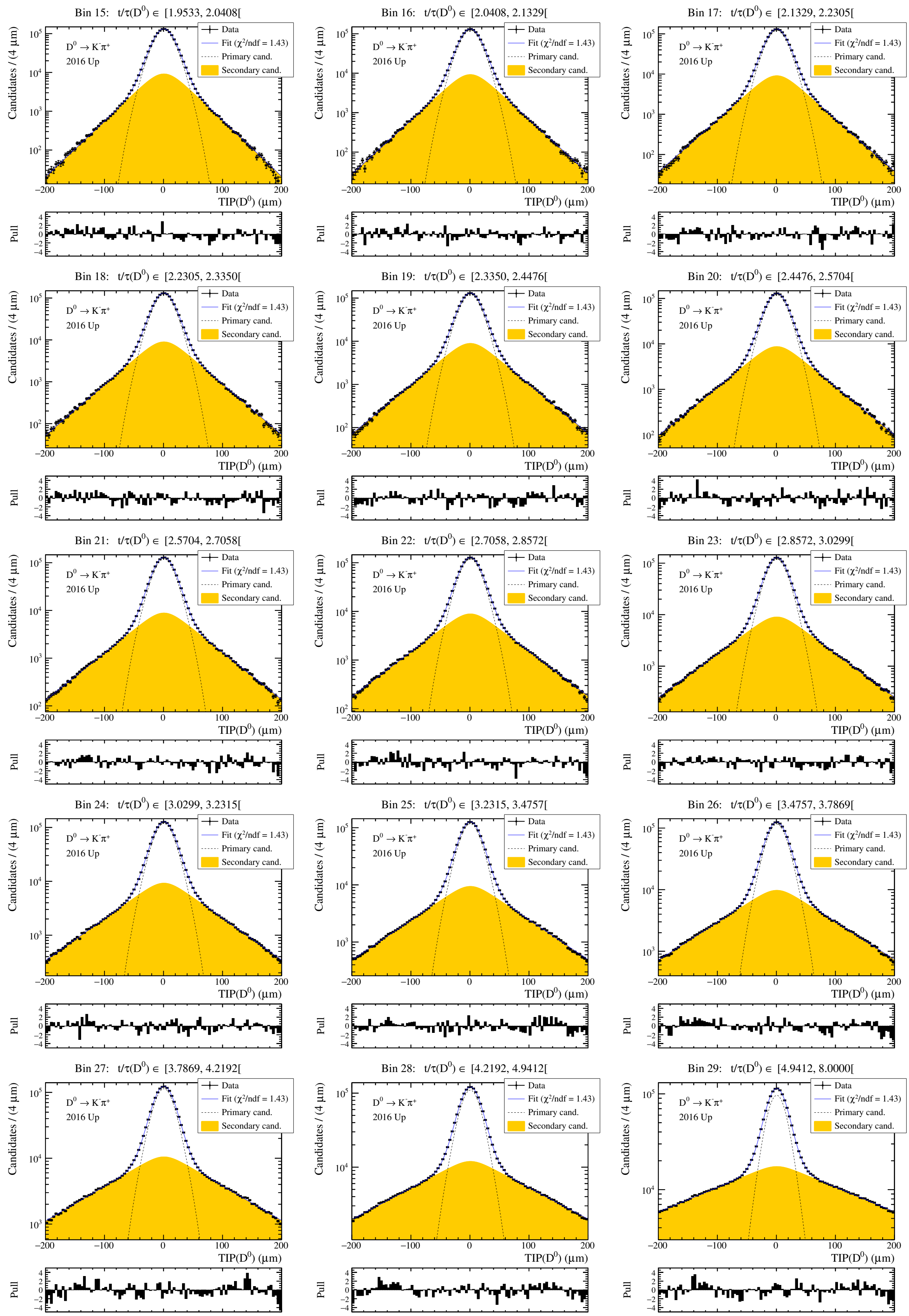

Figure C.4: Fit projections for time bins from 15 to 29 (logarithmic scale).

Bibliography

[1] Y. Grossman, A. L. Kagan, and Y. Nir, *New physics and CP violation in singly Cabibbo suppressed D decays*, Phys. Rev. **D75** (2007) 036008, `arXiv:hep-ph/0609178`.

[2] M. Bobrowski, A. Lenz, J. Riedl, and J. Rohrwild, *How large can the SM contribution to CP violation in D^0–$\bar{D}^0$ mixing be?*, JHEP **03** (2010) 009, `arXiv:1002.4794`.

[3] HFAG collaboration, Y. Amhis *et al.*, *Averages of b-hadron, c-hadron, and τ-lepton properties as of summer 2016*, `arXiv:1612.07233`.

[4] LHCb collaboration, R. Aaij *et al.*, *Measurement of the CP violation parameter A_Γ in $D^0 \to K^+K^-$ and $D^0 \to \pi^+\pi^-$ decays*, Phys. Rev. Lett. **118** (2017), no. 26 261803, `arXiv:1702.06490`.

[5] LHCb collaboration, R. Aaij *et al.*, *Measurements of prompt charm production cross-sections in pp collisions at $\sqrt{s} = 13$ TeV*, JHEP **03** (2016) 159, `arXiv:1510.01707`, [Erratum: JHEP **05** (2017) 074].

[6] S. Benson, V. V. Gligorov, M. A. Vesterinen, and J. M. Williams, *The LHCb Turbo Stream*, J. Phys. Conf. Ser. **664** (2015), no. 8 082004.

[7] R. Aaij *et al.*, *Tesla: an application for real-time data analysis in High Energy Physics*, Comput. Phys. Commun. **208** (2016) 35, `arXiv:1604.05596`.

[8] J. H. Christenson, J. W. Cronin, V. L. Fitch, and R. Turlay, *Evidence for the 2π decay of the K_2^0 meson*, Phys. Rev. Lett. **13** (1964) 138.

[9] C. A. Baker *et al.*, *An Improved experimental limit on the electric dipole moment of the neutron*, Phys. Rev. Lett. **97** (2006) 131801, `arXiv:hep-ex/0602020`.

[10] Particle Data Group, C. Patrignani *et al.*, *Review of particle physics*, Chin. Phys. **C40** (2016) 100001.

[11] V. Weisskopf and E. Wigner, *Berechnung der natürlichen linienbreite auf grund der diracschen lichttheorie*, Zeitschrift für Physik **63** (1930) 54; V. Weisskopf and E. Wigner, *Über die natürliche linienbreite in der strahlung des harmonischen oszillators*, Zeitschrift für Physik **65** (1930) 18.

[12] M. Sozzi, *Discrete Symmetries and CP Violation*, Oxford Univ. Press, 2008.

[13] A. F. Falk, Y. Grossman, Z. Ligeti, and A. A. Petrov, *SU(3) breaking and D^0–$\bar{D}^0$ mixing*, Phys. Rev. **D65** (2002) 054034, `arXiv:hep-ph/0110317`.

[14] E. Golowich and A. A. Petrov, *Short distance analysis of D^0–$\bar{D}^0$ mixing*, Phys. Lett. **B625** (2005) 53, `arXiv:hep-ph/0506185`.

[15] BaBar collaboration, B. Aubert *et al.*, *Evidence for D^0–$\bar{D}^0$ mixing*, Phys. Rev. Lett. **98** (2007) 211802, arXiv:hep-ex/0703020.

[16] Belle collaboration, M. Staric *et al.*, *Evidence for D^0–$\bar{D}^0$ mixing*, Phys. Rev. Lett. **98** (2007) 211803, arXiv:hep-ex/0703036.

[17] CDF collaboration, T. Aaltonen *et al.*, *Evidence for D^0–$\bar{D}^0$ mixing using the CDF II Detector*, Phys. Rev. Lett. **100** (2008) 121802, arXiv:0712.1567.

[18] LHCb collaboration, R. Aaij *et al.*, *Measurement of D^0–$\bar{D}^0$ mixing parameters and search for CP violation using $D^0 \to K^+\pi^-$ decays*, Phys. Rev. Lett. **111** (2013), no. 25 251801, arXiv:1309.6534.

[19] LHCb collaboration, R. Aaij *et al.*, *First observation of D^0–$\bar{D}^0$ oscillations in $D^0 \to K^+\pi^-\pi^+\pi^-$ decays and measurement of the associated coherence parameters*, Phys. Rev. Lett. **116** (2016), no. 24 241801, arXiv:1602.07224.

[20] I. I. Y. Bigi and N. G. Uraltsev, *D^0–$\bar{D}^0$ oscillations as a probe of quark hadron duality*, Nucl. Phys. **B592** (2001) 92, arXiv:hep-ph/0005089.

[21] T. Ohl, G. Ricciardi, and E. H. Simmons, *D^0–$\bar{D}^0$ mixing in heavy quark effective field theory: the sequel*, Nucl. Phys. **B403** (1993) 605, arXiv:hep-ph/9301212.

[22] H.-Y. Cheng and C.-W. Chiang, *Long-Distance Contributions to D^0–$\bar{D}^0$ Mixing Parameters*, Phys. Rev. **D81** (2010) 114020, arXiv:1005.1106.

[23] T. Gershon, J. Libby, and G. Wilkinson, *Contributions to the width difference in the neutral D system from hadronic decays*, Phys. Lett. **B750** (2015) 338, arXiv:1506.08594.

[24] A. A. Petrov, *Charm mixing in the Standard Model and beyond*, Int. J. Mod. Phys. **A21** (2006) 5686, arXiv:hep-ph/0611361.

[25] D. Du, *CP violation for neutral charmed meson decays to CP eigenstates*, Eur. Phys. J. **C50** (2007) 579, arXiv:hep-ph/0608313.

[26] D. Du, *Searching for possible large cp-violation effects in neutral-charm-meson decays*, Phys. Rev. D **34** (1986) 3428.

[27] V. V. Gligorov *et al.*, *Swimming: a data driven acceptance correction algorithm*, J. Phys. Conf. Ser. **396** (2012) 022016.

[28] LHCb collaboration, R. Aaij *et al.*, *Measurement of mixing and CP violation parameters in two-body charm decays*, JHEP **04** (2012) 129, arXiv:1112.4698.

[29] LHCb collaboration, R. Aaij *et al.*, *Measurements of indirect CP asymmetries in $D^0 \to K^-K^+$ and $D^0 \to \pi^-\pi^+$ decays*, Phys. Rev. Lett. **112** (2014), no. 4 041801, arXiv:1310.7201.

[30] P. Marino and M. J. Morello, *Measurement of the CP violation parameter A_Γ in $D^0 \to K^+K^-$ and $D^0 \to \pi^+\pi^-$ decays*, CERN-THESIS-2017-007 (2017).

[31] Belle collaboration, M. Staric, *New Belle results on D^0–$\bar{D}^0$ mixing*, in *Proceedings, 5th International Workshop on Charm Physics (Charm 2012): Honolulu, Hawaii, USA, May 14-17*, 2012. arXiv:1212.3478.

[32] BaBar collaboration, J. P. Lees *et al.*, *Measurement of D^0–$\bar{D}^0$ mixing and CP violation in two-body D^0 Decays*, Phys. Rev. **D87** (2013), no. 1 012004, arXiv:1209.3896.

[33] CDF collaboration, T. A. Aaltonen *et al.*, *Measurement of indirect CP-violating asymmetries in $D^0 \to K^+K^-$ and $D^0 \to \pi^+\pi^-$ decays at CDF*, Phys. Rev. **D90** (2014), no. 11 111103, `arXiv:1410.5435`.

[34] LHCb collaboration, R. Aaij *et al.*, *Measurement of indirect CP asymmetries in $D^0 \to K^-K^+$ and $D^0 \to \pi^-\pi^+$ decays using semileptonic B decays*, JHEP **04** (2015) 043, `arXiv:1501.06777`.

[35] LHCb collaboration, R. Aaij *et al.*, *Expression of Interest for a Phase-II LHCb Upgrade: Opportunities in flavour physics, and beyond, in the HL-LHC era*, Tech. Rep. CERN-LHCC-2017-003, CERN, Geneva, Feb. 2017.

[36] L. Evans and P. Bryant, *LHC Machine*, JINST **3** (2008) S08001.

[37] T. Sjöstrand, S. Mrenna, and P. Skands, *A brief introduction to PYTHIA 8.1*, Comput. Phys. Commun. **178** (2008) 852, `arXiv:0710.3820`; T. Sjöstrand, S. Mrenna, and P. Skands, *PYTHIA 6.4 physics and manual*, JHEP **05** (2006) 026, `arXiv:hep-ph/0603175`.

[38] LHCb collaboration, A. A. Alves Jr. *et al.*, *The LHCb detector at the LHC*, JINST **3** (2008) S08005.

[39] LHCb collaboration, R. Aaij *et al.*, *LHCb Detector Performance*, Int. J. Mod. Phys. **A30** (2015), no. 07 1530022, `arXiv:1412.6352`.

[40] L. S. T. Group, *Material for publications*, `http://lhcb.physik.uzh.ch/ST/public/material/index.php`, 2006. Accessed 13 August 2017.

[41] L. O. T. Group, *Performance of the LHCb Outer Tracker*, JINST **9** (2014), no. 01 P01002, `arXiv:1311.3893`.

[42] LHCb collaboration, I. Machikhiliyan, *Current status and performance of the LHCb electromagnetic and hadron calorimeters*, J. Phys. Conf. Ser. **293** (2011) 012052.

[43] LHCb collaboration, E. Picatoste Olloqui, *LHCb preshower(PS) and scintillating pad detector (SPD): Commissioning, calibration, and monitoring*, J. Phys. Conf. Ser. **160** (2009) 012046.

[44] W. D. Hulsbergen, *Decay chain fitting with a Kalman filter*, Nucl. Instrum. Meth. **A552** (2005) 566, `arXiv:physics/0503191`.

[45] N. L. Johnson, *Systems of frequency curves generated by methods of translation*, Biometrika **36** (1949) 149.

[46] LHCb collaboration, R. Aaij *et al.*, *Measurement of the difference of time-integrated CP asymmetries in $D^0 \to K^-K^+$ and $D^0 \to \pi^-\pi^+$ decays*, Phys. Rev. Lett. **116** (2016), no. 19 191601, `arXiv:1602.03160`.

[47] J. Albrecht, C. Fitzpatrick, V. Gligorov, and G. Raven, *The upgrade of the LHCb trigger system*, JINST **9** (2014), no. 10 C10026, `arXiv:1410.5012`.

[48] M. W. Kenzie and V. Gligorov, *Lifetime unbiased beauty and charm triggers at LHCb*, Tech. Rep. CERN-LHCb-PUB-2015-026, CERN, Geneva, Oct. 2016.

[49] CDF collaboration, T. Aaltonen *et al.*, *Measurement of CP–violating asymmetries in $D^0 \to \pi^+\pi^-$ and $D^0 \to K^+K^-$ decays at CDF*, Phys. Rev. **D85** (2012) 012009, `arXiv:1111.5023`.

[50] CDF collaboration, T. A. Aaltonen *et al.*, *Observation of D^0–$\bar{D}^0$ Mixing Using the CDF II Detector*, Phys. Rev. Lett. **111** (2013), no. 23 231802, `arXiv:1309.4078`.

[51] LHCb collaboration, R. Aaij *et al.*, *Evidence for CP violation in time-integrated $D^0 \to h^- h^+$ decay rates*, Phys. Rev. Lett. **108** (2012) 111602, `arXiv:1112.0938`.

Acknowledgements

I am grateful to my advisor, Michael J. Morello, for his close and careful supervision during the whole thesis work, often not limited by weekends and nightfalls. I also wish to thank Pietro Marino and Simone Stracka for their advice to solve the relevant computing challenges that I had to face during this year, particularly regarding the jobs submission on the grid. A special thanks to Simone Stracka for helpful explanations about the trigger of the LHCb experiment. Finally, I thank professor Giovanni Punzi for the valuable comments and suggestions he has given me from the beginning to the end of this thesis work.